NDOT Research Report

Report No. 224-14-803

Task Order 13

Thermal Gradients in Southwestern United States and the Effect on Bridge Bearing Loads

May 2017

Nevada Department of Transportation

1263 South Stewart Street

Carson City, NV 89712

Disclaimer

This work was sponsored by the Nevada Department of Transportation. The contents of this report reflect the views of the authors, who are responsible for the facts and the accuracy of the data presented herein. The contents do not necessarily reflect the official views or policies of the State of Nevada at the time of publication. This report does not constitute a standard, specification, or regulation.

Final Report
May 2017

Thermal Gradients in Southwestern United States and the Effect on Bridge Bearing Loads

SOLARIS Consortium, Tier 1 University Transportation Center
Center for Advanced Transportation Education and Research
Department of Civil and Environmental Engineering
University of Nevada, Reno
Reno, NV 89557

Leanne White
Keri L. Ryan, PhD
Ian G. Buckle, PhD
Department of Civil and Environmental Engineering
University of Nevada, Reno
Reno, NV 89557

***DISCLAIMER*:**

The contents of this report reflect the views of the authors, who are responsible for the facts and accuracy of the information presented herein. This document is disseminated under the sponsorship of the U.S. Department of Transportation's University Transportation Centers Program, in the interest of information exchange. The U.S. Government assumes no liability for the contents or use thereof.

ABSTRACT

Thermal gradients became a component of bridge design after soffit cracking in prestressed concrete bridges was attributed to nonlinear temperature distribution through the depth of the bridge. While the effect of thermal gradient on stress distributions has been previously investigated in concrete bridges, less research has been done investigating the effect on bearing loads. The climate condition of the southwestern portion of the United States may cause larger thermal gradients than recommended by AASHTO LRFD Bridge Design Specifications.

The main objective of this study was to evaluate the effect of thermal gradients in the southwestern region of the United States on bearing design. This study consisted of two parts, heat flow analysis using long-term meteorological data and two case study bridges in Nevada analyzed for bearing loadings including several variations of thermal gradient loading. One bridge was a two-span concrete posttensioned box girder bridge in Las Vegas, the second bridge was a two-span composite steel girder bridge in Reno.

Heat flow analysis was conducted using meteorological data from weather stations in Northern and Southern Nevada to evaluate the AASHTO LRFD thermal gradient recommended for Nevada. Results showed that AASHTO LRFD Zone 1 thermal gradient is an unconservative estimate of conditions in the southwestern states for both concrete and composite superstructures. Analysis in CSiBridge using area models of the concrete bridge in Las Vegas indicated that the largest predicted thermal gradient obtained through heat flow analysis increased total exterior bearing loads 12% relative to total load including the AASHTO thermal gradient. Analysis using area models of the composite steel girder bridge in Reno indicated that the unaltered temperature profile obtained through heat flow increased the total exterior bearing 27% relative to total load including the AASHTO thermal gradient at Abutment 1. Variation of constant temperature through the steel girder influenced both longitudinal and transverse loading. Reducing the temperature through the girder maximized bending moment and support reactions, while unaltered temperature through the girder maximized individual bearing loads. Thus, it is uncertain whether constant temperature through girder should be included.

ACKNOWLEDGEMENTS

This research was funded by the SOLARIS Consortium Tier 1 University Transportation Center (UTC) Grant No. DTRT13-G-UTC55 and matching funds by Nevada Department of Transportation (NDOT) under Grant No. P224-14-803/TO #13. The authors gratefully acknowledge this financial support. Furthermore, the authors extend special thanks to the bridge engineers of NDOT for allowing access to the as-built drawings and maintenance records of their bridges and eternal gratitude to Tiffany Carr for her engagement with this project.

Data were obtained from the Western Regional Climate Center (WRCC) UNR Weather Station and the National Oceanic and Atmospheric Administration (NOAA) Office of Global Programs Desert Rock Airport Surface Radiation Budget Network (SURFRAD) Station.

CONTENTS

LIST OF TABLES

LIST OF FIGURES

1. INTRODUCTION

Two types of temperature effects are considered in bridge design; uniform temperature change and nonlinear thermal gradients. A uniform temperature change causes longitudinal expansion while a nonlinear thermal gradient cause longitudinal expansion and vertical curvature.

Nonlinear thermal gradients became a consideration in bridge design when concrete bridge superstructures began to experience cracking in the bottom slab of the box girder (the soffit). The cracks were observed to expand and contract over the course of the diurnal (daily) heating cycle. The damage to the soffits of modern bridges demonstrated the need to understand and design for nonuniform temperature.

Seasonal temperature variations over the course of the year uniformly increase or decrease the temperature of the bridge, causing a proportional increase or decrease in the length of the bridge. A nonlinear temperature distribution throughout the depth of the bridge superstructure is caused by the daily fluctuations in solar radiation and ambient air temperature. This nonlinear temperature distribution is classified in two categories, positive thermal gradients and negative thermal gradients.

Positive thermal gradients occur when the temperature of the deck of the bridge is higher than the temperature of the girders. The positive gradient is a result of the rapid heating of the deck due to short wave solar radiation absorbed into the top surface along with the slow spread of heat through the depth of the bridge. Positive thermal gradients are typically observed during summer afternoons. The yearly maximum positive thermal gradient occurs on days with high solar radiation and low ambient temperatures during the summer.

Negative thermal gradients occur when the deck surface temperature is lower than the web temperature. The negative gradient typically occurs when the long wave radiation leaving the deck surface during the night rapidly cools the top of the bridge but cools through the web more slowly. Maximum negative thermal gradients occur in the early morning hours of winter. Negative thermal gradients have a significantly lower temperature difference than positive thermal gradients and do not cause tension in the soffit. Since negative gradients are not responsible for soffit cracking, design considerations are not affected by negative thermal gradients.

Thermal gradients that develop depend on the site specific environmental conditions. The solar radiation and fluctuations of air temperature experienced in the United States vary greatly throughout the year and across the nation. American Association of State Highway and Transportation Officials (AASHTO) broadly summarizes the variations across the United States by dividing the country into four zones (based on solar radiation patterns) with a thermal gradient assigned to each zone. Prior research has been conducted to investigate the appropriateness of the assigned thermal gradients in the first three zones. However, the location of the previous Zone 1 verification studies may not adequately reflect the climate of the southern portion of Zone 1. The intent of this study is to focus on the desert region of AASHTO zone 1; primarily, Arizona, New Mexico and Nevada. These

southwestern states generally experience little rainfall and high levels of solar radiation, conditions which are expected to lead to large thermal gradients.

The thermal gradient through the depth of the bridge causes internal stresses and associated forces in the supports. The resultant stresses from the thermal gradient are divided into two components; primary thermal stresses and secondary thermal stresses (Priestley and Buckle, 1978). Primary thermal stresses (which develop in a determinate structure or a structure with internal redundancies removed) are the results of nonlinear thermal gradients causing linear expansion through the depth of the beam. The final strain profile of the beam is assumed to be linear. The free strain profile is thermal strain at each point of the cross section if expansion were completely unrestrained in each fiber. The difference between the final strain and the free strain profiles cause self-equilibrating primary stresses. In an indeterminate bridge the vertical deflection is restrained creating bending moments which cause secondary thermal stresses.

The forces restraining the vertical deflection of a bridge caused by curvature also influence the bridge support reactions. The forces in the bearings that connect the superstructure to the substructure change as the bridge heats and cools in a diurnal cycle. Bearing forces in continuous multi-span concrete or composite bridges (steel girder bridges with concrete decks) have not been investigated in previous studies of thermal gradient effect. The focus of this investigation is to determine the impact thermal gradients have on the performance of bridges, especially bridge bearings through the analysis of three-dimensional thermal effects.

Modern technology allows for long term collection of meteorological data with small time intervals unlike prior research which limited meteorological data to use in heat flow. The availability of climate information allowed for heat flow analysis of northern and southern Nevada to evaluate the thermal gradient recommended by AASHTO LRFD Zone 1.

A list of bridges located in Nevada was assembled by the Nevada Department of Transportation (NDOT). The list included medium-span concrete and composite bridges with maintenance records indicating damaged bearings; two bridges were covered in this study. These bridges (one pre-stress box girder and one steel girder bridge) were modeled using CSiBridge to determine whether maximum thermal gradients increase the bearing loads beyond design capacity. This study is as an investigation of AASHTO Guide Specifications application of thermal gradients as well as a check that designers can incorporate thermal gradients into bearing design.

The terminology used hereafter is as follows: temperature profile or distribution refers to the variation of temperature through the depth of a bridge superstructure that could be measured at a given point in time. Temperature difference (ΔT) refers to the change in temperature between the deck surface and the minimum temperature in the web. Thermal gradient refers to the slope with which the temperature difference occurs. The plot of a thermal gradient adjusts the temperature profile such that the minimum temperature is equal to zero.

2. BACKGROUND LITERATURE REVIEW

2.1. Evolution of Modern Design Requirements for Thermal Gradients in Concrete Superstructure

The American Association of State Highway and Transportation Officials Load and Resistance Factor Design (AASHTO LRFD) Bridge Design Specifications service limit state load combinations included the thermal gradients effects of "axial extensions, flexural deformation and internal stresses" (AASHTO, 2010). The thermal gradients recommended by AASHTO (2010) were based on numerical equations that model how temperature throughout the depth of a bridge was affected by the surrounding environmental conditions.

Heat flow equations have been used to predict nonuniform temperature distribution in a bridge over time with applied boundary conditions representing the solar radiation, ambient temperature and wind speed. The heat flow equation predicted how heat traveled from the top of the cross section down through the depth; the solar radiation heats the surface of the deck, while ambient temperature and wind drew heat from the bottom of the superstructure. Design gradients described the most extreme temperature variation (greatest difference in temperature between deck and web or the thermal gradient that created the highest stresses in the bridge soffit) predicted by solving the heat flow equations with the solar radiation, ambient temperature and wind speed of a region recorded over the course of a year to a typical bridge cross-section.

The investigation of heat flow to predict thermal gradients in concrete superstructures originated in New Zealand and England. Two types of heat flow equations were considered, one dimensional (change through depth) and two-dimensional (change through depth and width). Since temperature change was assumed to be negligible over the length of the bridge, three-dimensional heat flow was not considered. One dimensional linear heat flow was found to be an acceptable simplification as both one dimensional and two-dimensional heat flow produce results similar to experimental data (Lanigan, 1973).

One of the more prominent heat flow equations that allowed for the modeling of thermal gradients over time came from England (Emerson, 1973). Emerson utilized an iterative method to solve the partial difference equation governing linear flow of heat. A major assumption in the application of the iterative solution was that the starting condition temperature in the bridge was uniform at 8a.m. and equal to the ambient air temperature. Emerson's linear heat flow equations were validated by comparison to the measured thermal gradient in concrete and steel bridges in England and showed a good agreement to expected shape of temperature distribution (Emerson, 1973). Emerson (1977) later reduced the absorption coefficient and amended starting conditions to achieve results closer to site temperature measurements from bridges in England and Wales.

The formulas used by Emerson were modified by Hunt and Cooke (1975) from an explicit approximation to an implicit approximation to reduce truncation error. The numerical approximations of Emerson were stable only with restrictions on the time step and node spacing. The approximation of Hunt and Cooke were unconditionally stable but increased the complexity of the computer code needed to solve equations simultaneously. Hunt and Cooke validated their solution using experimental data from a quarter scale model of a pre-

stressed concrete box girder bridge with controlled environmental conditions (Priestley, 1972b). In this experiment, heat lamps and fans were used to replicate typical diurnal fluctuations to verify theoretical thermal gradients, stress, strain and deflection values (Priestley, 1972b).

The heat flow equations of Hunt and Cooke were utilized by Priestley (1976a), to apply the typical solar radiation, wind speed and ambient temperature of New Zealand to common concrete bridge cross sections. This allowed for a parametric study that used four solar radiation sites in New Zealand and seven common concrete bridge cross sections. A plot of all critical thermal gradients (gradients causing highest tensile stress in the soffit) led to an estimated fifth order gradient as a possible design thermal gradient. Since a negative thermal gradient was not found to cause tensile force in the soffit, a design negative gradient was not suggested for New Zealand.

The Road Research Unit Bulletin of New Zealand (Priestley and Buckle, 1978) further offered a method to convert the thermal gradient into internal stresses that vary through the superstructure depth. The soffit was considered the critical section of design as case studies showed it experienced the most damage from thermal gradient. Damage to the soffit was a result of service (normal daily operation) loading rather than an extreme event (large loads of infrequent occurrence). Five bridges instrumented to record temperature were compared to the fifth order design gradient. The collected temperature profiles were similar in shape to the estimated fifth order gradient which led to the conclusion that the design gradient was conservative when predicting temperature through the cross-section depth (Priestley and Buckle, 1978). The scope of the report did not include the effect of thermal loads on bearings.

New Zealand design specifications adopted a sixth order curve for the positive thermal gradient that was proposed by Priestley (1972a) for use in concrete superstructures. This proposed gradient was based on the experimental and theoretical data of the scaled bridge model experiment. The thermal gradient tapered to zero 54 in. (1.37 m) from the maximum temperature located at the deck surface. The sixth order gradient was replaced by a fifth order gradient in 1977 (Figure 2-1) following more detailed investigation of thermal gradients (Priestley, 1976a). The fifth order gradient extended into the bridge to a depth of 47.24 in. (1.2 m) with an additional small linear positive gradient occurring in the soffit height up to 7.87 in. (0.2 m).

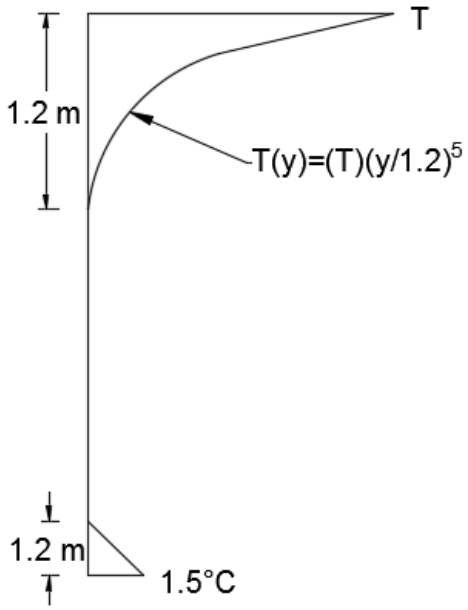

Figure 2-1-Priestley fifth-order thermal gradient

British standards (BS 5400-2, 1978) adopted straight line simplification of the thermal gradients based on Emerson (1977) for concrete, composite and steel bridges. The standard included positive and negative gradients for each type of bridge with recommendations for varying asphalt surface layer thickness. The positive thermal gradient for concrete bridges was composed of two straight-line segments that reached a maximum depth of 13.78 in. (0.350 m), and included a small positive linear gradient for the bottom 7.87 in. (0.2 m). The temperature difference of the curve depended on the depth of the bridge; it varied between the minimum difference of 15.3°F (8.5°C) for a bridge with a depth less than 7.87 in. (0.2 m) and maximum difference of 24.3°F (13.5 °C) for a depth greater than 31.50 in. (0.8 m).

The Australian bridge design code (AUSTROADS, 1992) adopted the fifth order curve proposed by Priestley (1976a). Due to the larger climatic variation across Australia, different maximum temperatures were suggested for specified regions; varying between a temperature difference of 25.2°F (14°C) on coastal sub-tropic portions of Australia and 36°F (20°C) on its inland portions. Negative thermal gradients applied were linear through a quarter of the depth recommended for the fifth order curve and the magnitude of the temperature difference was only 40% of the positive gradient.

While thermal gradients were being incorporated into bridge design codes in New Zealand, Britain, and Australia, they were applied to the United States by Potgieter and Gamble (1983) who expanded on the heat flow equation numerical methods of Hunt and Cooke (1975), Priestley and Buckle (1978) and others. Climatic data from 26 representative locations throughout America were input into the heat flow equations to determine

variation of thermal gradients across the United States. The variation in latitude and geographic regions across America led to a larger temperature difference in the thermal gradients than experienced in New Zealand or England. Potgieter and Gamble identified regions that develop similar thermal gradients; including, the desert, semi-desert, coastal regions, and the midwest. Potgieter and Gamble validated these gradients by comparing measured temperatures from bridges in Illinois to the temperature calculated using the heat flow equations.

In 1985, AASHTO sponsored a project to develop thermal gradients to be used for bridge design across the US. Imbsen et al. (1985) superimposed the 26 hypothetical thermal gradients from Potgieter and Gamble (1989) onto a map of the solar radiation contours in the United States to divide the US into four broad solar radiation zones that best fit the regions with similar gradients (Figure 2-2). The shape of the positive thermal gradient for each zone was simplified from Priestley and Buckle's fifth order curve to three straight-line segments that reached a depth of 39.36 in. (1.0 m), and a small positive linear gradient for the bottom 8 in. (0.2 m) (Figure 2-3). Maximum temperature difference of the thermal gradients varied with surfacing conditions and physical location of each zone. The largest temperature difference was applied to unsurfaced concrete in Zone 1 (Table 2-1). The presence of an asphalt surface layer reduced the temperature difference in each gradient as asphalt had been found to insulate the concrete and lower peak temperature at concrete surface. The negative thermal gradient shape was a modification of the British Standard that originated from the Emerson heat flow equations. The negative thermal gradient was half the temperature difference of the positive gradient with greater variation in temperature considered at the bottom of the bridge segment (Figure 2-4). The negative thermal gradient temperatures of unsurfaced bridges are shown in Table 2-2.

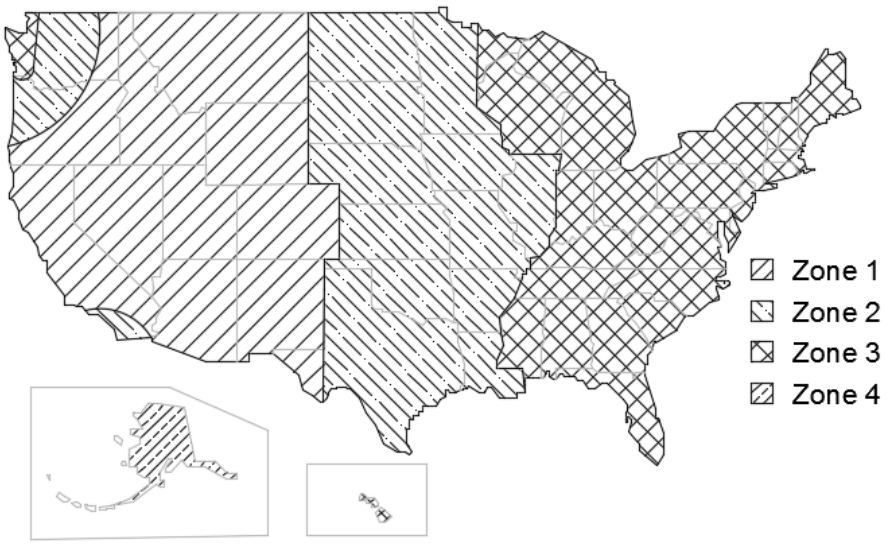

Figure 2-2- Imbsen et al. (1985) solar radiation zones for the United States

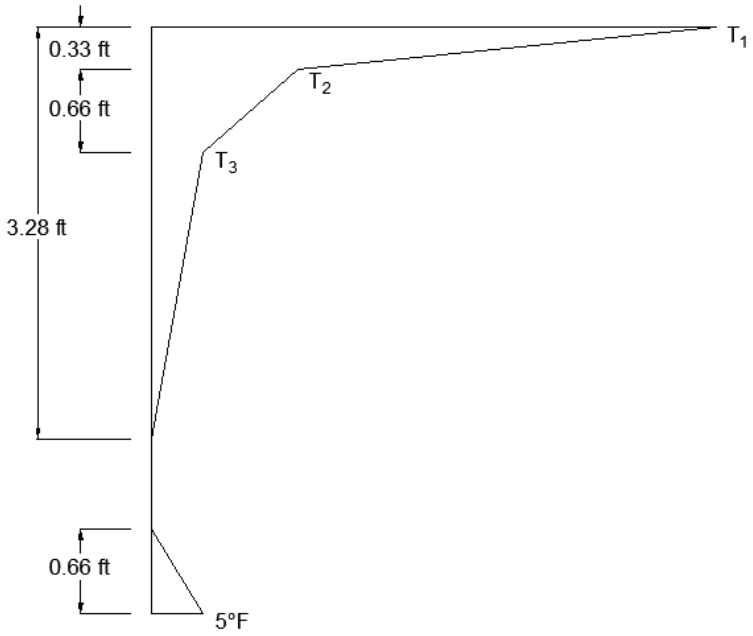

Figure 2-3-Imbsen et al. (1985) proposed positive concrete thermal gradient

Table 2-1-Imbsen et al. (1985) Positive Thermal Gradient Temperatures (Unsurfaced Condition)

Zone	T_1 [°F]	T_2 [°F]	T_3 [°F]
1	54	14	5
2	46	12	4
3	41	11	4
4	38	9	3

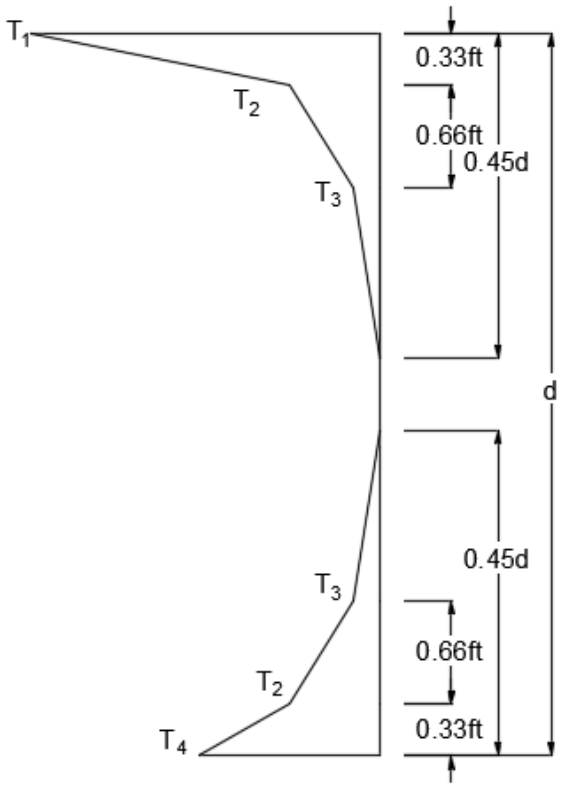

Figure 2-4-Imbsen et al. (1985) proposed negative concrete thermal gradient

Table 2-2-Imbsen et al. (1985) Negative Thermal Gradient Temperatures (Unsurfaced Condition)

Zone	T_1 [°F]	T_2 [°F]	T_3 [°F]	T_4 [°F]
1	27	7	2	14
2	23	6	2	10
3	21	6	2	8
4	19	5	2	6

In 1989, AASHTO published an abridged version of the Imbsen without recommendations for implementation of the thermal gradient. A modified version of the Imbsen thermal gradient was incorporated into the AASHTO LRFD Bridge Design Specification (AASHTO, 1994). The thermal gradient adapted into AASHTO LRFD only consider the top two temperatures of Imbsen's unsurfaced condition, as shown in Table 2-3. This version of the thermal gradient (Figure 2-5) included only two straight line segments with a significantly reduced superstructure depth of 16 in. (0.41 m) from the top of the bridge deck, and a small positive gradient for the bottom 8 in. (0.2 m). Imbsen's solar radiation zones (Imbsen et al., 1985) were adopted without alternation by AASHTO LRFD. The negative thermal gradient was shortened and reduced in magnitude to 30% of the positive gradients. The thermal gradients recommendations in AASHTO LRFD had not been updated since 1994.

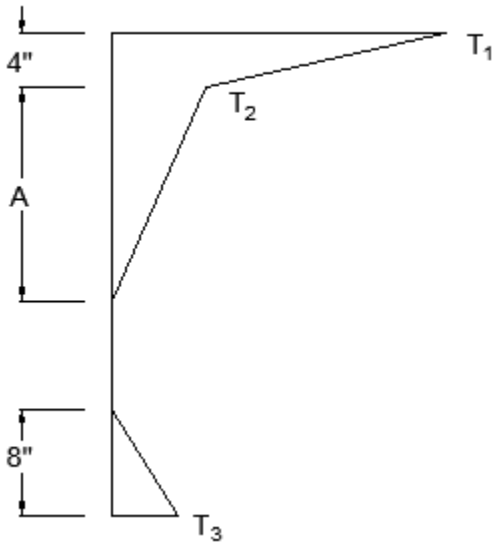

Figure 2-5-AASHTO LRFD concrete design thermal gradient

Table 2-3-AASHTO LRFD Thermal Gradient Temperatures

Zone	T_1 [°F]	T_2 [°F]
1	54	14
2	46	12
3	41	11
4	38	9

Based on the AASHTO LRFD load combinations, the thermal gradients were considered for the service level design (a load combination intended to reflect the normal daily operational levels of the bridge). AASHTO LRFD required that loads caused by thermal gradient "both longitudinally and transversely, should be calculated and considered in the design of the bearing and substructures" (AASHTO, 2010). If experience with specific bridge types had shown that structural distress was not caused by thermal gradients, the owner had the right decide to exclude thermal gradient loads. Force effects of thermal gradients were determined by calculations of axial expansion, flexural deformation and internal stresses.

The thermal gradients compared in Figure 2-6 illustrate the evolution from the original Priestley fifth order thermal gradient to the final AASHTO thermal gradient. The total depth of the bridge superstructure is assumed to be 62 in. (1.57 m) and the temperature distribution of each is based on the characteristics of the AASHTO Zone 1 (maximum temperature difference of 54°F or 30°C). Comparing the curves applicable for concrete girder shows that the AASHTO gradient depth is significantly less than the Priestley and Imbsen distributions.

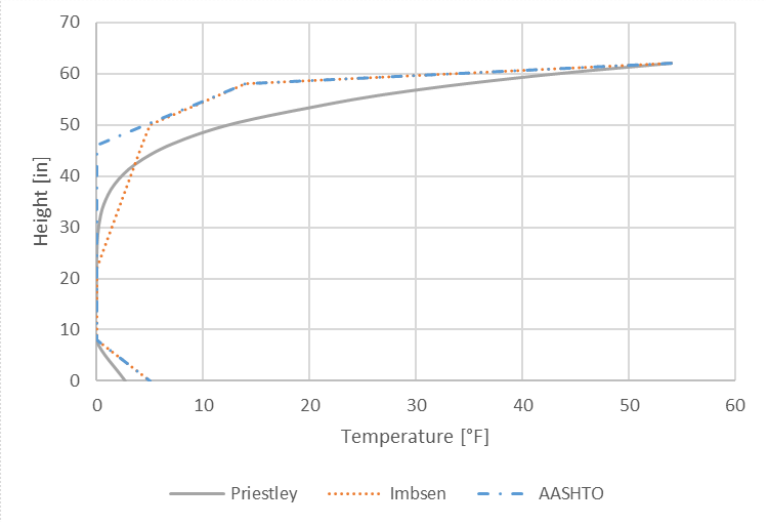

Figure 2-6-Concrete design thermal gradients

2.2. Evolution of Modern Design Requirements for Thermal Gradients in Composite Superstructure

The development of thermal gradients for composite bridges began with the theoretical work of Zuk (1961). Zuk determined the stresses that develop under four theoretical thermal gradients. The gradient for a composite bridge superstructure was composed of a linear temperature change through the depth of the concrete deck and a uniform temperature through the depth of the steel girder. The uniform temperature in the girder was assumed because the higher thermal conductivity of steel allowed it to equalize to ambient air temperature faster than the concrete slab. Later Zuk (1965) performed a field study in Virginia to measure the temperature and stresses in a composite bridge. The shape of the thermal distribution at the time of the peak gradient (between 2pm and 3pm) was a steep linear temperature change through the depth of the concrete slab and a uniform temperature or slight thermal gradient through the depth of steel girder which confirmed Zuk's previous assumptions. The temperature at the bottom of the concrete slab influenced the top of the girder before temperature equalized through the depth of the girder. Additionally, external and internal girders developed different thermal distributions. External girders were more affected by solar radiation than the internal girders, and changed temperature more rapidly than the concrete slab.

Emerson (1973) briefly considered the application of heat flow equations to a composite section using the same iterative process that was applied to a concrete bridge superstructure. The steel girders were assumed to be the same temperature as the concrete at point of interface and transition linearly to the shade temperature at a depth of 19.7 in. (0.5 m) below the interface. Emerson (1977) acknowledged that experimental observations determined the shape of the composite thermal gradient as the steel experienced transverse heat loss that could not be accurately summarized by linear heat flow analysis. The measured thermal gradient of a composite section showed a steep thermal gradient through the concrete deck and near uniform temperature through the steel girders.

Emanuel and Hulsey (1978) explored the thermal gradient of composite bridges with an adapted heat flow equation using environmental conditions for Missouri. The focus was to develop a thermal distribution for the most extreme temperature summer and winter days. For the maximum thermal gradient, the shape of the distribution was linear through the slab and approximately uniform through the girder. Non-uniformity through the top of the girder to match the bottom of the slab was sometimes observed. The gradient was found to cycle every 24-hours, and returned to a uniform temperature distribution in the early morning hours.

In 1986 Soliman and Kennedy modified the Zuk (1961) stress calculations and proposed a method of estimating stresses through the depth of the bridge. The method of estimating stresses required the shear and couple moment at interface of steel and concrete. The equations presented rely on steel and concrete material and section properties.

Kennedy and Soliman (1987) also proposed a temperature distribution for composite bridges. They compared measured temperature profiles to a wide variety of thermal gradients proposed by previous studies. Kennedy and Soliman proposed a thermal gradient

similar to Emanuel and Hulsey (1978), but with simplified straight line segments that varied linearly through the deck slab and were uniform through the girder. The temperature referenced as zero for the thermal gradient was the temperature at casting. The temperature difference of the proposed gradient was determined by season; recommended values were -7.5°F (-4.17°C) for a negative gradient in both summer and winter, +40°F (+22.22°C) and + 20°F (+11.11°C) for a positive gradient in summer and winter, respectively.

The Australian bridge design code AUSTROADS (1992) adopted a thermal distribution for composite bridges using a fifth order curve (based on Priestley, 1976a) through the depth of the concrete deck and uniform through the girder (Figure 2-7). The temperature of the interface between concrete and steel, as shown in the figure, depended on the depth of the deck: the thicker the deck, the lower the temperature in the girder.

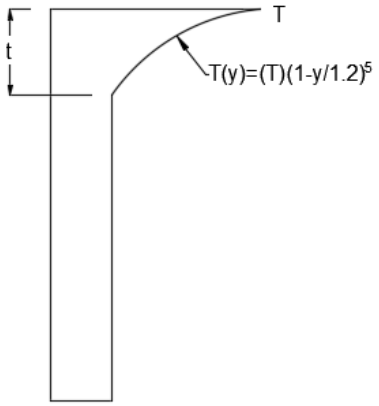

Figure 2-7-AUSTROADS steel thermal gradient

The AASHTO LRFD 1994 update also incorporated a gradient applicable to composite bridges, steel girders with concrete decks. The gradient was based on the Australian bridge design code (AUSTROADS, 1992), but used simplified straight line segments of the Priestley fifth order curve through the concrete slab (thickness t) (Figure 2-8). The AASHTO composite steel girder gradient (compared the concrete gradients in Figure 2-9) followed the AASHTO concrete gradient until interface with the steel girder where temperature became uniform through depth.

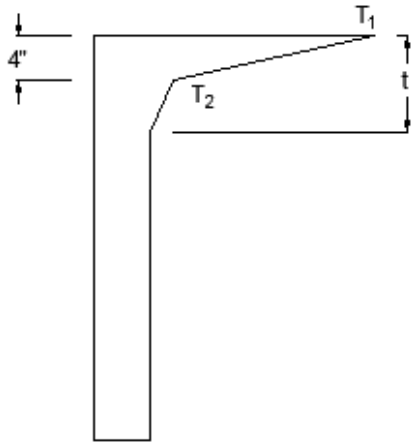

Figure 2-8-AASHTO LRFD steel design thermal gradient

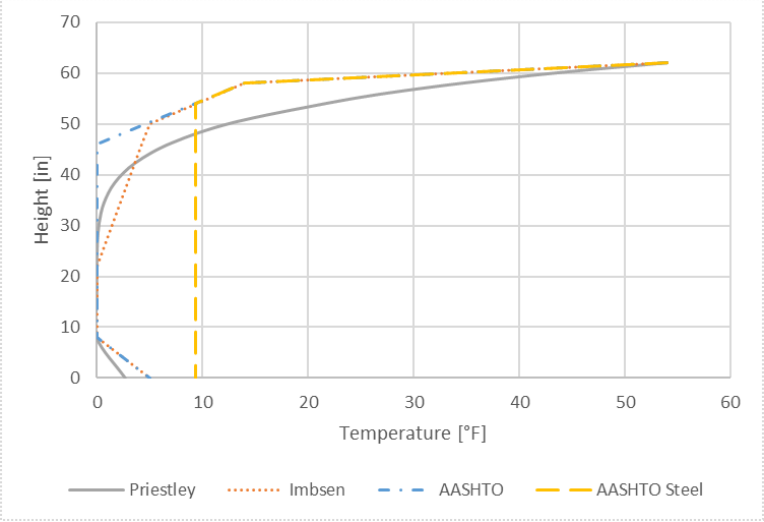

Figure 2-9-Concrete and steel design thermal gradients

2.3. Verification of AASHTO Thermal Gradient Recommendations

Recent studies reflected increased interest in monitoring bridge conditions and verifying that the code recommended thermal gradients appropriately reflect reality. The temperature in bridges were measured with thermocouples installed through the depth and width of the bridge cross section.

Roberts-Wollman et al (2002) measured the temperature of a segmental concrete box girder bridge in San Antonio, Texas (AASHTO Zone 2) over a period of 2.5 years (eight months of measurements took place before an asphalt surface was placed). For this bridge the AASHTO LRFD positive thermal gradients overestimated the maximum temperature difference measured in the bridge with and without asphalt surfacing. The shape of the

thermal gradient was determined to be similar to the gradient proposed by Imbsen et al. (1985). AASHTO negative thermal gradients also overestimated the maximum temperature difference for both unsurfaced and surfaced periods of measurement. The shape of the measure negative gradient was not well represented by the AASHTO LRFD negative gradient. Measured temperatures gradients were also compared to Potgieter and Gamble equations which estimated the maximum temperature variation in a bridge with an asphalt surface layer within 1.8°F (1°C) of the measured temperature.

Lee (2012) measured thermal gradients of a single uncovered prestressed concrete bridge girder in Atlanta, Georgia (AASHTO Zone 3) for twelve months. The recorded temperatures were compared to a 2D thermal gradient model. The paper then proposed a thermal gradient for exposed girders in the US developed from the environmental condition recorded in eight cities across the country. Although not directly compared to AASHTO, the recommended gradient extended from the top of the girder to the top of the bottom flange (57 in. (1.45 m) of depth in the field study), while AASHTO LRFD specified a maximum depth of 16 in. (0.41 m). Values of temperature T_1 at top and T_2 at bottom of the top flange were recommended for each city. Recommended temperatures were: for Phoenix, Arizona T_1 = 52ºF (28.89°C) and T_2 = 12ºF (6.67°C), for Alamosa, Colorado T_1 = 54ºF (30°C) and T_2 =13ºF (7.22°C), which were similar to the AASHTO zone 1 T_1 = 54ºF (30°C) and T_2 = 14ºF (7.78°C).

Hedegaard et al (2013) measured thermal gradients of a posttensioned concrete box girder bridge in Minneapolis, Minnesota (AASHTO Zone 2) over a period of three years. For this bridge, the AASHTO LRFD recommended gradient was not found to be conservative. The AASHTO thermal gradient underestimated the maximum measured positive and negative gradients, while the Priestley fifth order curve more closely approximated measured data.

Rodriguez (2012) measured thermal gradients of a cast-in-place, posttensioned, box-girder bridge in Elk Grove, California (AASHTO Zone 1) over a one-year period. This paper found the shape and depth of the maximum measured positive and negative gradients to be similar to the AASHTO LRFD recommendations and the temperatures recommended by AASHTO to be conservative for positive and negative gradients.

In summary, the applicability of the AASHTO LRFD thermal gradients varied by location (though there may be variation between bridge types). Limited data collected from each region of the United States precluded making general conclusions about regional difference.

2.4. Climate Consideration

The region to the east of the Sierra Mountains experiences less rainfall than coastal California or the eastern United States. This leads to lower average humidity in the south-western states; Nevada, Arizona, Utah and New Mexico (Daley et al, 2008). These states also experience low winter temperatures and high summer temperatures. Regions of highest maximum summer temperatures in the United States include southern portions of California and Nevada and eastern Arizona. While the minimum temperature of the United States does not occur in the south-western states, regions of very low temperature occur in

the northern portion of Nevada, New Mexico and Utah (Daly et al, 2008). Lack of precipitation and low humidity of the southwest states prevents the dissipation of heat through evaporative cooling.

The National Renewable Energy Laboratory (NREL) manages and updates the National Solar Radiation Database (NSRDB) to provide solar radiation data to the public. The Physical Solar Model (PSM) uses cloud properties and satellite readings to calculate surface radiation. The annual average daily total solar radiation of the United States (Figure 2-10) is highest in the southwestern states (especially Arizona, Nevada, New Mexico, and Utah). Clear skies in high altitude regions lead to warm days and rapid cooling at night, which is expected to cause significant thermal gradients in bridges. The southwest thermal loading due to daily temperature oscillation is expected to be larger than other regions of the United States.

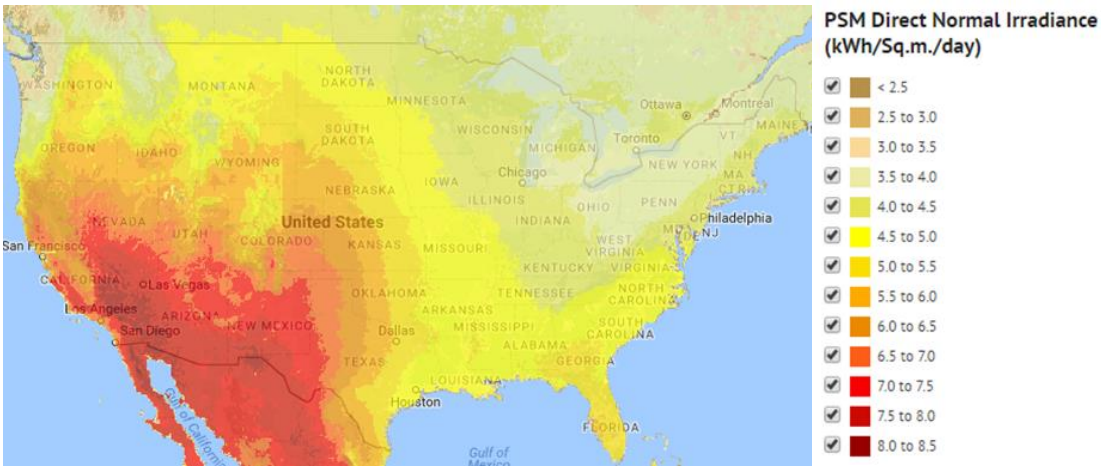

Figure 2-10-United States (PSM) average daily total solar radiation (Source: NREL, 2017)

3. HEAT FLOW PROBLEM

3.1. Introduction

To increase the understanding of bridge temperature variations the meteorological conditions of two locations in Nevada were assessed using heat flow equations and assumptions utilized by Potgieter and Gamble (1983). Previous heat flow analysis relied on limited data averaged over the course of a day or limited periods of analysis. Radiation, temperature, and wind speed recorded by two weather stations over long periods of time were used to better understand the expected daily temperature fluctuation through summer of a bridge located near the weather stations. The long period of analysis allowed for a more precise determination of the maximum temperature difference that can occur. The calculated temperatures through the depth of the bridge resolved into thermal gradients for both locations were compared to the thermal gradients from AASHTO LRFD Zone 1 and the Priestley and Buckle (1978) fifth order curve.

3.2. General Laws

The three main processes of heat exchange are: radiation, convection, and conduction. Previous studies evaluated one dimensional heat transfer through the superstructure depth and assumed that the effect of longitudinal and transverse heat flow was negligible (Lanigan, 1973; Priestley and Buckle, 1978).

Heat gain can occur through the absorption of shortwave radiation (visible light, often referred to as solar radiation) and heat loss can occur through the emission of longwave radiation (infrared light). Heat gain through shortwave radiation q_s, expressed as:

$$q_s = \alpha I_n \tag{3-1}$$

is a function of the solar radiation flux normal to the surface I_n reduced by the absorptivity (albedo) of the surface α to account for percentage lost to reflection.

Shortwave radiation typically accounts for the heating of bridge surfaces during the day, while longwave radiation is responsible for the heat loss from surfaces of the bridge at night. The heat lost through longwave radiation q_r is estimated using the Stefan-Boltzmann radiation law

$$q_r = \epsilon\sigma(R^4 - R_*^4) \tag{3-2}$$

in which ϵ is the emissivity of the surface, σ is the Stefan-Boltzmann constant and R and R_* are the absolute temperatures of the surface and sky respectively.

Absolute sky temperature is an expression of how overcast the night is. Clouds emit longwave radiation during the night into the atmosphere below, increasing the ambient temperature and preventing loss of heat from the bridge. A clear night has less longwave radiation present in the atmosphere, resulting in a colder night and increased heat emission from the bridge. If the down-dwelling infrared (longwave) radiation is measured, then it can be converted to a brightness temperature using the Stefan-Boltzmann law and used as the absolute sky temperature. A common assumption is that longwave radiation during the

day is insignificant and need only be considered when shortwave radiation goes to zero. Thus, longwave radiation is only accounted for during the night.

Convection heat transfer occurs when there is a difference between surface and ambient air temperatures. Wind speed can be a contributing factor to the rate at which heat transfer through convection occurs. Convection q_c, can be expressed as:

$$q_c = h_c(T - T_s) \tag{3-3}$$

in which h_c is an experimentally determined coefficient while T and T_s are the temperatures of the surface of the bridge and the temperature in the shade.

Conduction through the bridge determines how heat transfers through the depth of the bridge. The material properties of the bridge, heat conductivity k, mass density ρ, and specific heat c control heat flow through a body. Neglecting transverse and longitudinal heat flow (Lanigan, 1973), vertical heat flow through the depth of the superstructure is expressed as:

$$k\frac{\partial^2 T}{\partial y^2} = \rho c\frac{\partial T}{\partial t} \tag{3-4}$$

in which T is temperature, y is thickness along vertical axis, and t is time. The expression for heat conducted into a body q_y is based on Fourier's law:

$$q_y = k\frac{dT}{dy} \tag{3-5}$$

3.3. Material Thermal Properties

Some variation in assumed material thermal properties was present among the key papers that evaluated heat transfer (Emerson, 1973; Hunt and Cook, 1975; Priestley, 1976a; Potgieter and Gamble, 1983). Parameters assumed in this research conformed most closely with the values used in Potgieter and Gamble (1983), which were applicable to the United States. Material properties used for steel girders were taken to be average values. The material based properties are shown in Table 3-1.

Table 3-1-Properties of Concrete and Steel

Material Properties	Concrete	Steel
Mass density, ρ [lb/ft^3(kg/m^3)]	151 (2420)	489 (7833)
Heat conductivity, k [Btu/hr ft°F (W/m°C)]	0.8 (1.384)	31.2 (54)
Specific heat, c [Btu/lb°F (J/kg°C)]	0.22 (922)	0.11 (465)

The surface heat transfer coefficient h_c is an experimentally determined value needed for the convection contribution to heat transfer. The heat transfer coefficient of the top of the

bridge, used by both Priestley and Buckle (1978) and Potgieter and Gamble (1983), is a function of wind speed v (m/s or ft/s) and is expressed as:

$$h_{c_{top}} = 2.38 + 0.207v\ [BTU/hrft^{2}°F]$$
$$h_{c_{top}} = 13.5 + 3.88v\ [W/m^{2}°C] \quad (3\text{-}6)$$

Priestley and Buckle used the same value of h_c for top and bottom layer of the bridge; however, Potgieter and Gamble set the bottom layer of the bridge heat transfer coefficient to 45% of the top surface:

$$h_{c_{\mathrm{bottom}}} = 0.45h_{c_{top}} \quad (3\text{-}7)$$

The Potgieter and Gamble bottom layer assumption of heat transfer coefficient for concrete and composite bridge heat flows is selected for this study.

Absorptivity α depends on the color and texture of the surface layer of the bridge. Priestley (1976a) concluded that α= 0.7 for fresh clean concrete, while α= 0.9 for old concrete with a surface darkened by tire marks. To consider the effect of thermal gradients throughout the lifespan of the bridge, the absorptivity was assumed to equal 0.9. AASHTO LRFD adaptation of thermal gradients includes no provision for wearing surface; therefore, the theoretical concrete deck is assumed to be bare. The emissivity ϵ of concrete is a result of its material properties rather than color or texture. Potgieter and Gamble (1983) concluded that ϵ = 0.9 with or without wearing surface. Table 3-2 summarizes the thermal coefficients governing radiation and convection selected for this study.

Table 3-2-Thermal Coefficient Assumptions

Heat transfer coefficient (top), h_{ctop} [Btu/hr ft^2°F (W/m^2°C)]	$2.38 + 0.207v$ $(13.5 + 3.88v)$
Heat transfer coefficient (bottom), $h_{cbottom}$ [Btu/hr ft^2°F (W/m^2°C)]	$0.45 * h_{c_{top}}$
Absorpitivity, α	0.9
Emissivity, ϵ	0.9

To achieve the most accurate heat loss calculations, atmospheric emissivity is needed as the infrared radiation is being emitted and received into the atmosphere rather than the vacuum that is assumed for ideal black body radiation. Without field measurements of the absolute heat gain and loss from the bridge (referred to as an energy budget) with allowance for atmosphere emissivity, atmospheric emissivity was not included.

3.4. Solution Procedure using Finite Difference Method

The objective of solving a heat flow problem is to identify the temperature throughout the depth of a bridge when exposed to fluctuating environmental conditions (sun exposure over the course of 24-hours, changing ambient temperature, and wind speed). By using a finite difference solution of the differential equation of heat flow [Eqn. (3-5)], temperature at

each time step can be determined at discrete nodal locations by dividing the depth of the bridge into N layers of finite thickness Δ. Temperature at each node is denoted as T_i where $i = 1$ at the top surface node and increases to $i = N + 1$ at the node at the bottom node of the bridge superstructure. An example uniform material bridge section is discretized into vertical layers in Figure 3-1.

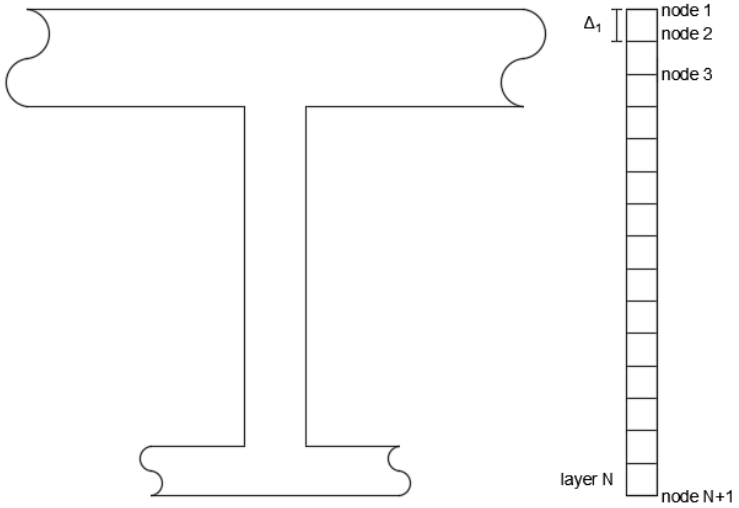

Figure 3-1-Bridge depth discretized into N layers and N+1 nodes

The surface layer of the bridge is exposed to radiation, convection and conduction. The equation for net heat transfer is written as

$$q_s - q_c - q_r - q_y = 0 \tag{3-8}$$

The net heat transfer equation is further expanded by substituting Eqs. (3-1), (3-2), (3-3) and a discretized Eq. (3-5) into Eq. (3-8), which leads to the following for the surface layer of the bridge (node 1) at time step m:

$$\alpha I_n - h_{c_{top}}(T_1^m - T_s^m) - \epsilon\sigma(R^4 - R_*^4) + k_1\left(\frac{-3T_1^m + 4T_2^m - T_3^m}{2\Delta_1}\right) = 0 \tag{3-9}$$

Conduction [Eqs. (3-4) and (3-5)] is the only method of heat transfer applicable through the interior layers. Potgieter and Gamble (1983) use the Crank-Nicholson implicit method of solving Eqn. (3-4) to provide an unconditionally stable equation to reduce restrictions on discretization of time step and layer thickness. To solve for the temperature at the time step m the known temperature at the previous time step $m - 1$ are required. Potgieter and Gamble's equation for heat transfer at node i between layers j and $j + 1$ of a uniform material ($k_j = k_{j+1} = k$) with uniform layer thickness ($\Delta_j = \Delta_{j+1} = \Delta$)is expressed

$$\frac{k}{2\Delta^2}\left(\left(T_{i-1}^{(m)} - 2T_i^{(m)} + T_{i+1}^{(m)}\right) + \left(T_{i-1}^{(m-1)} - 2T_i^{(m-1)} + T_{i+1}^{(m-1)}\right)\right) - \frac{c\rho}{\Delta t}\left(T_i^{(m)} - T_i^{(m-1)}\right) = 0 \quad (3\text{-}10)$$

A modification of the equation of heat transfer across internal layers allows for transfer across layers with different properties (different materials or layer thickness). The discretization through the top layers of the object can be increased to capture the rapid changes in temperature that can occur near the surface. An example discretization of a composite bridge is shown in Figure 3-2. The equation applicable to an interface layer (node i) with a transition in material (e.g. concrete in layer j and steel in layer $j+1$ and layer thickness Δ_j to Δ_{j+1}) is:

$$k_j \frac{(T_{i-2}^m - 4T_{i-1} + 3T_i^m)}{2\Delta_j} = k_{j+1} \frac{(-3T_i + 4T_{i+1} - T_{i+2})}{2\Delta_{j+1}} \quad (3\text{-}11)$$

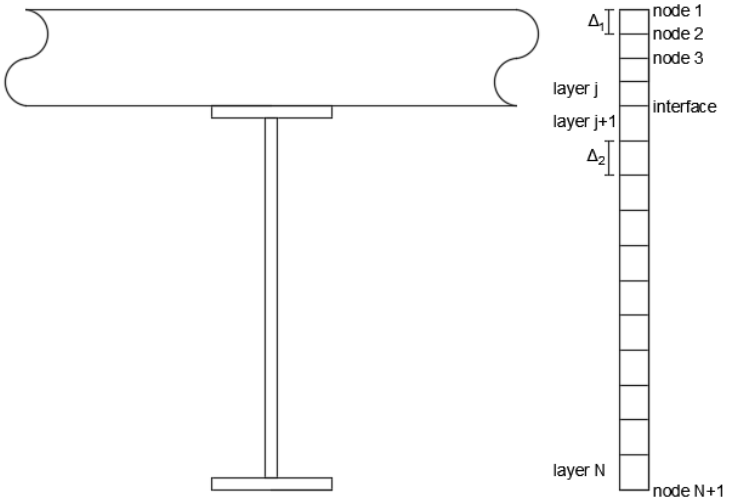

Figure 3-2-Composite bridge discretized into N layers and N+1 nodes

The bottom layer of the bridge is not exposed to direct solar radiation. Heat loss through longwave radiation is also neglected as the heat exchange between the bridge and the ground, which are both emitting longwave radiation, is considered approximately equal. Convection [Eqn. (3-3)] and conduction [Eqn. (3-5)] are the only components that remain for the net heat transfer equation [Eqn. (3-8)] for bottom node of the bridge ($N+1$)which leads to:

$$-h_{c_{bottom}}(T_{N+1} - T_s) + k_n\left(\frac{-3T_{N+1} + 4T_N - T_{N-1}}{2\Delta_N}\right) = 0 \quad (3\text{-}12)$$

where the thickness Δ and heat conductivity k are determined by the properties of bottom layer N.

Equations are solved simultaneously and expressed in matrix form for convenience. Temperature at time step m is calculated by solving the equation:

$$[A]\{T\}^{(m)} = \{B\}$$

As an example, the matrix $[A]$ of a section divided into four layers and five nodes with a change in material properties at the third layer is expressed as:

$$\begin{bmatrix} 3+h_{c_{top}} r_1 & -4 & 1 & 0 & 0 \\ p_1 & 2+2p_1 & -p_1 & 0 & 0 \\ k_1\Delta_2 & -4k_1\Delta_2 & 3k_1\Delta_2 - 3k_2\Delta_1 & -4k_2\Delta_1 & k_2\Delta_1 \\ 0 & 0 & p_2 & 2+2p_2 & -p_2 \\ 0 & 0 & 1 & -4 & 3+h_{c_{bottom}} r_2 \end{bmatrix}$$

where $r_1 = \frac{2\Delta_1}{k_1}$,$r_2 = \frac{2\Delta_2}{k_2}$, $p_1 = \frac{k_1 \Delta t}{\rho_1 c_1 \Delta_1^2}$, and $p_2 = \frac{k_2 \Delta t}{\rho_2 c_2 \Delta_2^2}$

while the right-hand side vector $\{B\}$ is expressed as:

$$\begin{Bmatrix} r_1 h_{c_{top}} T_s + q \\ p_1 T_1^{(m-1)} + (2+2p_1) T_2^{(m-1)} + p_1 T_3^{(m-1)} \\ 0 \\ p_2 T_3^{(m-1)} + (2+2p_2) T_4^{(m-1)} + p_2 T_5^{(m-1)} \\ r_2 h_{c_{bottom}} T_s \end{Bmatrix}$$

where $q = \alpha I_n - \epsilon\sigma(R^4 - R_*^4)$

3.5. Weather Stations

Environmental conditions of two different sites were obtained to evaluate the actual factors present in Northern and Southern Nevada. To solve for the heat flow in the representative bridge in northern Nevada, data from the University of Nevada Reno (UNR) Weather Station was used (Western Regional Climate Center, 2017). The UNR Weather Station is in Reno on the UNR campus (30.3918N, 119.80476W) at an elevation of 4480 ft (1365.5 m) above sea level and is managed by the Western Regional Climate Center. The data used from this site included measurements of downwelling solar and infrared radiation (W/m^2), average air temperature (°C), and wind speed (m/s) in 2015.

Southern Nevada was represented by data from the Desert Rock Airport Surface Radiation Budget Network (SURFRAD) station located 60 miles north west of Las Vegas, Nevada (36.624N, 116.019W), at an elevation of 3304 ft (1007 m) above sea level. SURFRAD is a long-term monitoring project established by the NOAA (National Oceanic and Atmospheric Administration) Office of Global Programs (NOAA Air Research Laboratories, 2017). Seven SURFRAD stations are currently in operation collecting

measurements of surface radiation budget (downwelling and upwelling solar and infrared measurements) to verify satellite based estimates of climate. Desert Rock (installed in 1998) was the most recent site to be added to the SURFRAD project. The data used from this site included measurements of downwelling solar and infrared radiation (W/m^2), 10-meter air temperature (°C), and wind speed (m/s) in 2015.

3.6. Heat Flow Analysis in Nevada

The heat flow equations were solved for the period of May through August, the months most likely to experience maximum positive thermal gradients. Data was taken from 2015, which was the most recent year with limited interruptions in collection occurring at either station. The assumed initial condition was uniform temperature through the depth of the bridge equal to the ambient temperature at 8 a.m. of the first day of the period analyzed. A theoretical bridge depth of 62 in. (1.575 m) (e.g. Figures 2-6 and 2-9) was assumed. Two bridge types were considered during the heat flow analysis, a concrete superstructure with constant material properties through the total depth and a composite bridge superstructure with a concrete deck and steel girders. For the composite bridge, an 8 in. (0.203 m) thick concrete deck was assumed to overlay 54 in. (1.372 m) steel girders. Fifteen layers were assumed for both bridge superstructures as the number of layer at which temperature in a profile converged: 15 uniform layers for the concrete superstructure section (Figure 3-3), and 4 thin deck layers with 11 thicker girder layers for the composite steel girder section (Figure 3-4). Temperature readings were available for the UNR weather station at 10 minute increments and for the Desert Rock station at 1 minute increments.

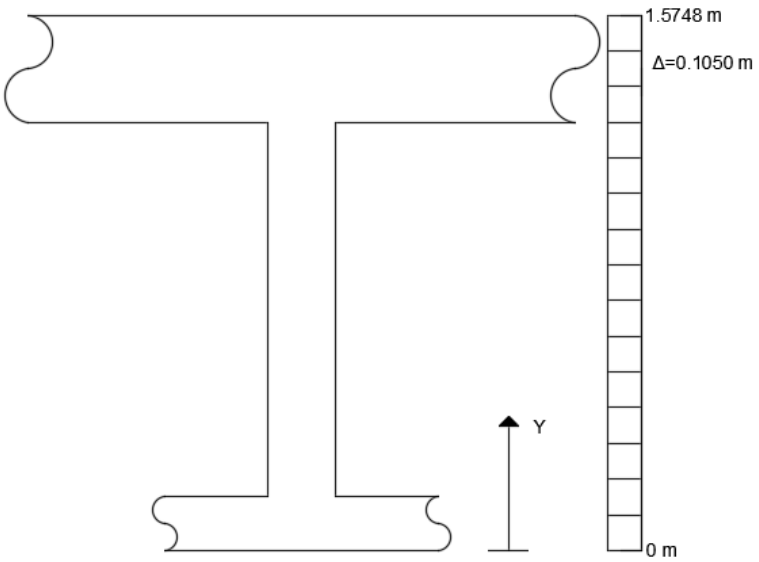

Figure 3-3-Hypothetical concrete bridge girder discretetized for heat flow

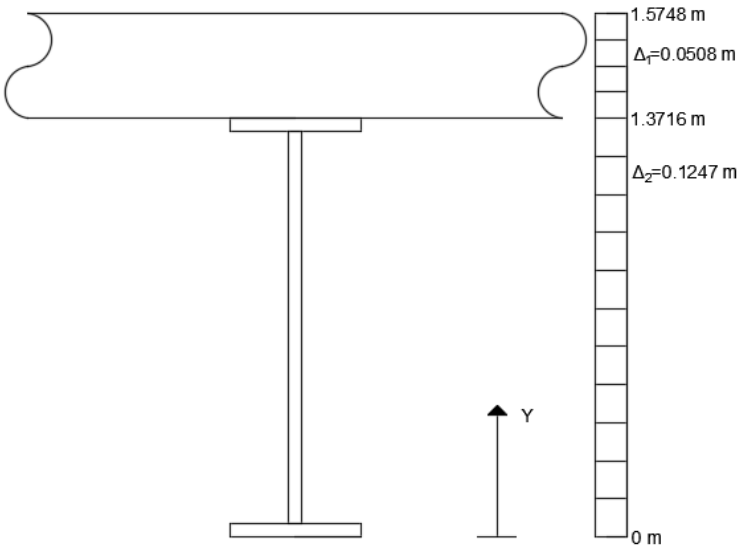

Figure 3-4-Hypothetical composite bridge girder discretetized for heat flow

The temperature through the bridge varied widely during a 24-hour period. The variation in temperature in the top, bottom and middle layer of a concrete section over a 24-hour period of a typical day are shown in Figure 3-5 and 3-6 corresponding to the UNR Weather

Station and Desert Rock SUFRAD Station, respectively. The top surface experienced the most variation in temperature through each 24-hour period, closely following the changing intensity of solar radiation, followed by the bottom layer of the section, which gains heat through convection with ambient air. The change in temperatures of internal layers was insignificant over the course of one day. The temperature profile of the section varied over the course of the day. Figure 3-7 shows four temperature profiles computed using the UNR Weather Station data on July 1st, while Figure 3-8 shows four temperature profiles computed using the corresponding Desert Rock SUFRAD Station data. The temperature profile oscillated from a negative gradient in the early mornings to a positive gradient at midday, and back to a negative gradient in the evening.

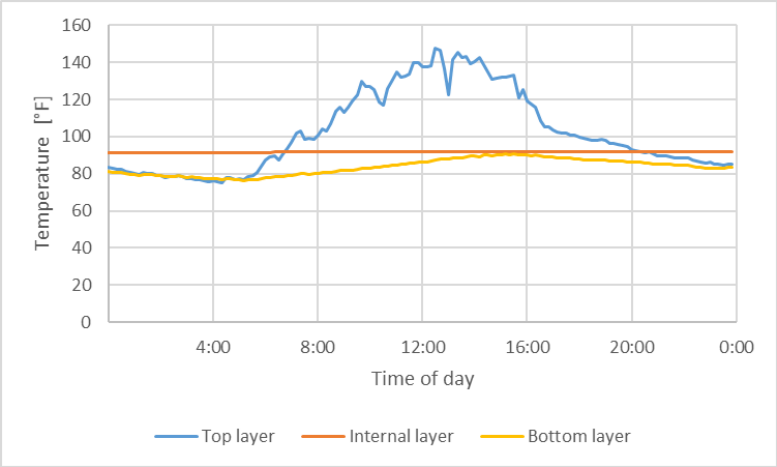

Figure 3-5-Concrete section 24-hr temperature variation July 1, 2015 from UNR Weather Station data

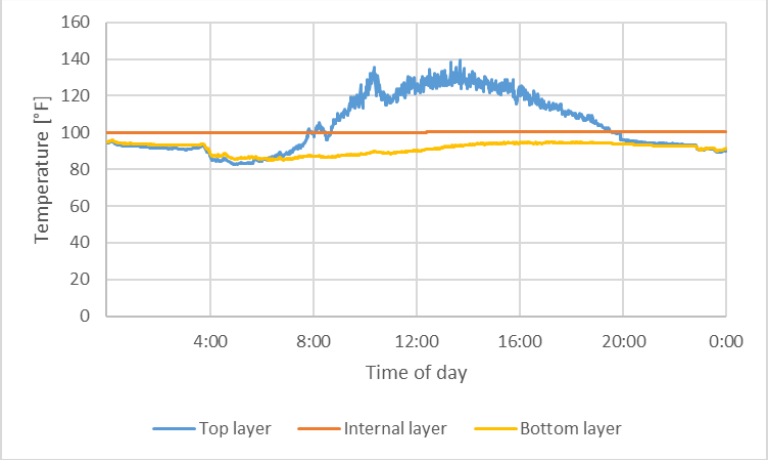

Figure 3-6-Concrete section 24-hr temperature variation July 1, 2015 from Desert Rock SUFRAD Station data

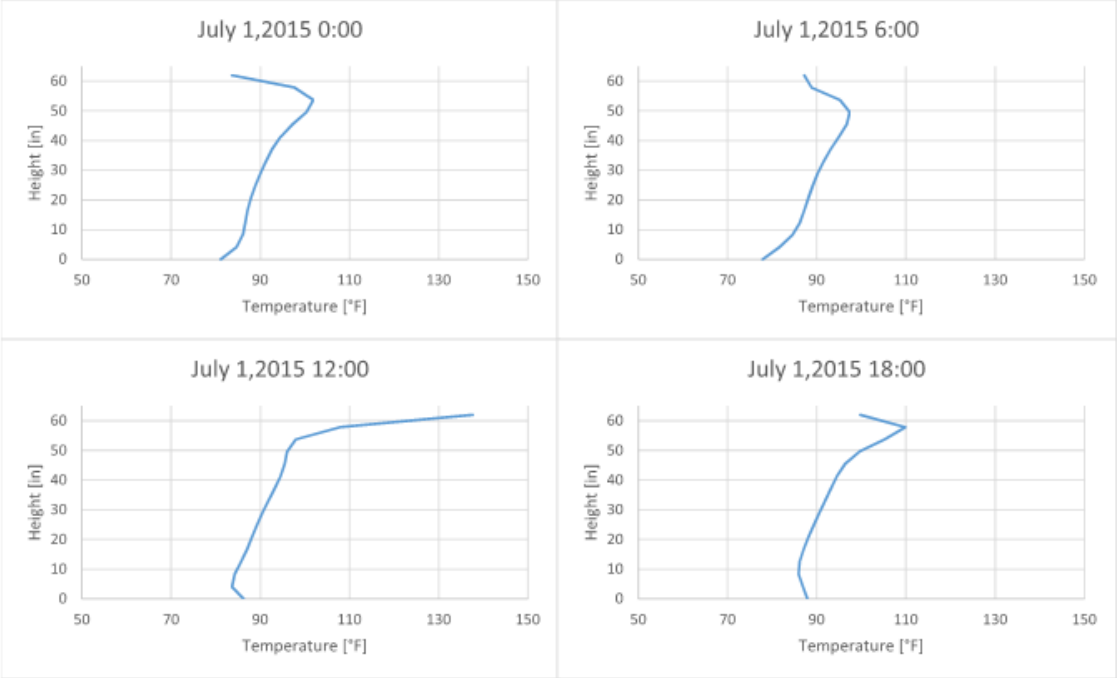

Figure 3-7-Concrete section temperature profiles from UNR Weather Station data over the course of 24-hour period at six hour intervals

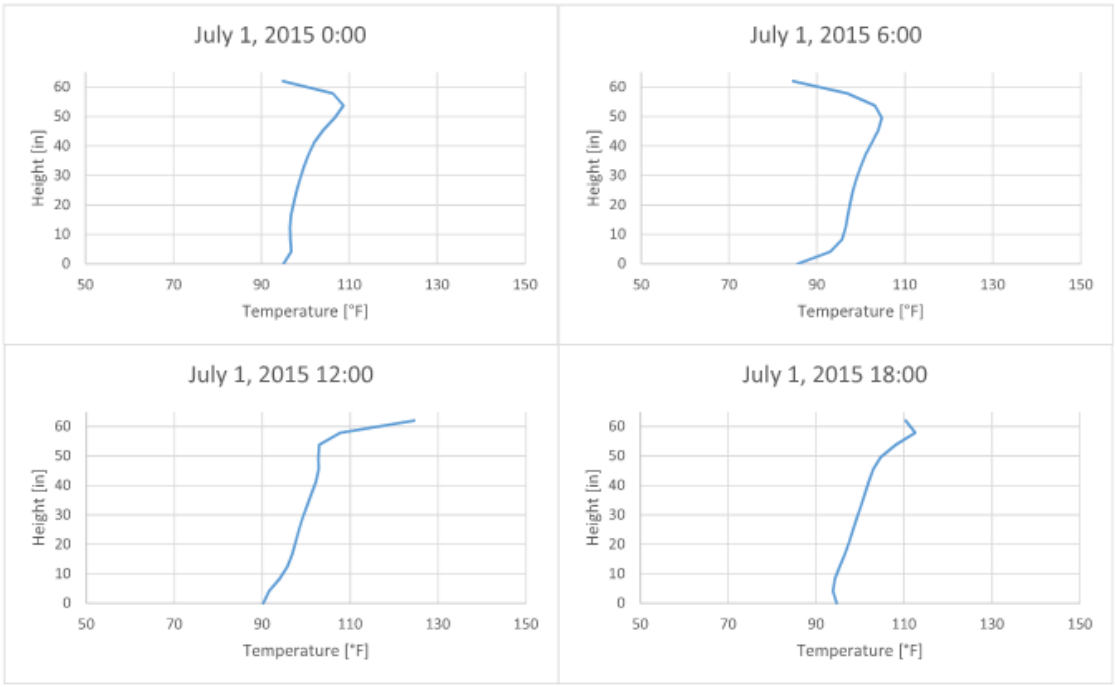

Figure 3-8-Concrete section temperature profiles from Desert Rock SUFRAD Station data over the course of 24-hour period at six hour intervals

To identify a maximum positive thermal gradient (largest temperature difference) that occurs between May and August, the difference between the temperature at the surface layer and lowest temperature of the internal layer was evaluated at each 10-minute interval for the UNR Weather Station results (Figure 3-9) and at each minute interval for the Desert Rock SUFRAD Station results (Figure 3-10). The temperature difference in the bridge superstructure exceeded 54°F (30°C) during a significant portion of the examined time frame. Temperature difference computed from the UNR Weather Station data exceeded 72°F (40°C) on six separate days (Table 3-3), while temperature difference computed from the Desert Rock SUFRAD Station data exceeded 72°F (40°C) on seven separate days (Table 3-4).

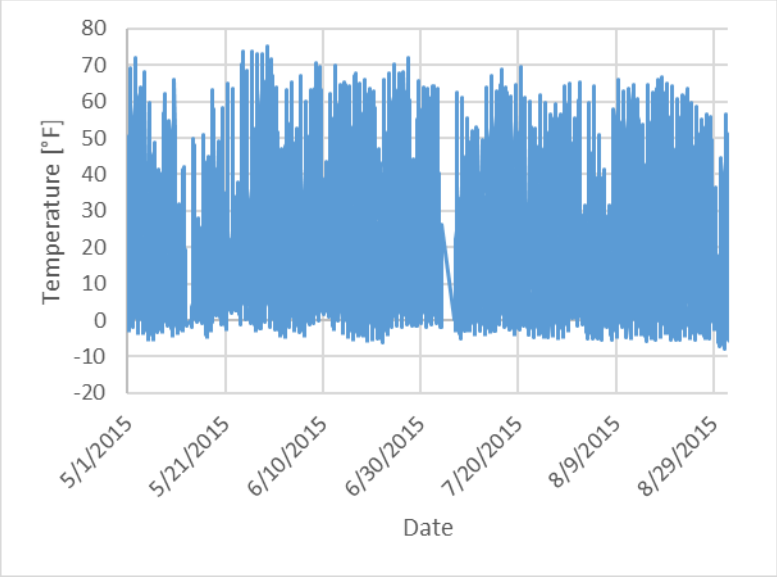

Figure 3-9-Concrete section temperature difference from UNR Weather Station data

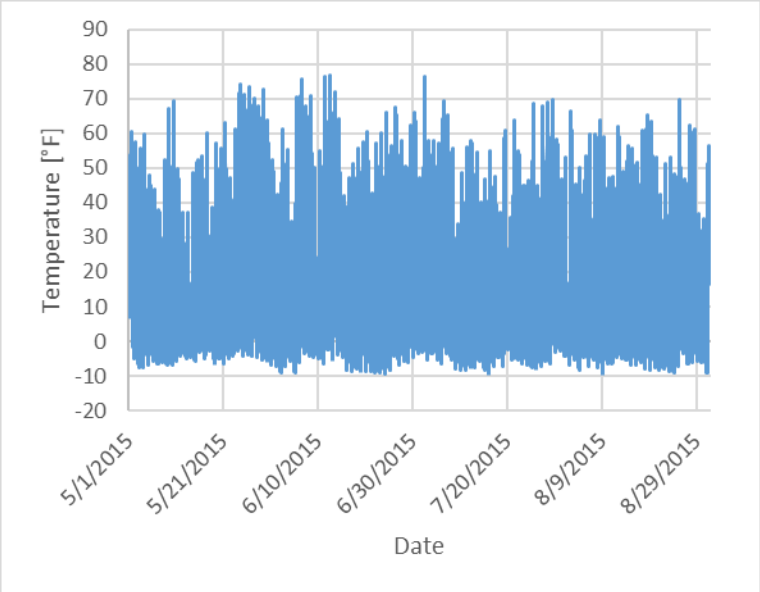

Figure 3-10-Concrete section temperature difference from Desert Rock SUFRAD Station data

Table 3-3-Instances exceeding 72°F (40°C) temperature difference from UNR Weather Station data

Date	Time	Temperature Difference [°C]	Temperature Difference [°F]
5/24/2015	13:30	40.895	73.611
5/26/2015	13:50	41.004	73.807
5/27/2015	12:20	40.619	73.114
5/28/2015	13:00	40.576	73.037
5/29/2015	12:30	41.859	75.346
6/27/2015	13:40	40.050	72.090

Table 3-4-Instances exceeding 72°F (40°C) temperature difference from Desert Rock SUFRAD Station data

Date	Time	Temperature Difference [°C]	Temperature Difference [°F]
5/24/2015	13:50	41.128	74.030
5/26/2015	13:40	40.758	73.364
5/29/2015	12:20	40.299	72.538
6/6/2015	13:02	42.032	75.658
6/11/2015	12:28	41.724	75.103
6/12/2015	14:27	42.549	76.588
7/2/2015	14:27	42.549	76.588

The profiles that were formed on the days with a temperature difference greater than 72°F (40°C) for the UNR Weather Station data are plotted in Figure 3-11 while the profiles for the Desert Rock SUFRAD Station data were plotted in Figure 3-12. The profiles calculated in Desert Rock had a larger variation in shape than the profiles at UNR. The Desert Rock profiles had higher temperature in the internal layers than the UNR profiles.

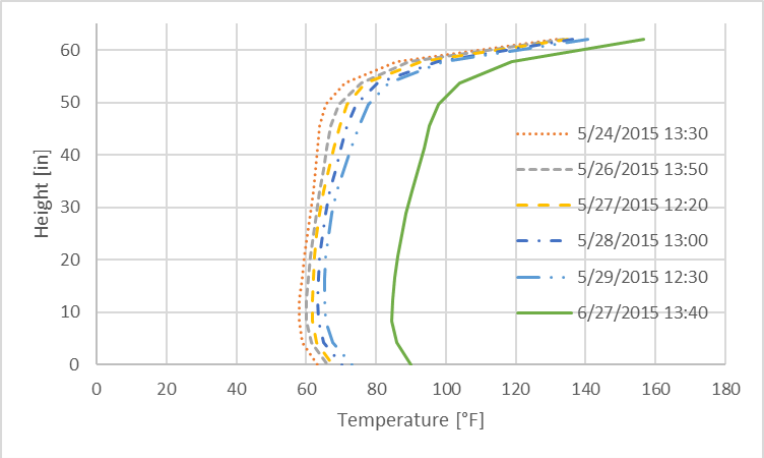

Figure 3-11-Temperature profiles with minimum 72°F (40°C) temperature difference from UNR Weather Station data

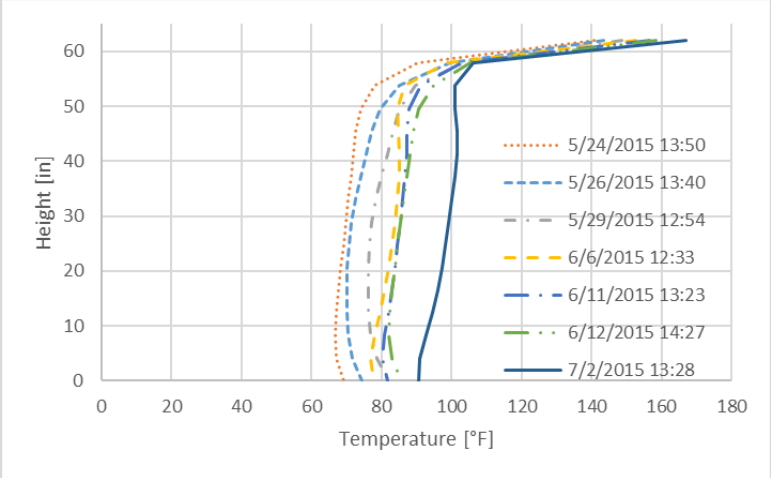

Figure 3-12-Temperature profiles with minimum 72°F (40°C) temperature difference from Desert Rock SUFRAD Station data

To examine the similarities of temperature distribution vs. depth on days with temperature difference exceeding 72°F (40°C), the temperatures were adjusted such that the minimum temperature equaled zero (UNR in Figure 3-13 and Desert Rock in Figure 3-14). The UNR profiles had similar top and bottom layers with variations occurring between the depths of 55.11 and 15.75 in (1.4 and 0.4 m). The Desert Rock profiles had noticeable variation in the temperature of the bottom layer and a wider variation in the internal layers than UNR profiles.

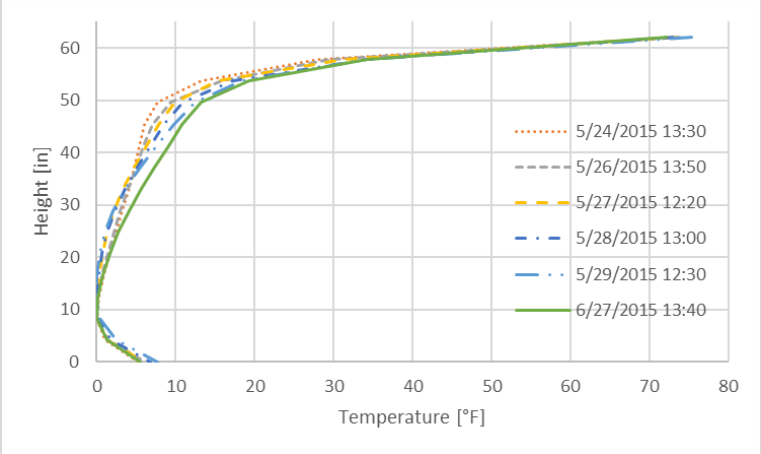

Figure 3-13-Temperature profiles (adjusted minimum temperature occurs of 0°F) through bridge depth on days exceeding 72°F (40°C) difference from UNR Weather Station data

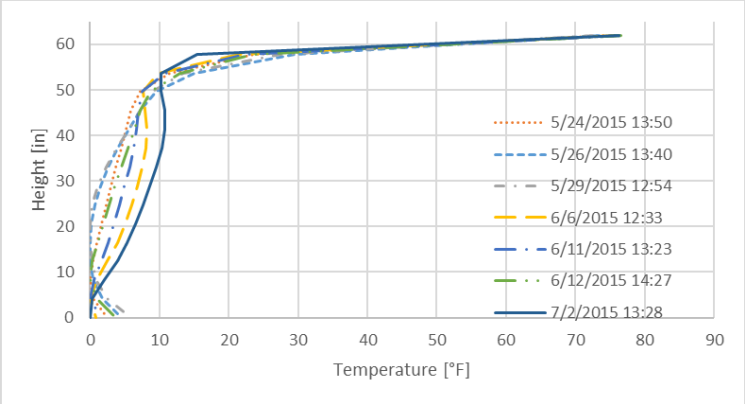

Figure 3-14-Temperature profiles (adjusted minimum temperature occurs of 0°F) through bridge depth on days exceeding 72°F (40°C) difference from Desert Rock SUFRAD Station data

The profiles adjusted to zero are compared to the Priestley fifth order gradient and the AASHTO LRFD Zone 1 gradient in Figure 3-15. The shape of the AASHTO gradient did not reflect the profiles calculated using heat flow analysis, while the Priestley gradient better estimated the profile shape. Since the Priestley gradient more closely matched the shape, the Priestley gradient was adjusted to have the same 72°F (40°C) temperature difference as the computed profiles. The adjusted Priestley gradient better represented the profiles calculated during early summer than the later summer profiles, especially those calculated for UNR.

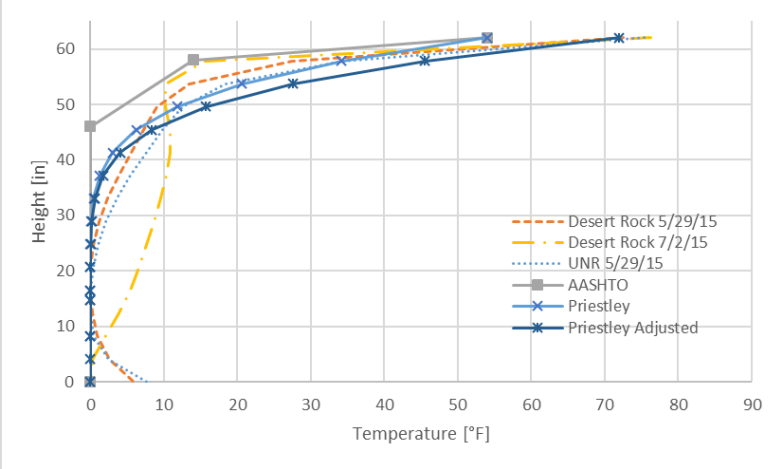

Figure 3-15-Adjusted profiles compared to AASHTO, Priestley and adjusted Priestley gradients

The pattern of temperature variation was different for a composite bridge section. The variation in temperature, over a 24-hour period, in the top, bottom and interface between concrete and steel on typical day from the UNR Weather Station are shown in Figure 3-16. Comparable data for a 24-hour period from the Desert Rock SUFRAD Station is shown in Figure 3-17. Only the top layer varied as the bottom steel layer and interface between materials remained at a near constant temperature over the 24-hour period. Steel is a more efficient heat conductor than concrete (heat conductivity is higher and specific heat is lower) and therefore the girder maintained a nearly constant temperature through depth of the girder. Figure 3-18 shows four temperature profiles computed from July 1st UNR Weather Station data while Figure 3-19 compares profiles computed from July 1st Desert Rock SUFRAD Station data. The profiles show the same oscillation between positive and negative gradients calculated for the concrete section.

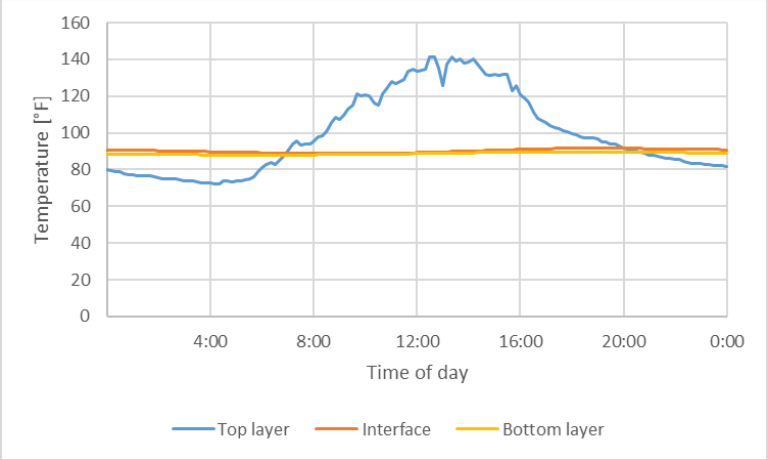

Figure 3-16-Composite section 24-hr temperature variation July 1, 2015 from UNR Weather Station data

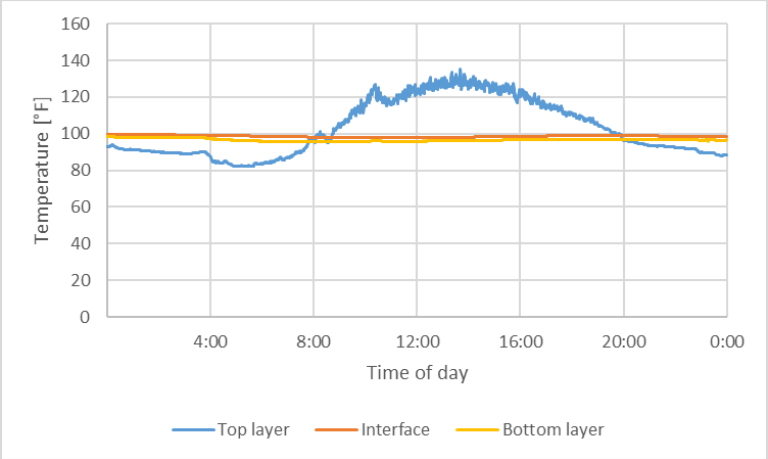

Figure 3-17-Composite section 24-hr temperature variation July 1, 2015 from Desert Rock SUFRAD Station data

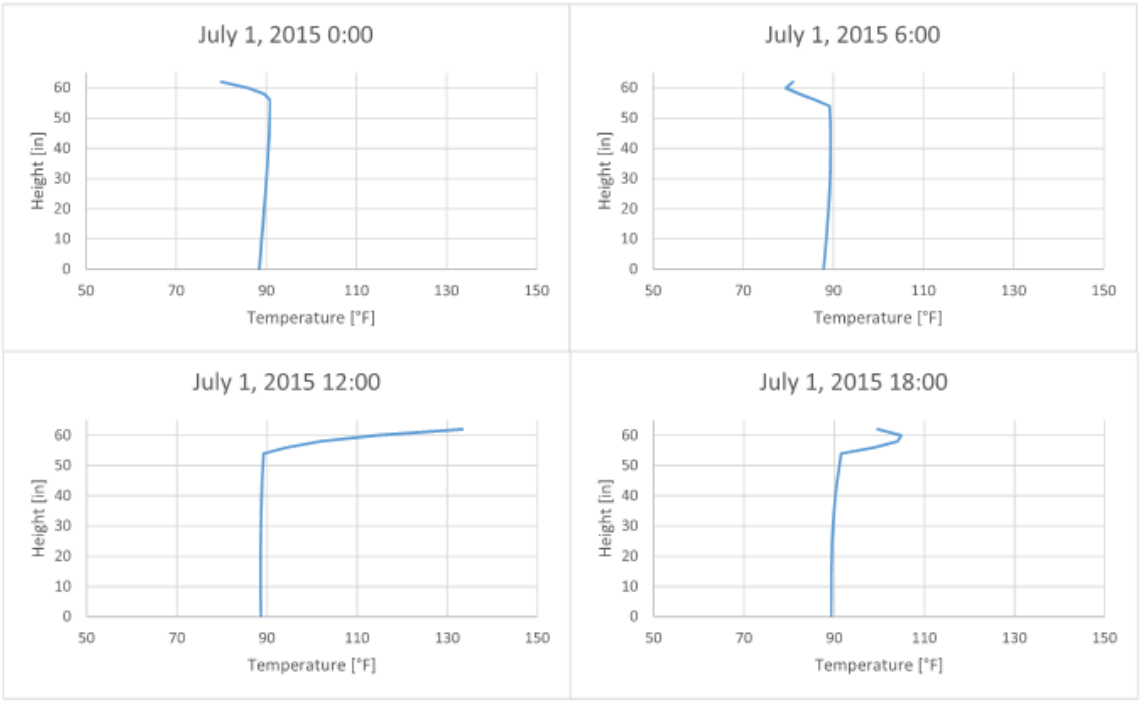

Figure 3-18-Composite section temperature profiles from UNR Weather Station data over the course of 24-hour period at six hour intervals

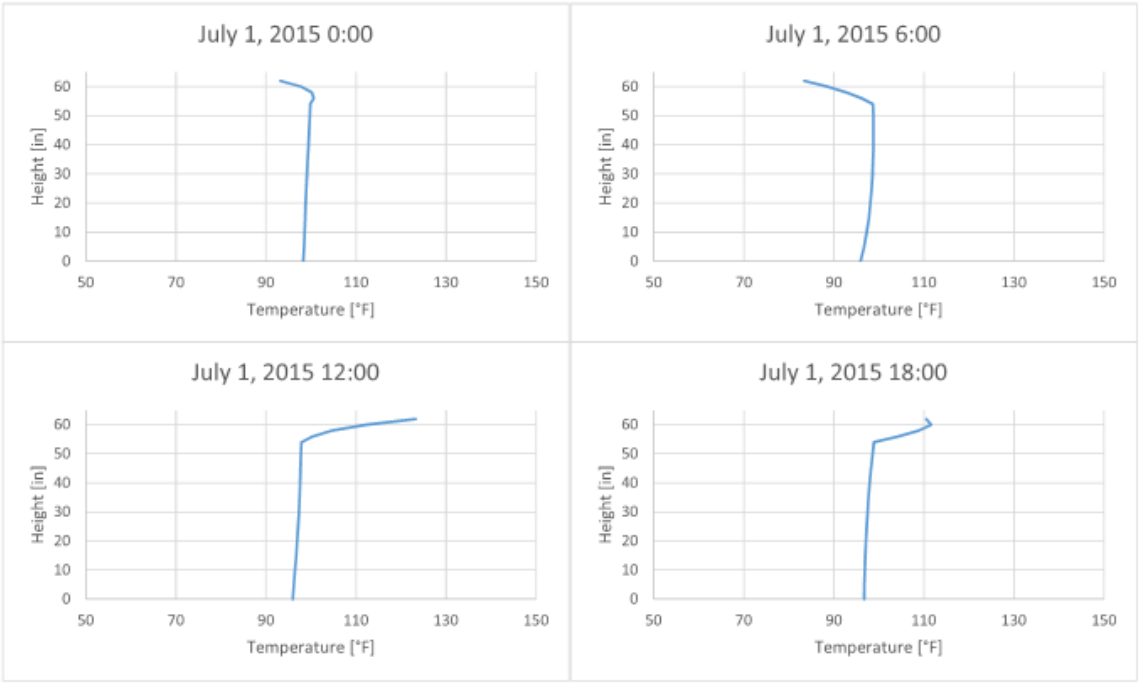

Figure 3-19-Composite section temperature profiles from Desert Rock SUFRAD Station data over the course of 24-hour period at six hour intervals

The process used to identify maximum positive thermal gradient for the concrete sections was also applied to the composite section. The difference between the temperature at the surface layer and lowest temperature of the internal layer was evaluated at each 10-minute interval for the UNR Weather Station results (Figure 3-20) and at each minute internal for the Desert Rock SUFRAD Station results (Figure 3-21). The temperature difference for both stations exceeded 54°F (30°C) during a significant portion of the examined time frame; however, the temperature difference never exceeded 72°F (40°C). The maximum temperature difference for the UNR Weather Station was 64.8°F (36°C) (Table 3-5) and 63°F (35°C) for the Desert Rock SUFRAD Station (Table 3-6). The reduction in maximum temperature difference compared to the concrete bridges was because nearly all the temperature change occurs through the deck of a composite bridge. A temperature change of a couple degrees through the girder was observed, but overall the girder temperature was nearly uniform.

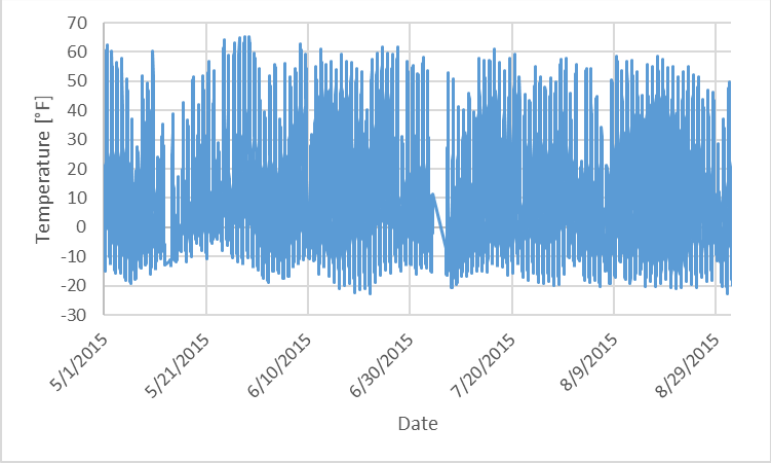

Figure 3-20-Composite section temperature difference from UNR Weather Station data

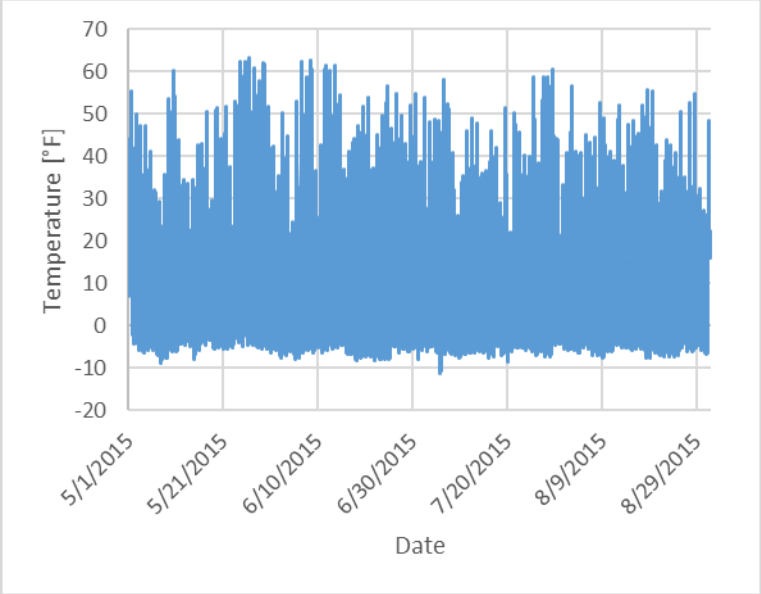

Figure 3-21-Composite section temperature difference from Desert Rock SUFRAD Station data

Table 3-5-Instances exceeding 64.8°F (36°C) temperature difference from UNR Weather Station data

Date	Time	Temperature Difference [°C]	Temperature Difference [°F]
5/27/2015	12:20	36.068	64.922
5/28/2016	13:00	36.255	65.259
5/29/2015	12:30	36.220	65.196

Table 3-6-Instances exceeding 63°F (35°C) temperature difference from Desert Rock SUFRAD Station data

Date	Time	Temperature Difference [°C]	Temperature Difference [°F]
5/26/2015	13:40	35.154	63.2772

The maximum temperature difference profiles for the UNR Weather Station data and the Desert Rock SUFRAD Station data are plotted in Figure 3-22 and Figure 3-23, respectively. The profiles calculated show that almost all the temperature change occurred in the concrete deck.

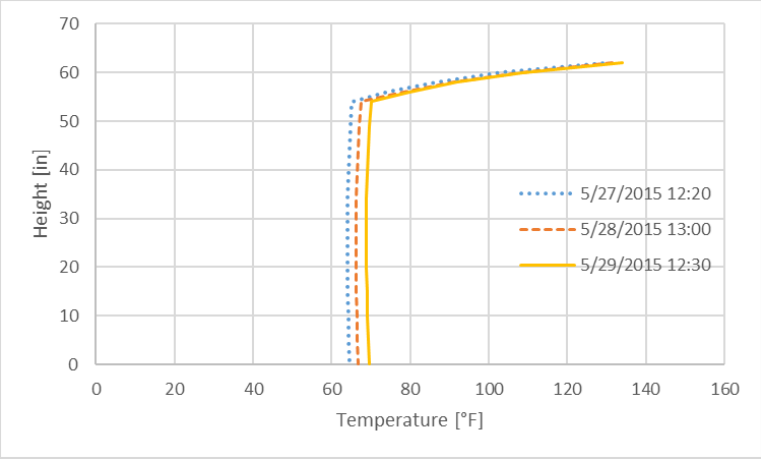

Figure 3-22-Temperature profiles with minimum 64.8°F (36°C) temperature difference from UNR Weather Station data

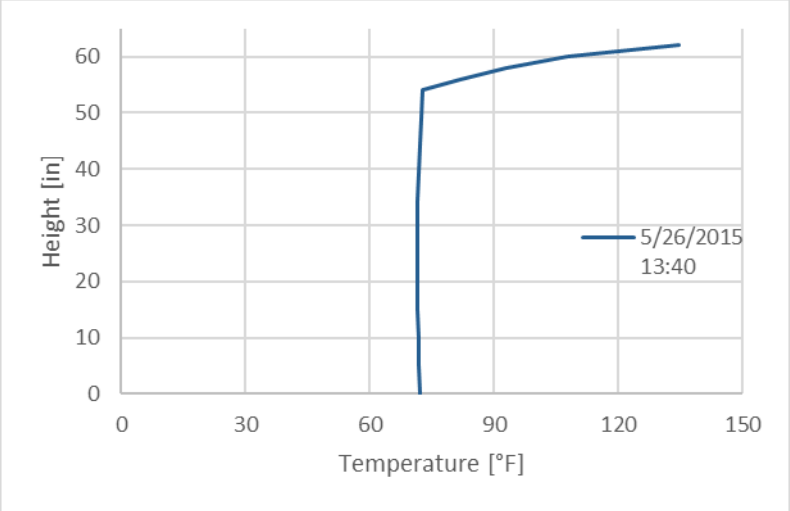

Figure 3-23-Temperature profiles with minimum 63°F (35°C) temperature difference from Desert Rock SUFRAD Station data

The calculated profiles from Desert Rock and UNR are compared to the AASHTO LRFD and AUSTROADS (1992) composite gradients in Figure 3-24. There was significant discrepancy between the uniform temperature in the girder in the profiles compared to the code thermal gradients. Unlike analysis of a concrete bridges section, the zero in thermal gradients does not refer to the minimum temperature, but rather to the temperature during construction. The discrepancy between calculated temperature profile and code thermal gradient may influence the thermal loading of a composite bridge. To isolate the change in temperature that occurs through the deck of the structure, the composite profiles and code gradients were adjusted such that the minimum temperature is equal to zero (Figure 3-25). The profiles calculated through heat flow had a larger temperature difference through the deck than either code recommendation.

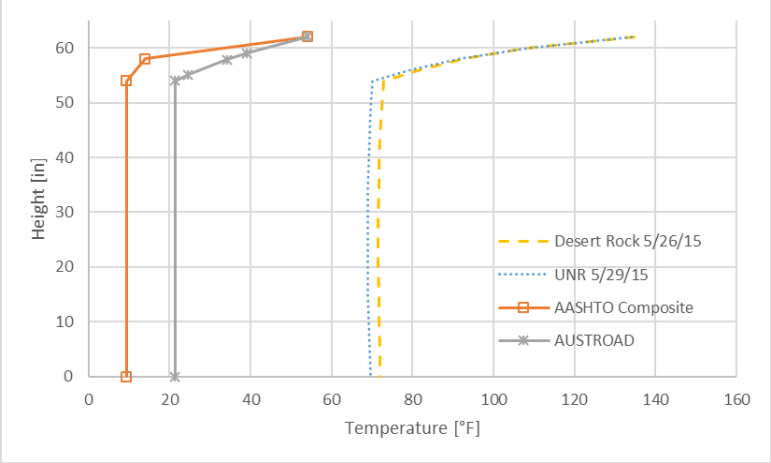

Figure 3-24-Temperature profiles compared to AASHTO and AUSTROADS gradients

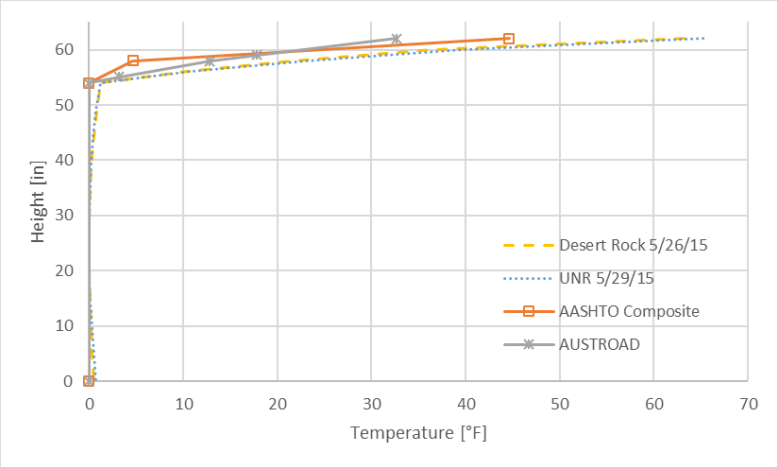

Figure 3-25-Temperature profiles, AASHTO and AUSTROADS gradients adjusted minimum temperature of 0°F

3.7. Conclusion

Applying heat flow analysis to a concrete section under the environmental condition present in Northern and Southern Nevada led to temperature profiles with larger temperature difference than the AASHTO LRFD Zone 1 thermal gradient used in design. Heat flow analysis preformed throughout the summer months allowed for long term trends to be analyzed as well as finding the maximum temperature difference to occur during to summer. The heat flow analysis revealed that most summer days had a positive temperature difference greater than the 54°F (30°C) maximum temperature difference of AASHTO. The shape of the profiles on days of highest temperature difference more closely reflected the Priestley fifth order gradient than the AASHTO gradient. The best fit to the profiles

calculated was a fifth order gradient with a temperature difference increased from 54°F (30°C) to 72°F (40°C).

Heat flow analysis on a composite section led to a much higher temperature difference than the AASHTO or AUSTROADS design thermal gradient. The profiles on the days of maximum temperature difference showed a temperature difference through the deck of 63°F (35° C) AASHTO temperature difference though the deck was only 45°F (25°C) and AUSTROADS was only 36°F (20°C). Discrepancy between the temperature in the girder of the calculated profiles and code thermal gradients was noted. Possible discrepancy in analysis of thermal loading may be caused by an incorrect assumption of temperature set to zero which would determine the uniform temperature in the girder. Therefore, both the calculated temperature profile and a temperature profile with the temperature in the girder set to zero were selected for analysis to capture any variation in result.

4. SOFTWARE VALIDATION STUDY

4.1. Introduction

CSiBridge finite element software is utilized by NDOT during the design of bridges. Thus, CSiBridge 2016 version 18.1.1 was used in this research to determine the effect of thermal gradient upon stresses in the superstructure and on bearing load distribution. Some limitations existed in applying thermal gradient in CSiBridge, therefore analytically calculated solution of bending moment were compared to bending moment calculated by CSiBridge to determine total error in using CSiBridge as an analytical software.

CSiBridge input limited the complexity of thermal gradients to five linear segments, preventing the application of a true fifth order gradient as recommended by Priestley and Buckle (1978). A concrete bridge was modeled to determine the effect of reducing a fifth order gradient to a piecewise linear approximation that was compatible with the input format for CSiBridge.

AASHTO provided equations to solve for the axial expansion, flexural deformation and internal stress due to thermal gradient loading for uniform material cross-sections; however, it did not provide specific guidelines for solving for the effect thermal gradient have on a composite bridge. The equations developed by Priestley and Buckle (1978) for concrete section were modified using transformed section analysis to develop equations for composite bridge sections. To validate using CSiBridge to analyze thermal gradient loading on composite bridge sections, a simple composite bridge modeled in CSiBridge with AASHTO Zone 1 composite thermal gradient was compared to the composite equations exact solution.

4.2. Modeling Considerations

As mentioned above, a nonlinear thermal gradient in CSiBridge can be modeled as a piecewise linear gradient with up to five linear segments (Figure 4-1). When a thermal gradient is applied as a load case to the bridge, the program converts the input nonlinear gradient to an equivalent linear thermal gradient that produces the same axial force, curvature and bending moment as the input nonlinear thermal gradient.

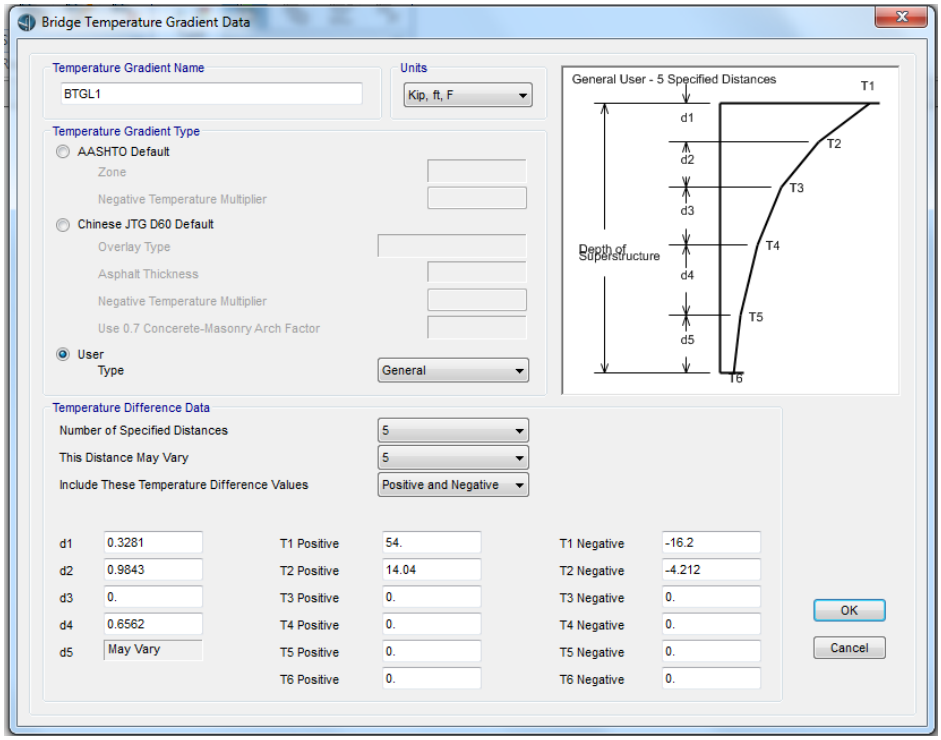

Figure 4-1-CSiBridge Thermal gradient input window (Source CSiBridge, 2016)

Two CSiBridge modeling approaches were considered: spine, and area. Spine models (composed of frame elements) only predict longitudinal curvature of the bridge. No transverse curvature is captured by spine models. The spine modeling approach is often preferred by analysts to reduce the processing time involved, and is the default approach used by NDOT. Area models (composed of shell elements) can be used to analyze transverse curvature of the bridge, which causes thermal loads to be distributed unequally to the bearings across a bent cap or abutment. The shell elements used as girders in the area model are oriented at 90 degrees from the deck and soffit elements such that the thickness of the element is the width of the girder. The area model of a composite bridge uses shell elements for the deck and frame elements for the individual girders. Both modeling approaches use frame elements for column and bent cap components.

For these verification studies, two thermal gradients were considered AASHTO, and Priestley. The AASHTO thermal gradients were exactly represented in CSiBridge as it is composed of three line segments. The fifth order gradient proposed by Priestley was approximated in CSiBridge by using a piecewise linear approximation. This introduced model error (inability of the model to exactly represent the system with its loads and boundary conditions) that is distinct from the error of the finite element method relative to an exact solution. For verification, CSiBridge results were compared to exact solutions for the fifth order gradient as well as a piecewise linear approximation of the fifth order gradient. Comparing CSiBridge results to the exact solution for a fifth order thermal

gradient identified the total error, which included both model and finite element method error. On the other hand, comparing CSiBridge analysis to an exact solution for a piecewise linear thermal gradient isolated the finite element method error.

4.3. Concrete Section Modeling Verification

Priestley and Buckle (1978) presented a simple method to solve for the support reactions and stresses caused by thermal gradients in an indeterminate bridge. First, the bridge was reduced to an unrestrained, determinate bridge by removal of intermediate pier supports. A determinate (single span) bridge subjected to thermal gradient loading develops a longitudinal curvature, as the bridge curves vertically to accommodate unequal longitudinal expansion through the superstructure cross-section depth. The curvature (ψ) induced take place in a determinate bridge is

$$\psi = \frac{\alpha}{I}\int t_{(y)} b_{(y)} (y - n) dy \tag{4-1}$$

where α is the coefficient of thermal expansion, I is the moment of inertia, $t_{(y)}$is the variation of temperature through depth of bridge cross section (along the y axis), $b_{(y)}$ is the variation in width through the depth, and n is the distance from the cross-section centroid and the arbitrary datum ($y = 0$).

The final strain (ε_o) at datum $y = 0$, where A is the area of the cross section, is,

$$\varepsilon_o = \frac{\alpha}{A}\int t_{(y)} b_{(y)} dy - n\,\psi \tag{4-2}$$

The primary stresses ($fp_{(y)}$) caused by nonlinear thermal gradients (primary stress goes to 0 if thermal gradient is linear) are a function of the final strain (Eq.4-2), the curvature of the bridge (Eq.4-1) and the thermal gradient expressed as

$$fp_{(y)} = E_c(\varepsilon_o + \psi * y - \alpha t_{(y)}) \tag{4-3}$$

The internal supports of an indeterminate structure resist the thermal curvature of the structure causing bending moment to develop. To reapply the internal restraints, fixed end moments (M) in an indeterminate structure are evaluated in terms of the modulus of elasticity (E), moment of inertia (I) and curvature (ψ) as

$$M = EI\psi \tag{4-4}$$

The fixed end moments that restrain the curvature are applied at the points where structure is released for the determinate analysis and at each bridge end and moment distribution is applied to solve for the bending moment distribution over the length and support reactions.

An indeterminate bridge also develops secondary stresses ($fs_{(y)}$) due to the bending moment that develops when thermal curvature is resisted by internal supports. These stresses are maximized at the location of the peak moment (M'), and can be expressed as

$$fs_{(y)} = \frac{M'(n-y)}{I} \quad (4\text{-}5)$$

The total stress ($ft_{(y)}$) in an indeterminate bridge at the location of the peak moment is expressed as

$$ft_{(y)} = fp_{(y)} + fs_{(y)} \quad (4\text{-}6)$$

Priestley and Buckle (1978) demonstrated the application of the stress and moment equations in an example. The example involved a three-span beam and slab bridge, the cross-section of the bridge is shown in Figure 4-2. The bridge superstructure total depth = 59.06 in. (1.5 m), and is composed of 7.87 in. (0.2 m) thick concrete deck and four identical 15.75 in. (0.4 m) wide concrete beam girders. The dimensions of a single girder with the effective deck width is shown in Figure 4-3. The end spans are 55.77 ft (17 m) long and the middle span is 82.02 ft (25 m) (Figure 4-4). The material properties assumed for the concrete are modulus of elasticity E = 4351.13 ksi (30 GPa), and coefficient of thermal expansion $\alpha = 5.56*10^{-6}°F^{-1}$ ($10^{-5}°C^{-1}$).

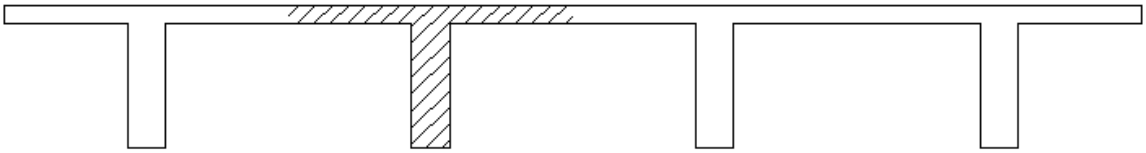

Figure 4-2-Bridge cross section

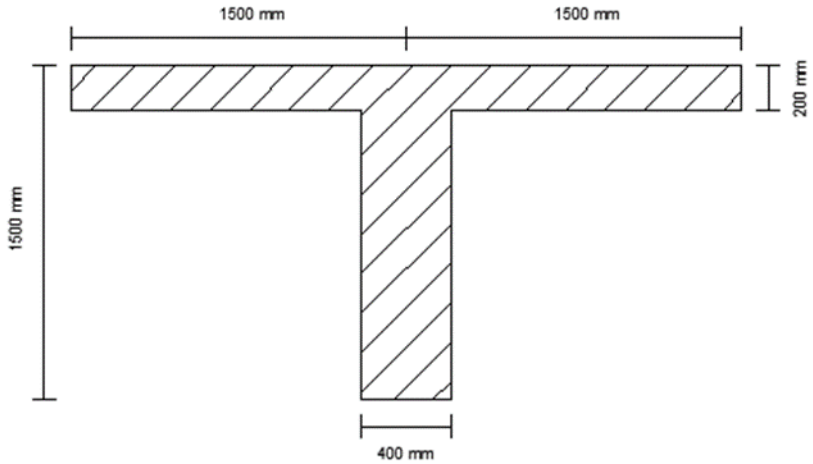

Figure 4-3-Single girder cross section

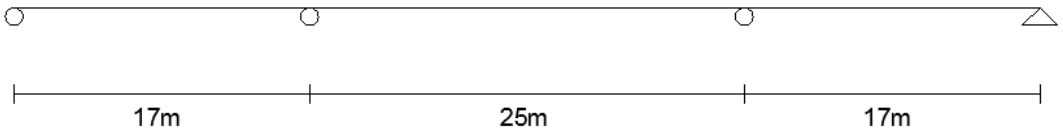

Figure 4-4-Span dimensions

To isolate model error resulting from limited thermal gradient input of CSiBridge, the example problem was solved using a piecewise linear approximation of the fifth order gradient (shown in Figure 4-5) in Appendix A. The piecewise linear approximation was represented by four discrete segments (7.87 in. (0.2 m), 7.87 in. (0.2 m), 11.81 in. (0.3 m), and 19.69 in. (0.5 m) deep), and a fifth segment with temperature = 0 that encompassed the remaining depth (> 47.24 in. (1.2 m)).

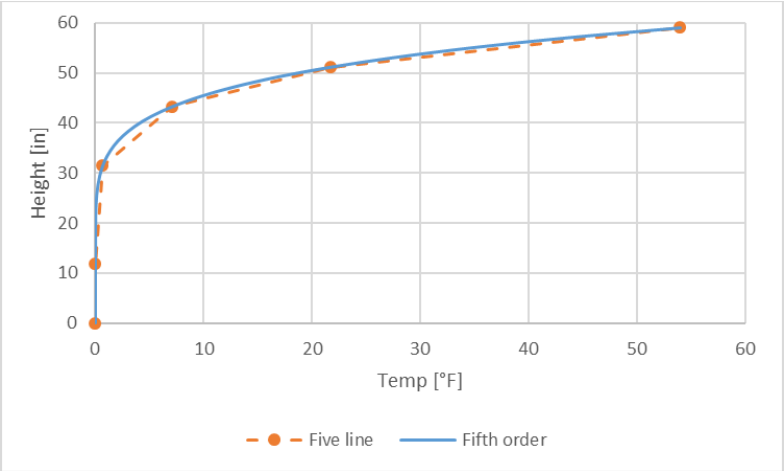

Figure 4-5-Fifth order gradient vs piecewise linear approximation

Three methods of solving for the maximum bending moment and stress distribution were compared to the exact solution of a fifth order gradient: exact solution, a CSiBridge spine model and a CSiBridge area model—all subjected to the approximate piecewise linear gradient.

The support boundary conditions were applied at the neutral axis by defining the bearing elevation at the neutral axis. Rollers were applied at both abutments and pin supports at the piers. A spine model was developed from frame elements, where a single element represents the entire superstructure.

An area model was developed using thin shell elements for girder and deck components. The area model was discretized by; segment length along the longitudinal direction and submesh size in longitudinal and transverse directions. The maximum moments due to thermal gradients calculated using three segments lengths with varying submesh sizes are

compared in Figure 4-6. Segment length was observed to have no effect on the analysis of thermal gradients, while submesh size only slightly effected the results of thermal gradient loading. Thus, the selected parameters for the deck spans of the area and spine models were maximum segment length = 3.28 ft (1 m) and maximum submesh size = 1.97 ft (0.6 m) which optimized convergence and processing time.

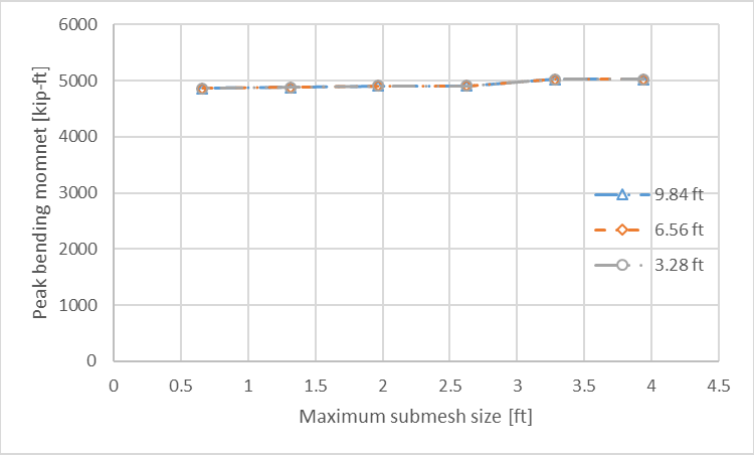

Figure 4-6-Peak bending moment variation due to model discretization (three segment lengths with altered submesh size)

The bending moment diagram from the Priestley and Buckle example bridge with an applied fifth order gradient is shown in Figure 4-7. The maximum moments from the CSiBridge models and the exact solution to a piecewise linear gradient were all larger than the maximum moments due to a fifth order gradient; the absolute error is shown in Figure 4-8. The CSiBridge spine model produced a maximum moment closest to the exact solution to a piecewise linear gradient. The area model had the largest total error; however, the peak moment of all three solutions relative to the exact solution of a fifth order gradient had less than 10% error, shown in Figure 4-9.

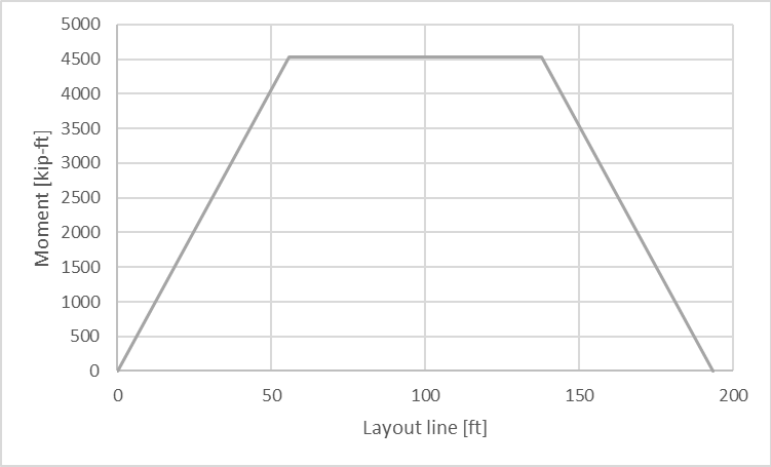

Figure 4-7-Priestley and Buckle example bending moment diagram

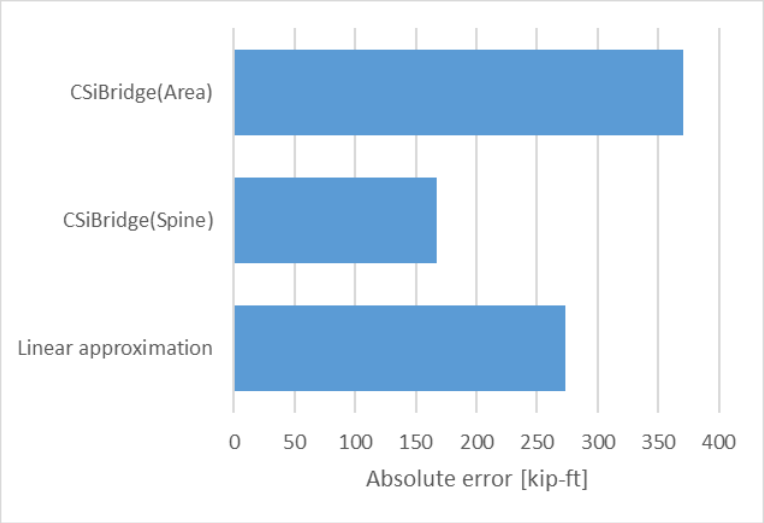

Figure 4-8-The absolute error in peak moment for three methods of solving relative to the exact solution to a fifth order gradient

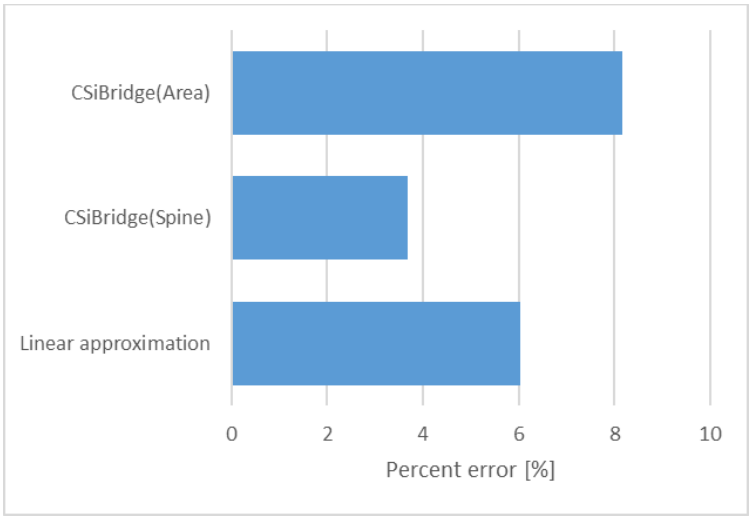

Figure 4-9-The percent error in peak moment for three methods of solving relative to the exact solution to a fifth order gradient

To isolate the error in the finite element method, the absolute error of the comparison of peak moment from the two CSiBridge models to the piecewise linear approximation is shown in Figure 4-10. The area model overestimated and the spine model underestimated the peak bending moments of the exact solution of a piecewise linear gradient. The error due to finite element method was less than 2.5% for both CSiBridge models (Figure 4-11). The percent error in the CSiBridge models relative to the piecewise linear approximation was significantly lower than the CSiBridge models relative to the fifth order gradient. The total error in using CSiBridge to calculate thermal effects in a concrete bridge section was primarily a result of model error due to limited input rather than finite element method error. The area models produced a peak bending moment closer to the solution of the piecewise linear approximation than the spine model.

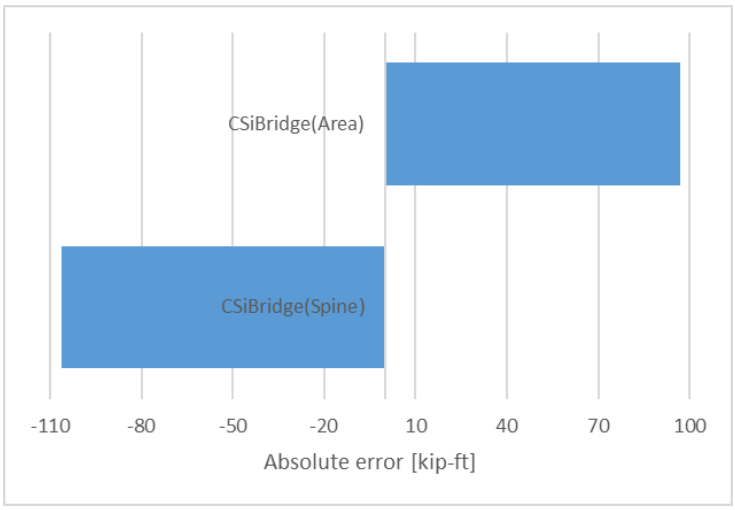

Figure 4-10-The absolute error in peak bending moment for CSiBridge models relative to the exact solution to piecewise linear gradient

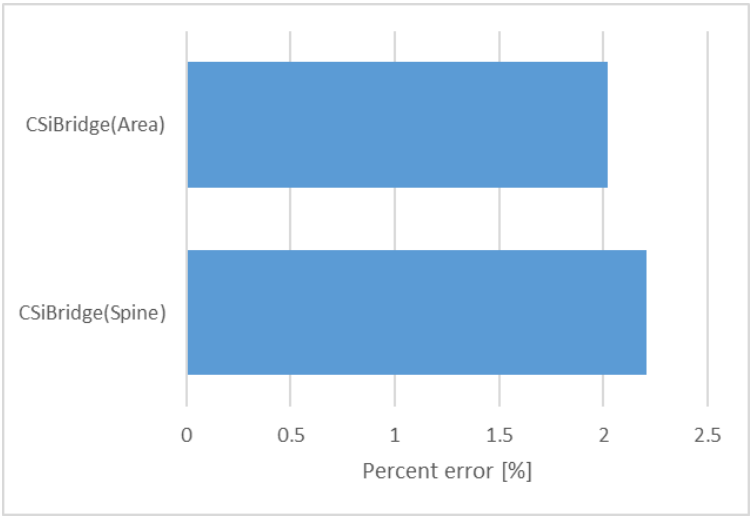

Figure 4-11-The percent error in peak bending moment for CSiBridge models relative to the exact solution to piecewise linear gradient

Only the secondary stresses of thermal gradients were considered by CSiBridge. The stresses due to a piecewise linear approximation compared to the results of CSiBridge area model are shown in Figure 4-12. Since CSiBridge applies nonlinear thermal gradients as an equivalent uniform temperature load and linear thermal gradient self-equilibrating stresses were not included the results of either model. Revision of the application of thermal gradients in CSiBridge is a planned improvement; currently analytically calculated

solutions are the best way to solve for self-equilibrating stresses caused by nonlinear thermal gradients

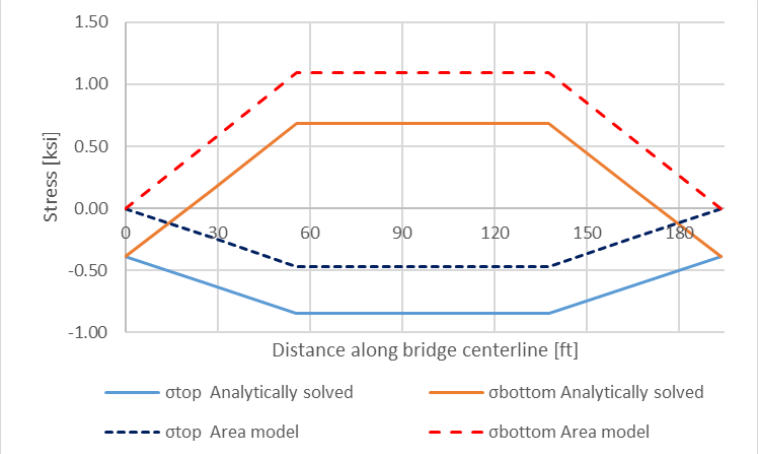

Figure 4-12-Top and bottom fiber stress comparison

4.4. Composite Section Modeling Verification

The equations in AASHTO LRFD (2010) for analyzing the effect of thermal gradients were based on the derivations of Priestley and Buckle (1978), which only considered a uniform material section. The equations used by AASHTO to develop an exact solution for a concrete bridge section were modified with transformed section analysis to develop an exact solution for composite bridge sections.

Priestley and Buckle solved for strain and curvature in a concrete section subjected to a thermal gradient by setting the axial force and internal moment equations equal to zero. Equations appropriate for composite bridge section were developed for this research by separating the equations into steel and concrete segments and using transformed section analysis to convert the steel sections to equivalent concrete sections using the modular ratio ($\frac{E_s}{E_c}$). The derivations of the equations for composite sections can be found in Appendix B. The resulting strain equation for a composite section is:

$$\varepsilon_0 = \frac{\alpha_c \int_{di}^{dt} t_{(y)} b_{(y)} dy - \psi n A_c + \frac{E_s}{E_c} \alpha_s \int_{db}^{di} t_{(y)} b_{(y)} dy - \frac{E_s}{E_c} \psi n A_s}{(A_c + \frac{E_s}{E_c} A_s)} \qquad (4\text{-}7)$$

The curvature equation for a composite section is:

$$\psi = \frac{\alpha_c \int_{di}^{dt} t_{(y)} b_{(y)} (y-n) dy + \frac{E_s}{E_c} \alpha_s \int_{db}^{di} t_{(y)} b_{(y)} (y-n) dy}{(I_c + \frac{E_s}{E_c} I_s)} \qquad (4\text{-}8)$$

where I_c and I_s are taken about the transformed section centroid and n is the distance from the transformed section centroid and the arbitrary datum ($y = 0$). The fixed end moments are determined using Eqn. (4-3) with the transformed section moment of inertia, which is expressed as:

$$M = E_c (I_c + \frac{E_s}{E_c} I_s)\, \psi \qquad (4\text{-}9)$$

A CSiBridge spine model and an area model of an example bridge were compared to the exact solution for a composite section, derived in Appendix C using Equations (4-8) and (4-9). The example bridge cross section shown in Figure 4-13, is composed of a 12 in. (0.3 m) concrete deck and four steel I-beam girders with dimensions shown in Figure 4-14. The bridge has two 50 ft (15.24 m) spans as shown in Figure 4-15. The concrete modulus of elasticity = 3605 ksi (24.86 GPa) and a coefficient of thermal expansion = $5.5*10^{-6}°F^{-1}$ ($9.9*10^{-6}°C^{-1}$). The steel modulus of elasticity = 29000 ksi (199.95 GPa) and a coefficient of thermal expansion = $6.5*10^{-6}°F^{-1}$ ($1.17*10^{-5}°C^{-1}$). The AASHTO (2010) composite gradient for Zone 1 was applied to a representative girder (Figure 4-16).

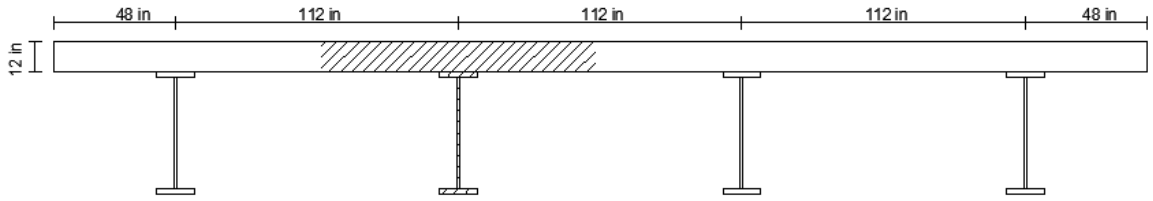

Figure 4-13-Composite bridge cross section

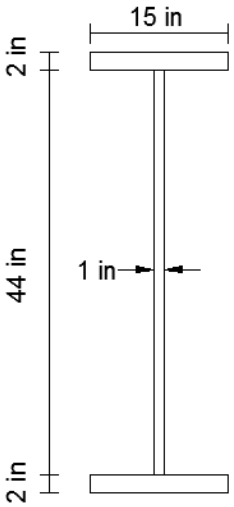

Figure 4-14-Steel girder dimensions

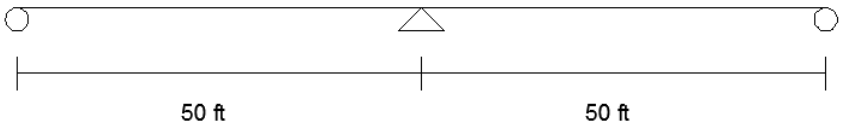

Figure 4-15-Span dimensions

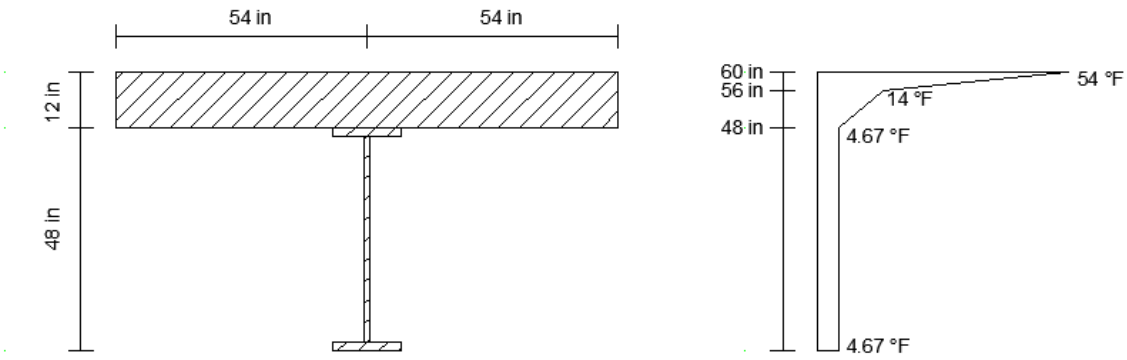

Figure 4-16-Representative single girder cross section with AASHTO thermal gradient

The modeling assumption were the same as for the concrete section except for the following changes. The area model built in CSiBridge used thin shell element for the deck component of the superstructure and a separate frame elements for each girder. Similar

exercise testing the discretization of the area model was used to choose segment length of 2 ft (0.61 m) area and spine models with a maximum submesh of 1 ft (0.30 m) which optimized convergence and processing time.

The bending moment diagram calculated using the composite section exact solution is shown in Figure 4-17. Comparing the maximum moments from the CSiBridge models to the moment from the composite section exact solution, the maximum moments of both models were smaller than expected. The absolute error of the comparison to the piecewise linear approximation is shown in Figure 4-18. The percent error in the CSiBridge models relative to the composite section exact solution was less than 4% for both models (Figure 4-19).

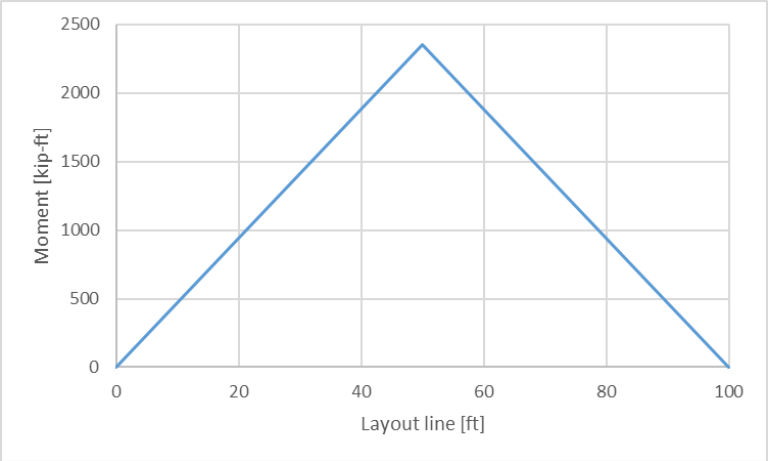

Figure 4-17-Composite section exact solution bending moment diagram

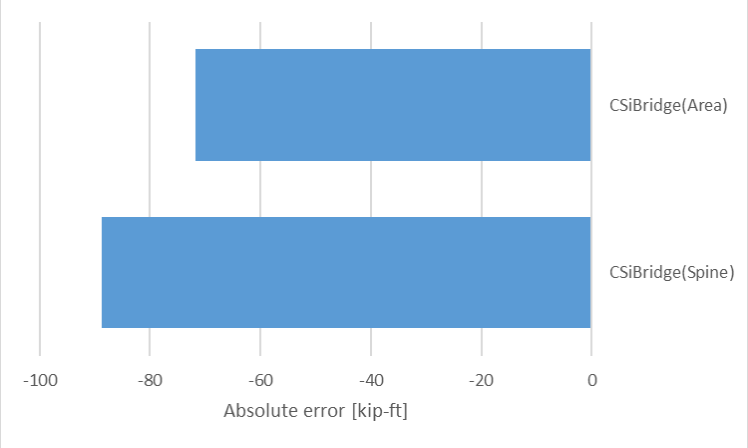

Figure 4-18-The absolute error in peak bending moment for CSiBridge models relative to composite section exact solution

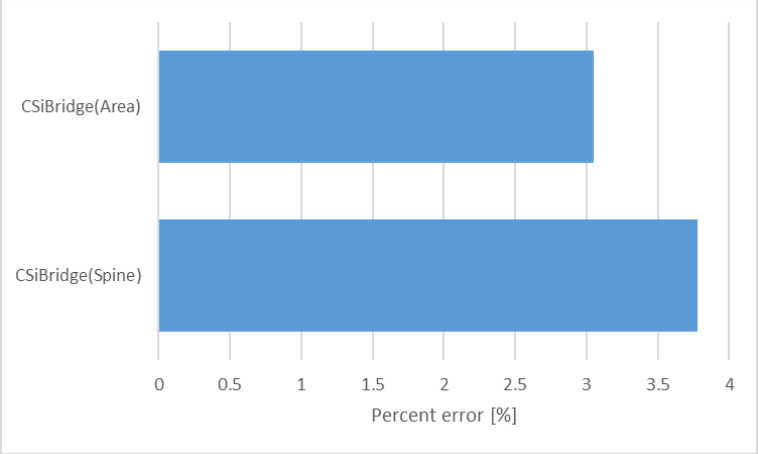

Figure 4-19-The percent error in peak bending moment for CSiBridge models relative to composite section exact solution

4.5. Conclusions

Altering the thermal gradient from a fifth order gradient to a piecewise linear approximation (necessary for input in CSiBridge) increased the peak bending moment developed in the bridge superstructure. The error in both CSiBridge models relative to the exact solution of fifth order gradient were under 10%. The error was significantly reduced when the models were compared to the piecewise linear approximation (less than 3%). Model error due to input limitations of CSiBridge was a larger component of the total error than finite element method error; however, the modeling results were sufficiently accurate to the exact solution for the fifth order thermal gradient to investigate the effects of thermal gradient on bearing load in a concrete bridge.

Less than 4% error in the moment was observed in CSiBridge models relative to equations developed to give an exact solution for analysis of composite section under thermal gradient loading.

The finite element method errors were comparable for area and spine models, therefore both model were considered in subsequent analysis for comparison to exact solution. However, since only area models can evaluate the transverse distribution of bearing loads due to thermal gradients, CSiBridge area models were used for determining bearing loads and stresses.

5. THERMAL ANALYSIS OF AIRPORT CONNECTOR OVER WRIGHT BROTHERS LANE

5.1. Introduction

To examine the effect of thermal gradient on the bridge bearings, a two-span post-tensioned concrete box girder bridge was selected for analysis in this research. The maintenance records for the bridge indicated bearing pad issues that could be related to thermal gradients loading A model of the bridge was built in CSiBridge per the as-built drawings.

Restraint of the longitudinal curvature of the bridge caused by the positive thermal gradients induced self-equilibrating loads on a two-span bridge. The abutments incurred a downward force while the pier incurred an uplift force. However, as there are no bearings in the integral bent cap at the pier, the shear force at the pier was not considered for bearing load analysis. The variation of stresses in top and bottom fiber of the superstructure along the longitudinal axis due to thermal gradient loads were also considered.

The bridge was analyzed under the following range of thermal gradients that might occur in a concrete bridge in the southwest: the AASHTO Zone 1 positive and negative gradients, a fifth order gradient with maximum temperature difference as recommended by AASHTO Zone 1, and a fifth order gradient with maximum temperature difference taken from the heat flow analysis (Figure 3-15). The superstructure stresses and bearing loads due to thermal loading and load combination Service I and III were compared to AASHTO LRFD design limits to evaluate the influence using different thermal conditions.

5.2. Bridge Characteristics

A post-tensioned concrete box girder bridge located in Las Vegas, Nevada (built in 1994) carries the southbound two lanes of the McCarran airport connector over Wright Brothers Lane, hereafter referred to as “Airport Connector”. This bridge was selected due to the bearing issues indicated by maintenance records that could have been caused by thermal gradients. The two-span 300-foot (91.44 m)-long bridge is curved with a centerline radius of 425 ft. The bridge is composed of a three-cell box girder with an integral cap supported by a single column at the pier and seat type abutments. Figure 5-1 shows the plan view of the Airport Connector with the three cells of the box girder bridge superimposed. Four bearings pads are located at each abutment at the base of the girders.

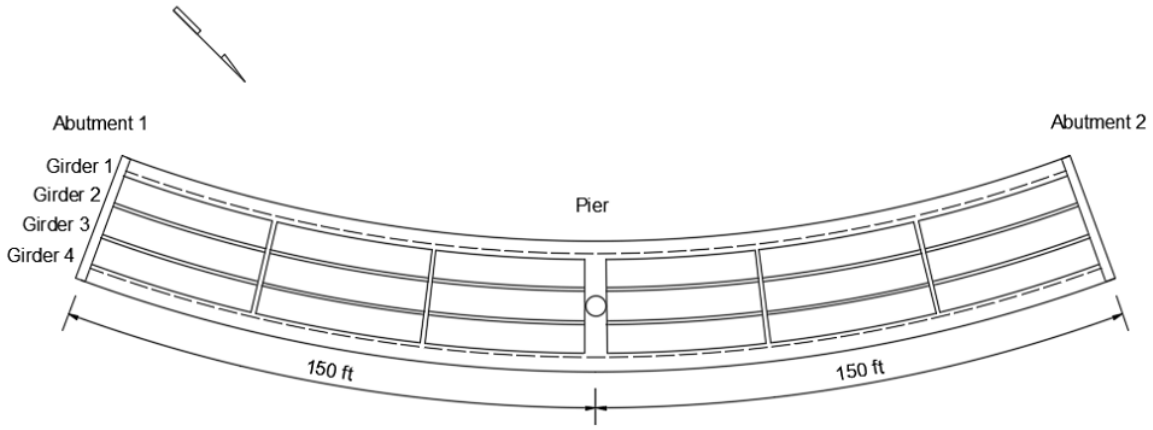

Figure 5-1-Plan view of the Airport Connector box girder bridge

The bridge width of 39 ft (11.89 m) is between outer deck edges with 24 ft (7.32 m) of road width. Concrete railings 16 in. (0.41 m) wide and 32 in. (0.81 m) tall are located at each edge of the cross section. The box girder total depth is 78 in. (1.98 m) with an included deck thickness of 8.5 in. (0.22 m) and soffit thickness of 6 in (0.15 m). The interior girder thickness is 12 in. (0.30 m) while the exterior girders have a thickness of 14 in. (0.36 m) at the top of the girder and increase to more than 24 in. (0.61 m) at the curved bottom of the girder. The deck overhang length from the outside of the exterior girder is 48 in. (1.22 m) with a thickness of 8.5 in. (0.22 m) at the tip and a thickness of 14 in. (0.36 m) at the intersection with the exterior girder. The cross-section dimensions of the box girder are shown in Figure 5-2 while the dimensions of the diaphragm at each abutment are shown in Figure 5-3.

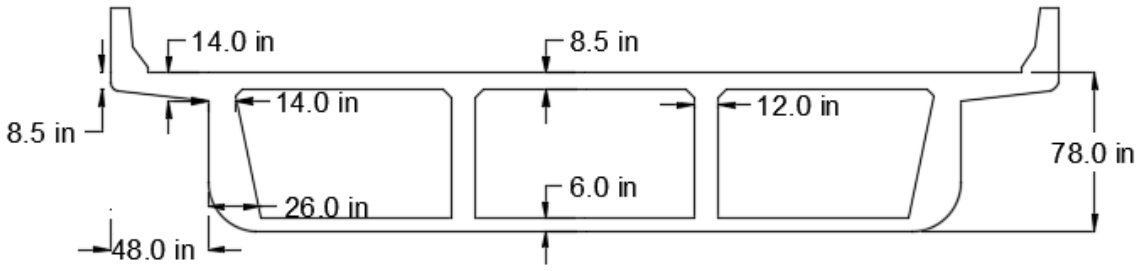

Figure 5-2-Cross-section view of the Airport Connector box girder bridge

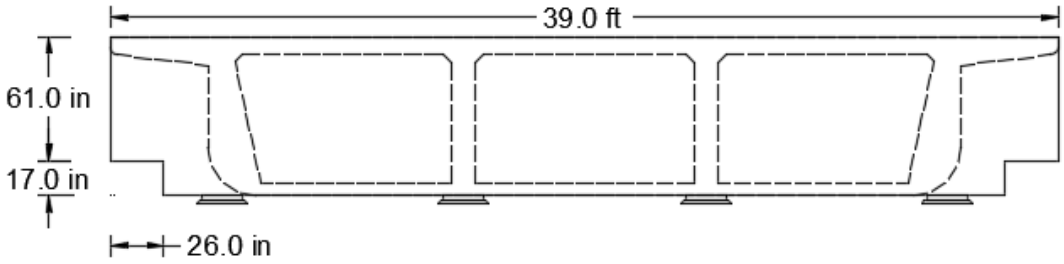

Figure 5-3-Cross-section view of the Airport Connector diaphragm at abutment with bearings under girders

The elevation of the bridge is shown in Figure 5-4. The solid diaphragm at each abutment are 33 in. (0.84 m) thick, the integral bent cap at the pier is 78 in. (1.98 m) thick and the cross frames dividing each span into thirds are 8 in. (0.20 m) thick. The column at the pier is 72 in. (1.83 m) in diameter, with a clear height of 25.25 ft (7.70 m) to the square footing 22.5 ft (6.86 m) in plan and 57 in. (1.27 m) thick.

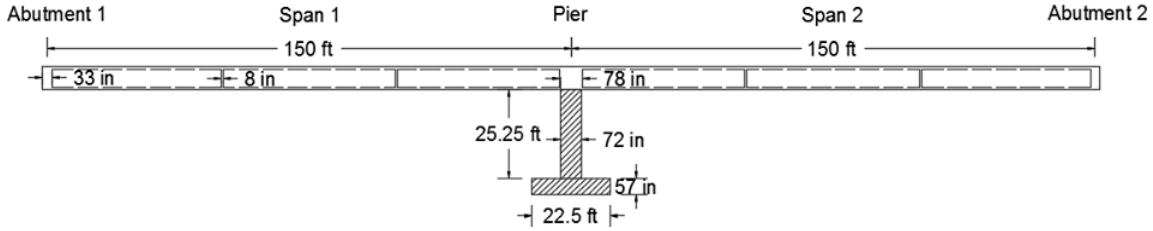

Figure 5-4-Elevation of the Airport Connector along layout line

The bearings on the bridge are steel-reinforced neoprene pads of 70 Durometer hardness 20 in. (0.51 m) by 20 in. (0.51 m) in plan and 2.5 in. (0.06 m) thick, not including steel layer thickness. Fourteen-gauge steel shims separate the bearing laminations: 0.25 in. (6.35 mm) thick exterior lamination and 0.5 in. (12.7 mm) thick interior lamination. The centerline of each bearing is aligned with the centerline of the abutment diaphragms longitudinally and girder centerline transversely.

The concrete has an initial strength of 4,000 psi (27.58 MPa) and an ultimate strength of 5,000 psi (34.47 MPa). The reinforcing steel is AASHTO M31 (ASTM A615) Grade 60. The prestressing steel is comprised of 0.6 in (.015 m) diameter, 7 wire low relaxation 270 ksi (1.86 GPa) strands with a steel modulus of 28,000 psi (193.05 MPa).

The Airport Connector as-built drawings specify post-tensioned steel in the configuration shown in Figure 5-5. The final post-tensioned force, after all losses, applied to the southbound abutment is 9,154 kips (40.72MN), which is distributed among the four girders of the bridge. The secondary forces resulting from pre-stressed steel affect the bridge like a positive thermal gradient, causing an upward curvature in the bridge.

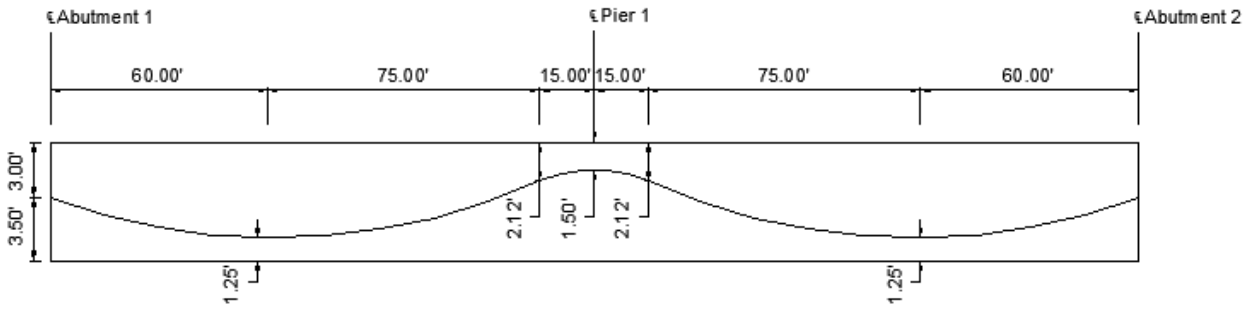

Figure 5-5-Airport Connector Bridge posttensioning steel diagram

5.3. Modeling Assumptions and Verifications

The central angle of a single span of the bridge is 20.22°. Section 4.6.1.2.3 of AASHTO (2010) allows a bridge with a central angle less than 34° within one span to be modeled as a straight bridge. Thus, the curvature was not included in the CSiBridge model.

Both area and spine models were generated in CSiBridge and analyzed to determine the load transferred to the bearings under dead load, live load, prestressing and thermal gradient loading. To verify the accuracy of area and spine models, the moments at the pier and abutment support reactions resulting from AASHTO LRFD Zone 1 positive thermal gradient were compared to the analytically calculated solutions in Appendix D.

The area model used shell elements for superstructure components (deck, girder and soffit). The integral bent cap and column were the only frame elements. The spine and area model both used a maximum segment length 5 ft (1.52 m) while the area model also had a maximum submesh size of 2 ft (0.61 m). The spine model used frame element for the entire superstructure cross section; with a maximum segment length of 5 ft (1.52 m). In both models the base of the single column was fixed, while roller supports were specified at abutment bearing location only restrain movement in the vertical direction. The results of the CSiBridge analysis with AASHTO LRFD Zone 1 thermal gradient loading are shown in Table 5-1.

Table 5-1-Peak bending moment and support reactions due to AASHTO thermal gradient

Model	Moment [k-ft]	Abutment 1 Force [k]	Abutment 2 Force [k]
Analytical	7128.2	47.52	47.52
Spine	7453.38	49.69	49.69
Area	7797.03	51.98	51.98

The percent error for bending moment results from CSiBridge relative to the exact solutions of the AASHTO LRFD Zone 1 thermal gradient was less than 5% when using spine models, but increased to just under 10% for the area model. In the next section the area model was used for evaluating the stresses in the superstructure and forces present in

bearings due to the spine model inability to solve for transverse distribution of bearing load.

5.4. Analysis

To evaluate the effect of the thermal gradient shape and temperature difference, stresses and bearing loads predicted by four alternative gradients were compared. The gradients of interest, shown in Figure 5-6, were the current AASHTO LRFD Zone 1 positive gradient (referred to as "AASHTO"), the AASHTO LRFD Zone 1 negative gradient (referred to as "AASHTO-negative"), the fifth order gradient with the same maximum temperature as the AASHTO requirements (referred to as "Fifth order"), and a fifth order gradient adjusted to the maximum temperature difference of 72°F (40°C) found in the heat flow analysis (referred to as "Adjusted fifth order").

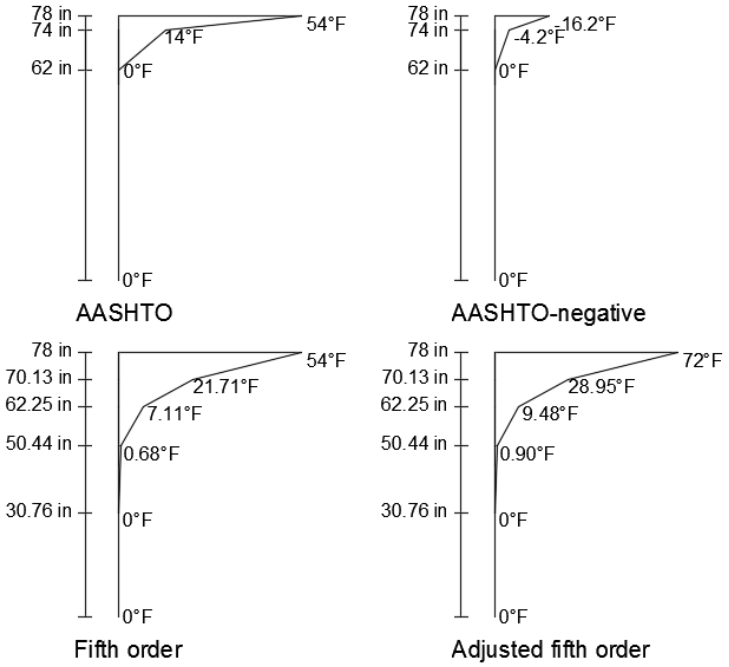

Figure 5-6-Thermal gradients applied to the Airport Connector bridge

As mentioned in Chapter 4, limitations of CSiBridge are that the fifth order gradient must be simplified to five linear segments, and the primary stresses due to thermal gradients are not calculated by the software. To compensate, the primary stress distribution of the four gradients were evaluated analytically using piecewise linear approximation of the fifth order gradient (Figure 5-7). The primary stresses through the depth of the section were affected by the shape of the gradient. While the primary stress distribution of the adjusted fifth order gradient caused higher internal tension and compression in the bottom fiber than the other three gradients, the AASHTO gradient caused the largest compressive stress in the top fiber of the bridge. The secondary stresses at the pier support of the bridge (location of peak bending moment) are shown in Figure 5-8, and were combined with primary stresses to derive total thermal stresses at the pier support in Figure 5-9. Of the four

gradient, the largest compressive stress in the top fiber and the largest tensile stress in the bottom fiber of the bridge section was caused by the adjusted fifth order gradient. Considering total thermal stresses, fifth order and AASHTO gradients led to similar compression values for the top fiber of the bridge but produced very different tension values in the bottom fiber. The adjusted fifth order gradient caused a larger maximum compression and tension value than both AASHTO and fifth order gradients.

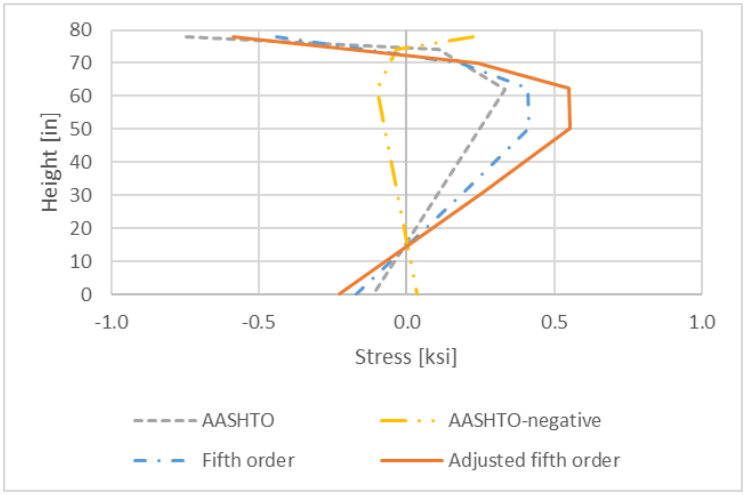

Figure 5-7-Primary thermal stress for different input thermal gradients (compression is negative)

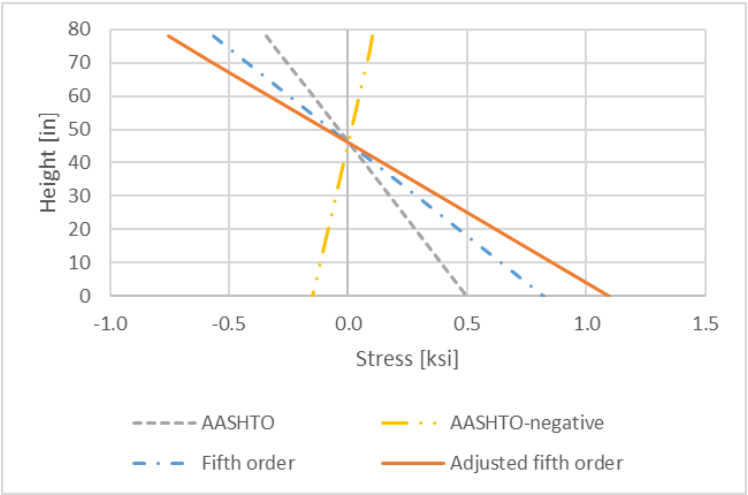

Figure 5-8-Secondary thermal stresses at pier support (compression is negative)

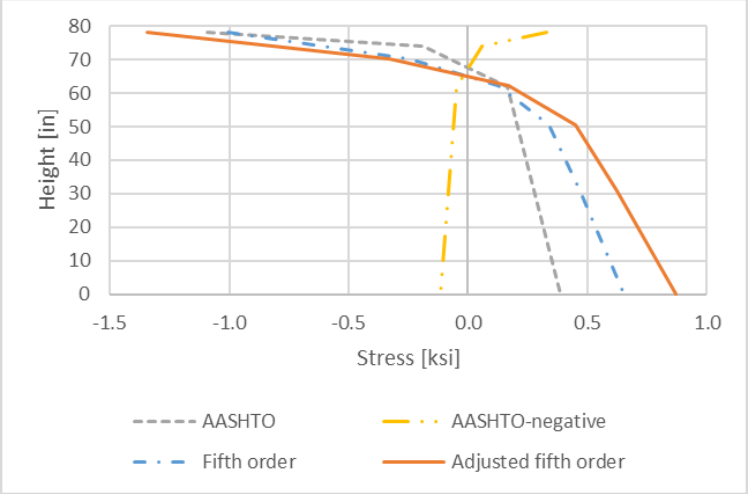

Figure 5-9-Total thermal stresses at pier support (compression is negative)

Figures 5-10 and 5-11 present the predicted moments at the pier, and support reactions at Abutment 1, respectively. The reactions due to the fifth order gradient and the adjusted fifth order gradient were more than 150% and 200% of the AASHTO gradient reactions, respectively.

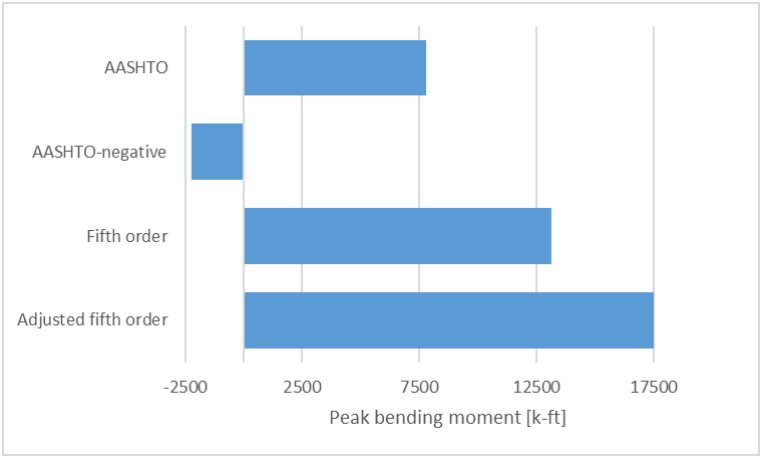

Figure 5-10-Peak bending moment at pier due to thermal gradients

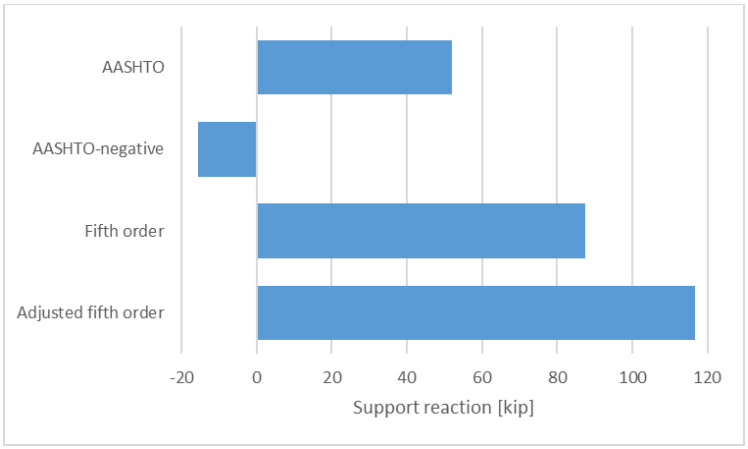

Figure 5-11-Support reaction at Abutment 1 due to thermal gradients (uplift is negative)

The area model results also indicated the transverse thermal curvature caused by thermal gradient applied through the diaphragms at the abutments and pier had significant influence on the transverse distribution of load on the bearings. Figure 5-12 shows the influence of the varying gradient on the support reactions of each bearing at the four girders. The loads were distributed such that the exterior bearings experienced increased loading while the interior bearings experienced uplift, except for the AASHTO negative gradient, which induced an opposite trend to the positive gradient.

Figure 5-12-Distributed bearing loads due to thermal gradient (uplift is negative) at Abutment 1

The overall effect of thermal stresses was evaluated by comparing total stress due to AASHTO load combinations to the AASHTO prestressed concrete stress limits. The compression limits (Table 5.9.4.2.1-1 of AASHTO (2010)) applied to compression stresses caused by load combination Service I, while the tension limits (Table 5.9.4.2.1-2 of

AASHTO (2010)) applied to tension stresses caused by load combination Service III. These load combinations involved the factored combination of the dead load of structural components and nonstructural attachments (DC), vehicular live load (LL), secondary forces of pre-stressing (PS) and force effect due to thermal gradient (TG) (AASHTO, 2010). AASHTO LRFD load combination Service I is expressed as:

$$1.0DC + 1.0LL + 1.0PS + 0.5TG \quad (5\text{-}1)$$

AASHTO LRFD load combination Service III is expressed as:

$$1.0DC + 0.8LL + 1.0PS + 0.5TG \quad (5\text{-}2)$$

The dead load of structural components included weight of the deck, webs and soffit. Dead load of nonstructural attachments included the railings and wearing surfaces. Live load was determined by calculating the maximum effect for each component caused by a design vehicle moving load. The live load for bearings was determined by solving for the maximum shear at the abutments. The live load for the stresses in the bridge was determined by solving for peak bending moment at mid-span. For these circumstances, the design vehicular live load (HL-93) was controlled by the combination of design truck load (HS-20) and design lane load.

The combined stresses due to dead, live, and prestressing loads were taken as reported by CSiBridge and added to thermal stresses that were analytically calculated, since CSiBridge does not report the primary stress due to thermal gradients.

The stresses in the top fiber and bottom fiber of the bridge due to load combination Service I are shown in Figure 5-13 and Figure 5-14 respectively. The stresses in the top fiber and bottom fiber of the bridge due to load combination Service III are shown in Figure 5-15 and Figure 5-16 respectively. The top and bottom fiber stresses due to both load combinations varying with thermal gradient load applied were all within the AASHTO compression limit and tension limit.

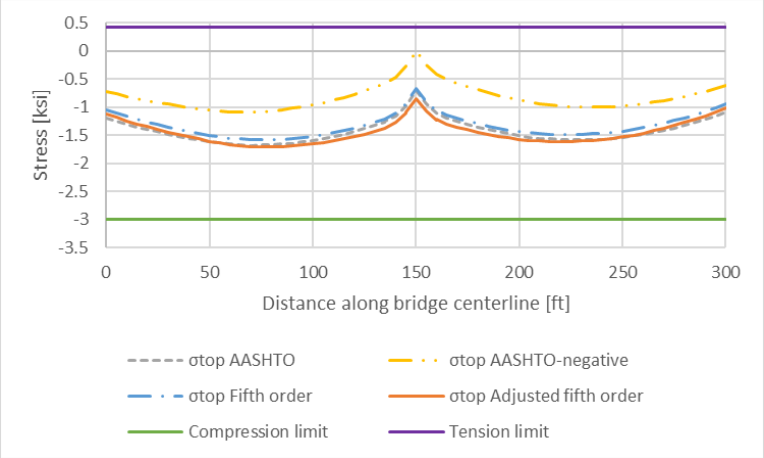

Figure 5-13-Service I stress in top fiber

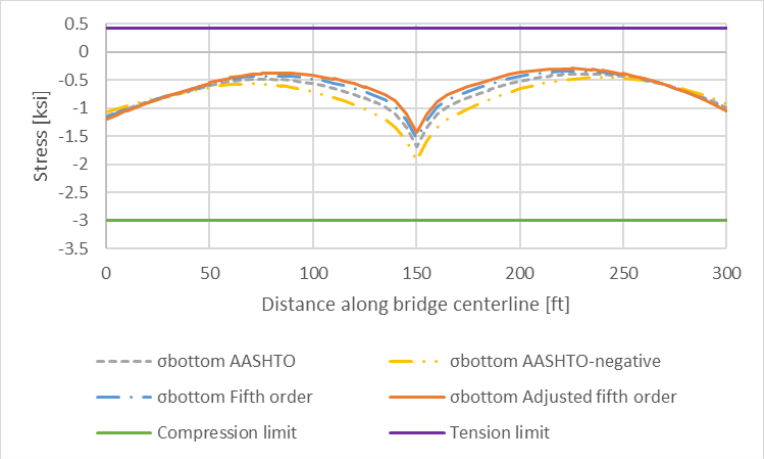

Figure 5-14-Service I stress in bottom fiber

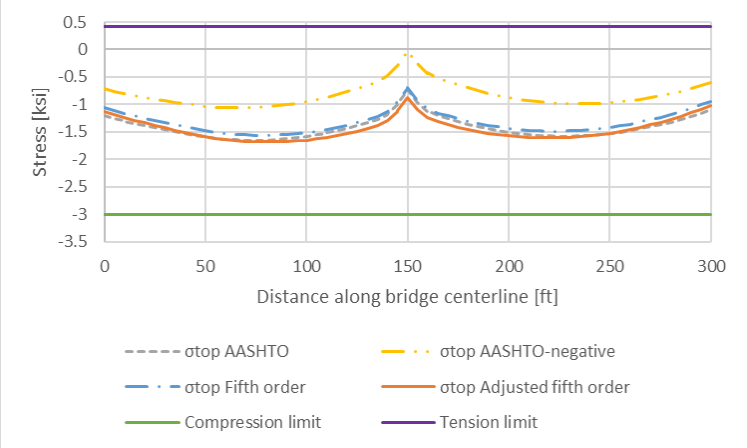

Figure 5-15-Service III stress in top fiber

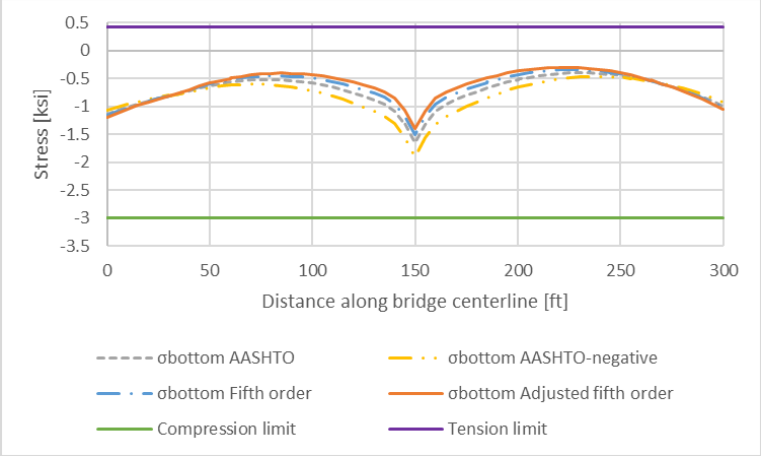

Figure 5-16-Service III stress in bottom fiber

The bearing load limit was calculated using the AASHTO LRFD steel-reinforced elastomeric bearing Method A special design provisions. These provisions govern the average compressive stress due to service load combinations. The maximum compressive stress allowed per bearing pad was 1.25 ksi (8.62MPa). The maximum load allowable for each bearing was 500 kip (2.22MN). The bearing loads caused by the Service I combination are shown in Figure 5-17. The compressive bearing load recommended by AASHTO LRFD, Method A, was exceeded by the load combinations including the positive thermal gradients. Relative to the total loading including the AASHTO positive gradient, the fifth order gradient and adjusted fifth order gradient increased the total load on the exterior bearings by 7% and 12% respectively. It is unlikely that transverse load distribution was analyzed in the design of the Airport Connector, in addition the AASHTO recommended thermal gradient led to lower support reaction than the gradients recommended by previous heat flow analysis of Nevada. The combination of these two

factors led to the conclusions that thermal gradient loads may cause bearing stress limits to be exceeded.

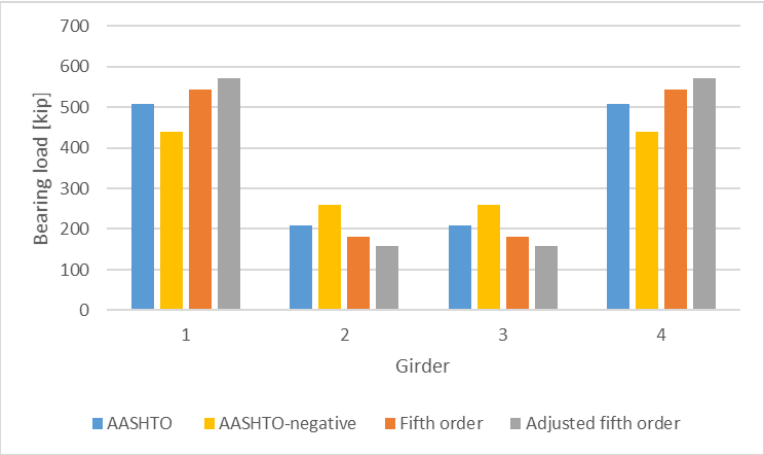

Figure 5-17-Distributed bearing loads with Service I combination at Abutment 1

5.5. Maintenance Records

The maintenance records of the bridge were reviewed to evaluate whether abnormalities related to the bridge bearings could be attributed to thermal loading, drawing potential connection to the analysis results of the previous section. The first inspection of the bridge was completed in 1994. The report noted a few bearing pads were “out of shape”. The bearing pad conditions noted during inspection remained the same until 2002, when the inspection report noted that the bearing pad in the northeast corner of Abutment 2 had an overhang of 1 in. (0.03 m), which led to the inspector lowering the rating of the bearing devices. In 2007, a further complication was noted as two bearings (one interior and one exterior) at Abutment 1 were observed to overhang their pedestals by at least 1 in. (0.03 m). In 2015, the inspection report noted that the bearing at Abutment 2 did not show any additional movement and may have been constructed with overhang.

The movement of the bearings may have been caused by the thermal gradient loading to the bridge or the bearing overhangs may have been present since construction. Thermal gradients would be expected to affect external bearings more than internal bearings. Since no differential wearing was mentioned between the interior and exterior bearing, the current bearing conditions cannot be conclusively attributed to thermal gradients. Uplift that might allow bearings to move off supports was not suggested in the analysis of load combinations. The cause of the bearing issues described in the maintenance records was inconclusive.

5.6. Conclusion

Four thermal gradients were considered when analyzing the concrete box girder bridge carrying the McCarran airport connector in Las Vegas. The typical AASHTO LRFD Zone 1 positive and negative thermal gradients were compared to piecewise linear approximation

of a fifth order thermal gradient and an adjusted fifth order thermal gradient reflecting the worst case thermal loading predicted using heat flow analysis.

The stresses caused by each gradient were evaluated at the top and bottom fiber of the bridge cross section. The total stress caused by each gradient at the pier support were compared. The compressive stress caused in the top fiber did not vary between the AAASHTO positive gradient and the fifth order gradient; but varied when compared to the adjusted fifth order gradient. Significant variation was observed in the tensile stress at the bottom fiber, where the AASHTO positive gradient caused the lowest tensile stress and the adjusted fifth order gradient caused the highest.

The stresses in the bridge caused by AASHTO load combinations Service I and III, including the gradients, were within the AASHTO prestressed concrete stress limits. The effect of altering the thermal gradient load was minimal when analyzing stress due to total combined load. Since CSiBridge is currently unable to calculate primary stresses due to thermal gradients, analytical solutions should be used to incorporate thermal gradient stresses into bridge design.

The support reactions caused by each thermal gradient loading varied significantly from the other gradients. The AASHTO negative gradient caused the smallest support reaction at Abutment 1. The abutment support reactions caused by the fifth order and adjusted fifth order gradients were over 150% and 200% of the AASHTO positive gradient support reaction, respectively. Furthermore, the distribution of support reaction to each bearing due to transverse thermal curvature predicts that positive gradients cause uplift in the interior bearings. However, this uplift was balanced by other loads under the service load combinations such that net uplift was not anticipated. The compression limit was exceeded in the exterior bearing by all three variations of load combination Service I including positive thermal gradients. Additionally, the fifth order gradient and adjusted fifth order gradient increased the total load on the exterior bearings by 7% and 12%, respectively when compared to the total load including the AASHTO thermal gradient. It is recommended that thermal gradient loading be considered using three dimensional models to calculate interior and exterior bearing load distribution.

The AASHTO recommended positive thermal gradient was found to predict stresses and bearing loads that were unconservative relative to the thermal gradients obtained from heat flow analysis. The effect of thermal gradient variation on the stress distribution of the bridge was small but caused significant variation to the abutment bearing loads. Further investigation to fine tune and validate the thermal gradients of the southwestern United States is recommended to determine the adequacy of the current code provisions regarding design considerations for thermal gradients. Parametric studies to establish the expected distribution between interior and exterior bearings could be used as an alternative to three-dimensional bridge model analysis.

6. THERMAL ANALYSIS OF I-580 OVER SOUTH VIRGINIA INTERCHANGE

6.1. Introduction

As mentioned previously, a second bridge was selected for examining the effect of thermal gradients on bridge bearings. The selected bridge is a two-span, skewed, steel girder bridge, which was subjected to different temperature profiles and additional response considerations due to the composite effects. Similar to the Airport Connector, this bridge was selected in light of maintenance records indicating bearing pad issues that might be related to thermal gradient loading. A model of the bridge was built in CSiBridge per the original as-built drawings.

The support reactions caused by thermal gradient loading were expected to be similar to those calculated for the Airport Connector. The skew of the composite bridge caused variation from transverse distribution of bearing loads observed in the Airport Connector analysis.

The bridge was analyzed under the following range of thermal gradients that might occur in a composite bridge in the southwest: the AASHTO Zone 1 positive and negative gradients for steel girder structures, the AUSTROADS steel girder gradient, and the profile with maximum temperature difference calculated by the heat flow analysis of this research (Figure 3-24 and 3-25). Similar to the Airport Connector bridge, the bearing loads due to thermal loading and load combination Service I were compared to AASHTO LRFD design limits to evaluate the influence using different thermal conditions.

6.2. Bridge Characteristics

A composite bridge located in Reno, Nevada (built in 1985) carries Interstate 580 over South Virginia Street, hereafter referred to as "I-580". The two-span 248-foot-long (75.59 m) bridge (Figure 6-1) is slightly curved with a radius of 2500 ft (762 m). The bridge is composed of a 9.5-inch-thick (0.24 m) concrete slab supported on 10 steel plate girders. Expansion bearings plates are located at the south abutment (referred to as "Abutment 1"), sliding bearing plates are located at the pier and fixed bearing plates at the north abutment (referred to as "Abutment 2"). The bridge was selected due to the bearing issues indicated by maintenance records that might have been caused by thermal gradients. Several of the fixed bearings at the north abutment exhibit partial uplift.

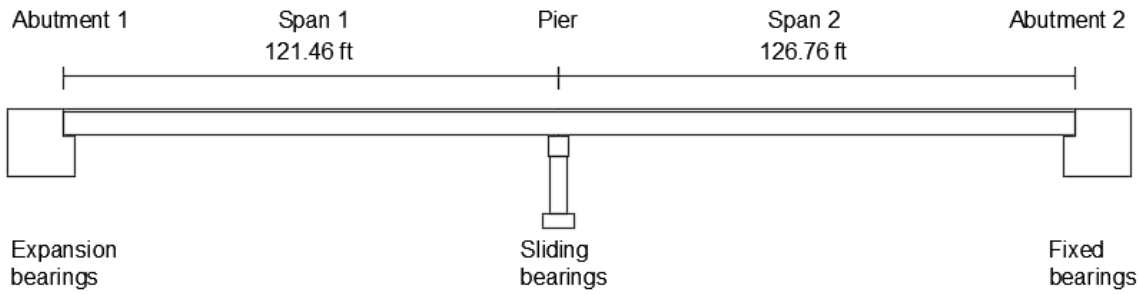

Figure 6-1-Side elevation of I-580 composite bridge

The superstructure cross section is symmetrical about the centerline (Figure 6-2). Each half is composed of five girders on a concrete bent, where the bent is supported by two columns flared at the top in the transverse direction. There are three concrete railings on top of the deck; one at each edge and one on the centerline of the cross section. The skew on each support decreases from Abutment 1 (42°10') to the pier (39°22') to Abutment 2 (36° 28'). Cross frames built perpendicular to the girder provide transverse bracing as shown in the layout of the bridge in Figure 6-3.

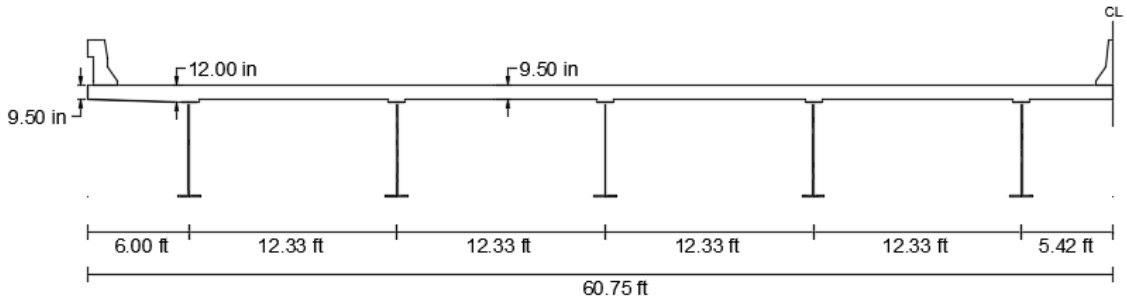

Figure 6-2-Half cross section of I-580 composite bridge

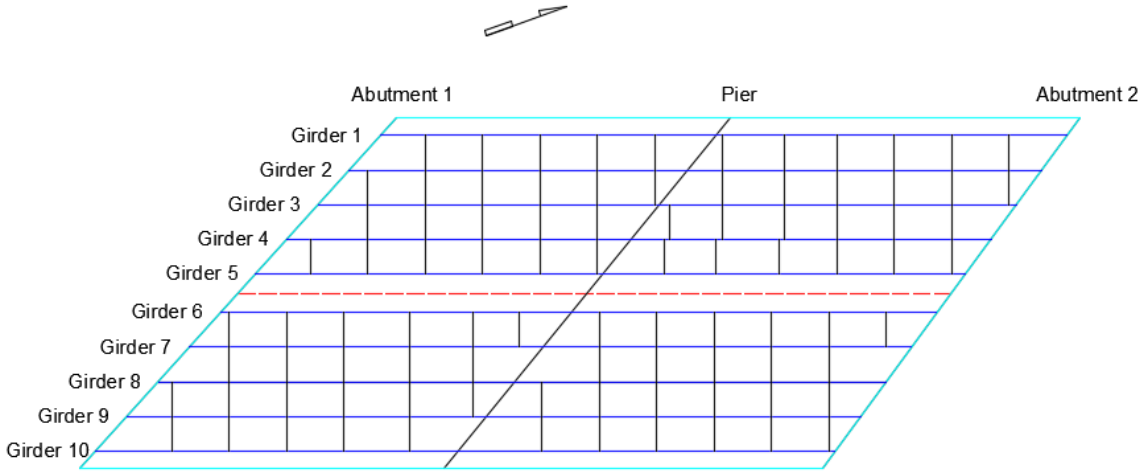

Figure 6-3-Plan of I-580 composite bridge

The bridge width is 121.5 ft (37.03 m) from outer deck edges, where the total lane width is 72 ft (21.95 m). The typical concrete haunch thickness is 2.5 in. (0.635 m) from the bottom of the top flange to the bottom of the deck. The overhang distance from the centerline of the exterior girder is 6 ft (1.83 m). The distances between the column centerlines are 41.0625 ft (12.52 m) and 41.7343 (12.72 m) under Girder 1 through 5 and Girder 6 through 10 respectively. In each span, all the girders are composed of six built-up steel sections that vary nonprismatically from the abutment to the pier. The dimensions of the six girder cross sections and the length of each segment in both spans are shown in Table 6-1. The skew of the bridge requires girders of varying length; the variation takes place in the length of the first cross section which varies per girder.

Table 6-1-Girder Cross Section Dimensions

Top Flange Width [in]	Top Flange Thickness [in]	Bottom Flange Width [in]	Bottom Flange Thickness [in]	Web Height [in]	Web Thickness [in]	Span 1 Length [ft]	Span 2 Length [ft]
10	0.625	16	1	66	0.6875	24-27	24-26
14	1	20	1.5	66	0.6875	14	16
14	1	20	1.5	66	0.625	48	48
20	1.0625	20	1.0625	66	0.75	14	16
24	1.25	24	1.25	66	0.75	14	16
24	1.75	24	1.75	66	0.75	8	8

The concrete has an ultimate compressive strength of 4000 psi (27.58 MPa). The reinforcing steel is ASTM A615 Grade 60. The structural steel is ASTM A36 (AASHTO M 183). The bearings on the bridge are steel-reinforced elastomeric bearings with a hardness of 50 Durometers composed of 0.5 in. (12.7 mm) thick laminations. The expansion bearings at Abutment 1 are 26 in. (0.66 m) wide by 20 in. (0.51 m) long with a thickness of 3 in. (0.08 m). The sliding bearings at the pier are 34 in. (0.86 m) wide by 26

in. (0.66 m) long with a thickness of 2 in. (0.05 m). The fixed bearings at the pier are skewed with orthogonal dimensions of 28 in. (0.71 m) by 30 in. (0.76 m) long with a thickness of 1 in. (0.03 m).

The bridge was widened in 2012 with the addition of two girders, a bent cap, a column and footing to the eastern edge of the bridge, which added 15 ft (4.57 m) of deck width. As this addition occurred within the last five years, it was neglected from consideration.

6.3. Modeling Assumptions and Verification

The central angle of a single span of the bridge is 2.78°. Following the same AASHTO guidelines as applied to the Airport Connector, the CSiBridge model of I-580 did not include the curvature of the bridge.

The CSiBridge model was utilized for determining the load transferred to the bearings under dead load, live load and thermal gradient loading. Similar to the Airport Connector, area and spine models were verified by comparing the peak bending moments and support reactions of each model resulting from the AASHTO LRFD Zone 1 positive composite thermal gradient to the composite section exact solution (Appendix E). The analytically calculated solutions did not account for any effects of the skew or the changing girder dimensions. The girder section that comprised the largest portion of the bridge length was used in the analytically calculated solutions.

The area and spine models of I-580 were generated using the same maximum segment length and submesh size as Airport Connect. However, unlike Airport Connector, the area model only used shell elements for the deck section; girders and cross frames were modeled with frame elements. In both models the base of the four columns were pinned. The bearing supports at the first abutment and the pier restrained movement in the vertical and transverse directions, while the bearing supports at the second abutment also restrained moment in the longitudinal direction. The results of the CSiBridge analysis with AASHTO LRFD Zone 1 composite thermal gradient loading and the analytically calculated solution from Appendix E are shown in Table 6-2.

Table 6-2-Peak bending moment and support reactions due to AASHTO thermal gradient

Model	Moment [k-ft]	Abutment 1 Force [k]	Pier Force [k]	Abutment 2 Force [k]
Analytical	5544.7	45.65	89.39	43.74
Spine	7163.35	58.97	115.71	56.74
Area	6805.37	56.10	110.70	54.60

The discrepancy between bending moment results of CSiBridge relative to the analytical solutions of the AASHTO LRFD Zone 1 composite thermal gradient exceeded 25% for the spine model and slightly less for the area model. This high level of discrepancy was attributed to the nonprismatic section properties and skew in the CSiBridge models that was not accounted for in the analytically calculated solutions. As done previously in analysis of the Airport Connector, the area model was used for evaluating forces present in bearings due to the spine model inability to solve for transverse distribution of bearing load.

6.4. Analysis

To evaluate the effect of the thermal gradient shape on a composite member, five gradients were compared. The gradients of interest, shown in Figure 6-4, were the current AASHTO LRFD Zone 1 positive gradient (referred to as "AASHTO"), AASHTO LRFD Zone 1 negative gradient (referred to as "AASHTO-negative"), the AUSTROADS composite gradient with the same maximum temperature as the AASHTO gradient (referred to as "AUSTROADS") and two variations of the composite results found in the heat flow analysis. The two gradients taken from the heat flow analysis included: a temperature profile with the calculated temperatures (referred to as "Heat flow-unaltered") and a profile with the temperature through the girder set to zero (referred to as "Heat flow-zero") leaving only linear variation in temperature through the deck. As mentioned in Chapter 4, a limitation of using CSiBridge was that the fifth order portion of the AUSTROADS gradients was simplified to four linear segments. Since CSiBridge does not have the capability to check for the stress distribution of a composite section, stress analysis was not performed.

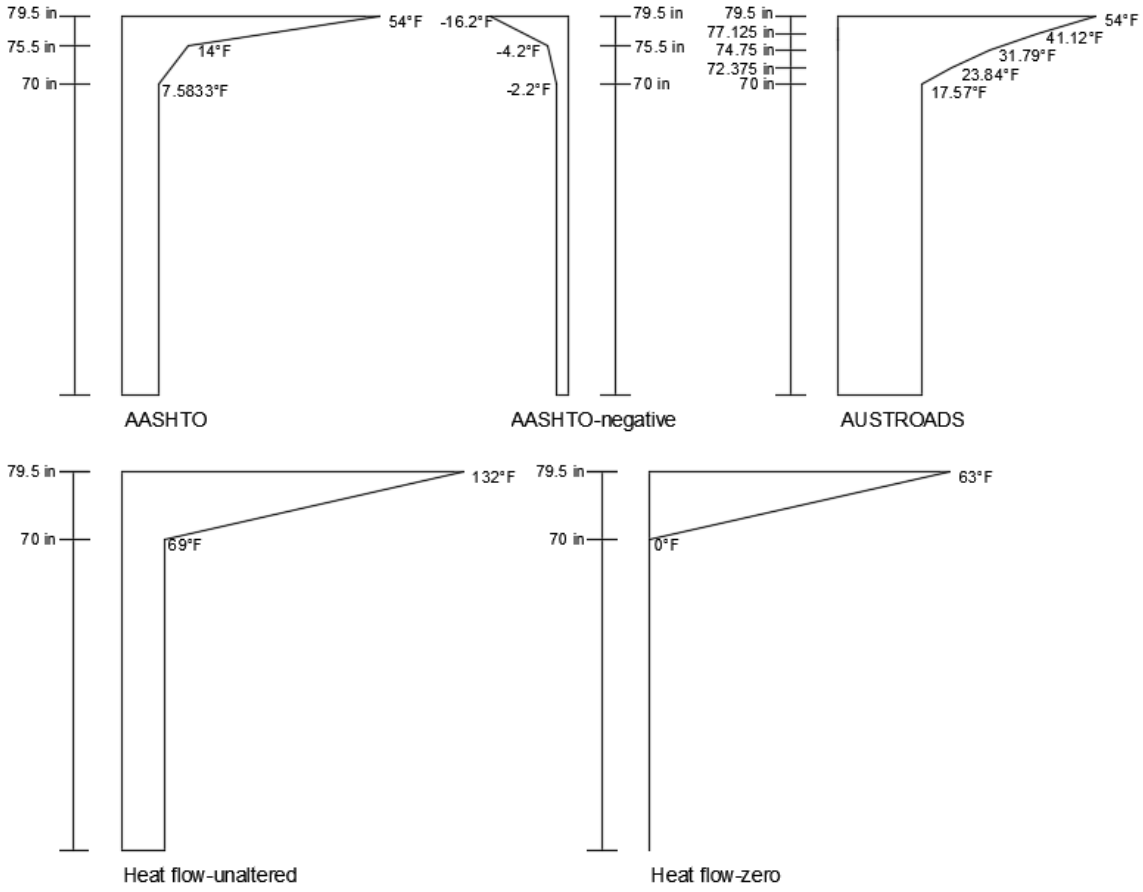

Figure 6-4-Thermal gradients applied to the I-580 bridge

Figures 6-5 presents the CSiBridge area model moment at the pier. Figures 6-6 through 6-8 present the CSiBridge area model support reactions at Abutment 1, the pier, and Abutment 2, respectively. The peak bending moment and support reactions caused by the heat flow-zero gradient were more than 200% of the peak bending moment and support reactions caused AASHTO gradients while those due to heat flow-unaltered were 133% of the reactions due to AASHTO gradients. The bending moment and support reaction due to the AASHTO Zone 1 composite thermal gradient.

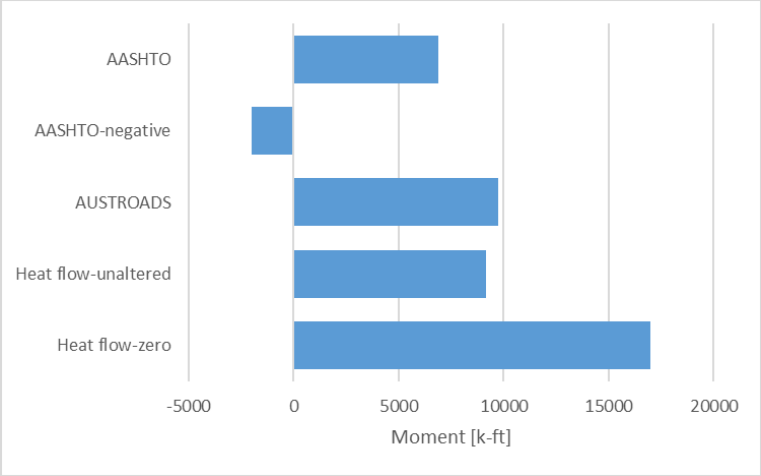

Figure 6-5-Moment at pier due to thermal gradients

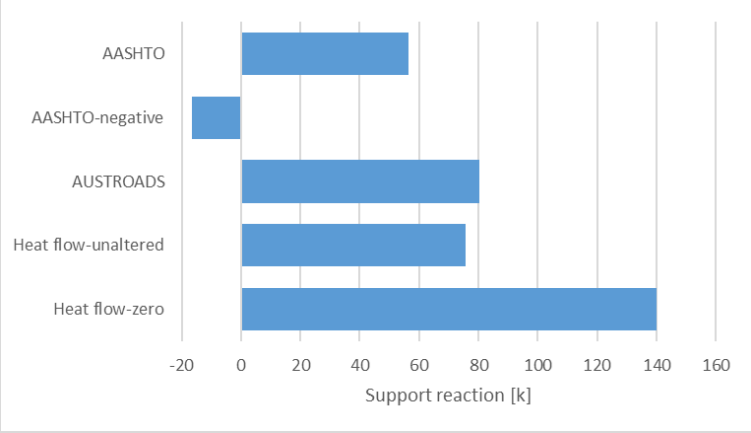

Figure 6-6-Support reaction at Abutment 1 due to thermal gradients (uplift is negative)

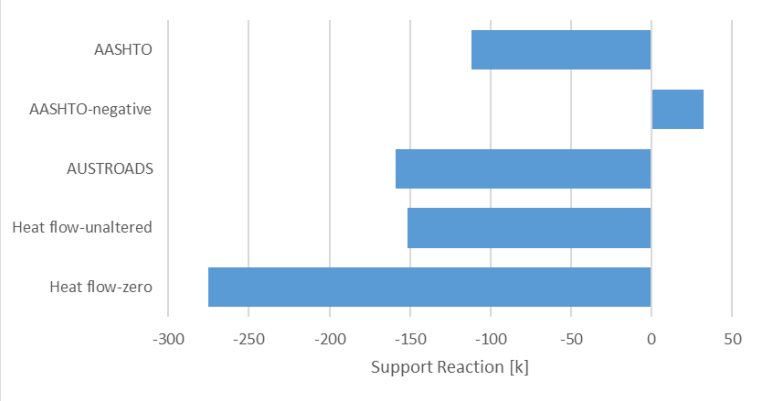

Figure 6-7-Support reaction at the pier due to thermal gradients (uplift is negative)

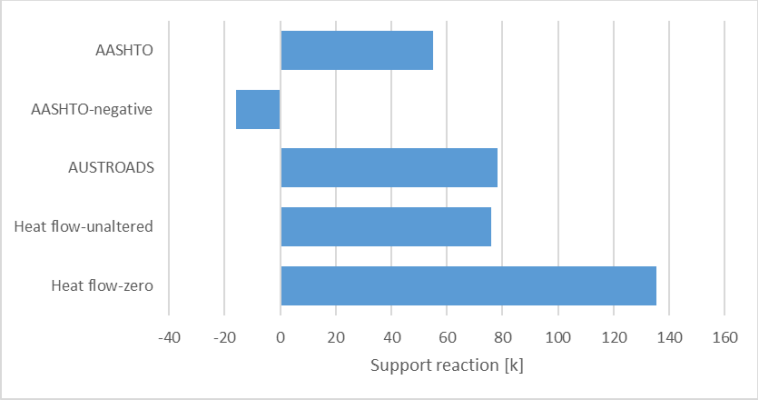

Figure 6-8-Support reaction at Abutment 2 due to thermal gradients (uplift is negative)

The significant difference between the heat flow-unaltered and the heat flow-zero gradients was contrary to the principle of thermal gradient loading in concrete sections. Altering the thermal gradient by a constant temperature in a uniform material section would not affect thermal curvature, bending moments and support reactions. However, in a composite structure built of two materials with unequal thermal coefficients, heating relative to the original temperature at time of construction would cause unequal expansion of the concrete and steel. The thermal coefficient of concrete is less than steel, thus the expansion of steel is greater than concrete under equal temperature change (Figure 6-9). If the concrete and steel sections are connected and are both subjected to a uniform temperature change, a restraining force would be generated at the interface between materials (Figure 6-10). On the other hand, a thermal gradient through the concrete portion of a composite section would cause forces that restrain axial expansion and moments that restrain the curvature (Figure 6-11). Any increase in temperature in the steel would cause expansion in steel that reduces the interface force but does not affect the moment. Thus, reduction in the forces at the interface caused by uniform heating of the steel may lower the moment in composite

sections and therefore reduce the impact of the thermal gradient. The smaller peak moment of the heat flow-unaltered gradient compared to the heat flow-zero was a result of the increased temperature change in the girder.

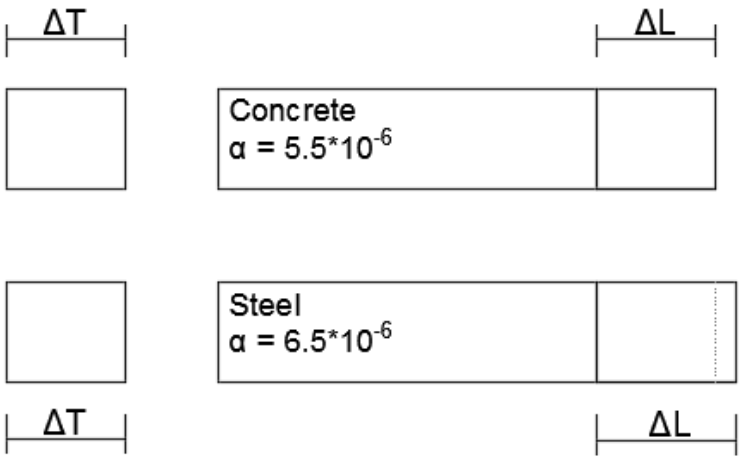

Figure 6-9-Expansion of concrete and steel under uniform temperature change

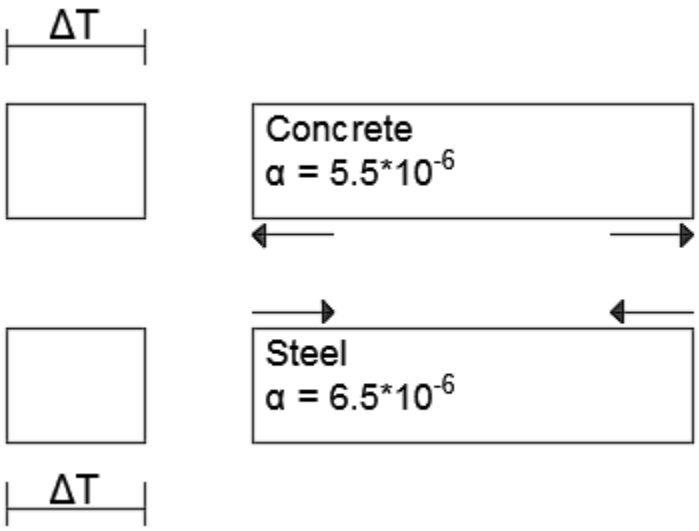

Figure 6-10-Expansion of concrete and steel under uniform temperature change with edge restrained

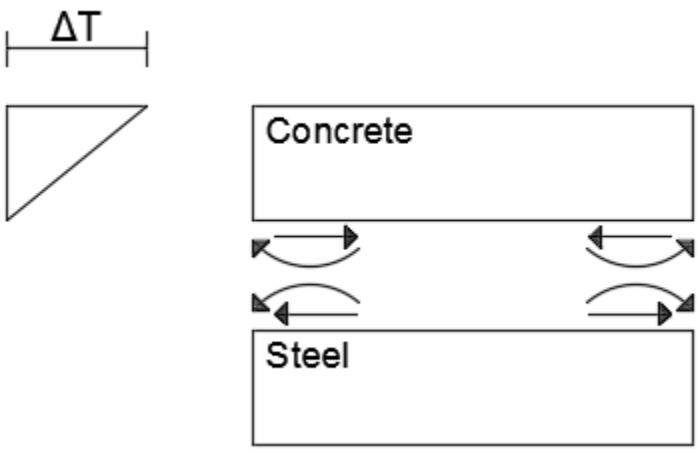

Figure 6-11-Expansion of concrete under thermal gradient with edge restrained

The loading of each of the 10 bearings at Abutment 1, the pier and Abutment 2 due to applied thermal gradients are shown in Figures 6-12 through 6-14. The loads were distributed such that the exterior bearings experience increased loading while the interior bearings experienced uplift, except for the AASHTO negative gradient which led to the opposite trend. The skew of the I-580 affected the distribution of load to exterior bearings; Abutment 1 experienced the largest bearing load at the obtuse corner (Girder 1). Abutment 2 had the opposite trend of exterior bearing loading that was caused by the longitudinal restraint applied at each bearing. Unlike the overall support reactions, the transverse distribution of bearing loads that caused the largest loading to exterior bearings by a significant margin was due to the heat flow-unaltered gradient. The loading on the girder 10 bearing caused by heat flow-unaltered gradient was 400% of the loading due to the AASHTO positive composite gradient, while heat flow-unaltered gradient caused 168% of the loading due to the AASHTO positive composite gradient. The large transverse distribution of load was attributed to the restraint condition of the bearings. Transverse movement of the bearings was restrained at Abutment 1 and the pier, which increased the transverse curvature and thus increased the loading of the exterior bearings (especially the obtuse corner of Abutment 1, Girder 1). The longitudinal restraint of bearings at Abutment 2 in addition to the transverse restraint increased the transverse distribution and caused the acute corner bearing (Girder 1) load to be higher than the obtuse corner bearing (Girder 10) load. Heat flow-unaltered had the largest increase in temperature and thus the largest transverse distribution of load.

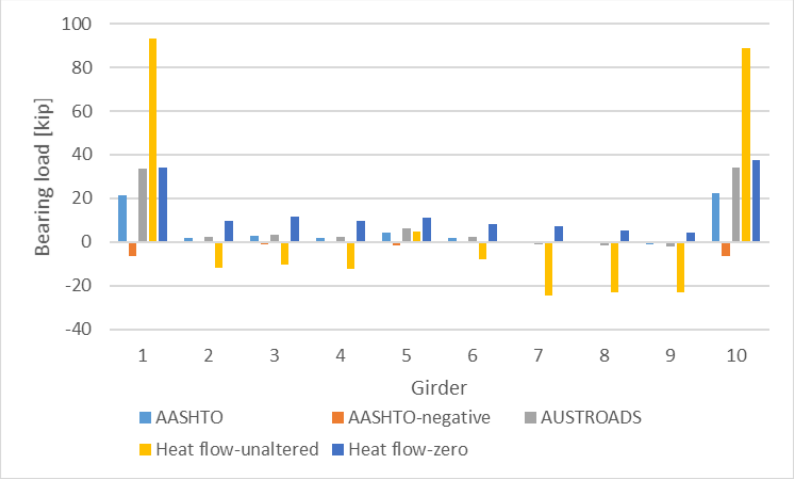

Figure 6-12-Distributed bearing loads at Abutment 1 due to thermal gradient (uplift is negative)

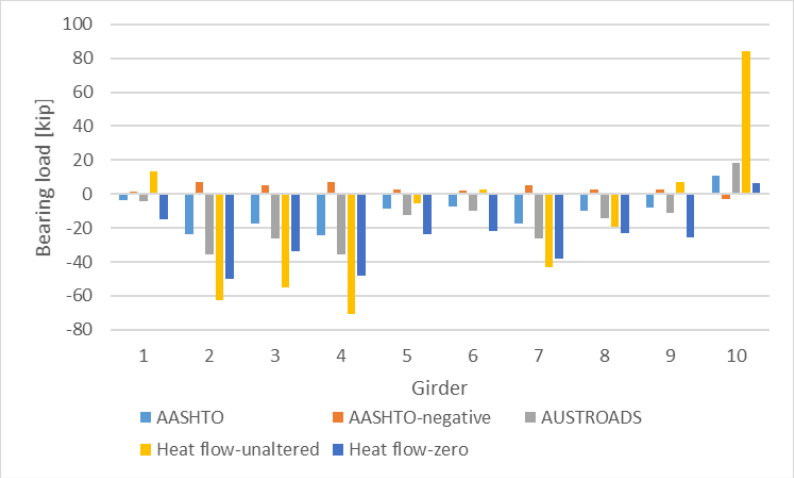

Figure 6-13-Distributed bearing loads at pier due to thermal gradient (uplift is negative)

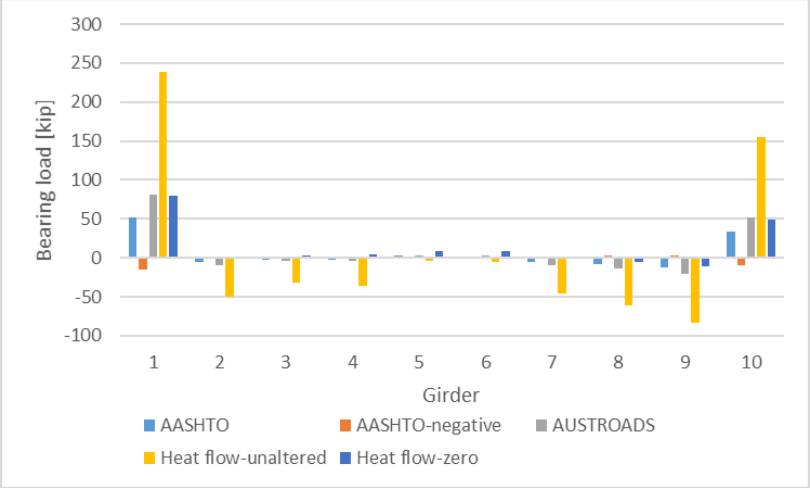

Figure 6-14-Distributed bearing loads at Abutment 2 due to thermal gradient (uplift is negative)

For bearing load analysis, AASHTO LRFD load combination Service I (Eq. 5-1) was applied, where the PS = 0. Load combination Service III was not applied to the I-580 bridge as it was only required for "longitudinal analysis relating to tension in prestressed concrete superstructures" (AASHTO, 2010).

The bearing load limit was calculated using the AASHTO LRFD steel-reinforced elastomeric bearing Method A special design provisions. These provisions govern the average compressive stress due to service load combinations. The varying bearing sizes result in maximum compressive stresses at Abutment 1, the pier, and Abutment 2 of 0.89 ksi, 1.20 ksi and 1.25 ksi (6.14 MPa, 8.27 MPa, and 8.62 MPa) respectively. The maximum loads allowable for each bearing at Abutment 1, the pier and Abutment 2 were 463 kip, 1061 kip and 1050 kip (2.06MN, 4.72 MN and 4.67 MN), respectively. The bearing loads caused by the Service I combination are shown in Figures 6-15 through 6-17. The compressive bearing load recommended by AASHTO LRFD Method A was not exceeded by the load combinations at the abutments or pier supports. However, the load on the exterior bearing due to a load combination that included the heat flow-unaltered thermal gradient loading exceeded the next largest exterior bearing load by 50 kips at Abutment 1, girder 10 and by 100 kips at Abutment 2, girder 10. The total load increased by 27%, 15% and 39% in exterior bearings of Abutment 1, pier and Abutment 2 respectively, when replacing the current AASHTO gradient with the heat flow-unaltered, which is representative of temperature that might be observed in a field study.

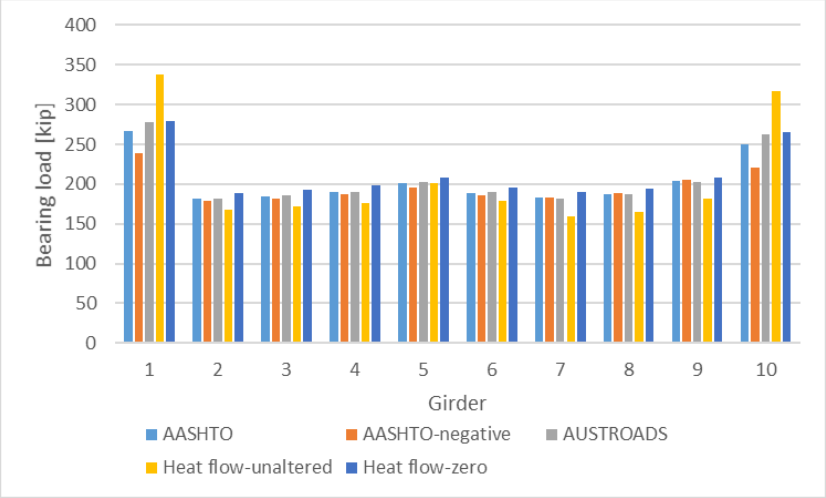

Figure 6-15-Distributed bearing loads with Service I combination at Abutment 1

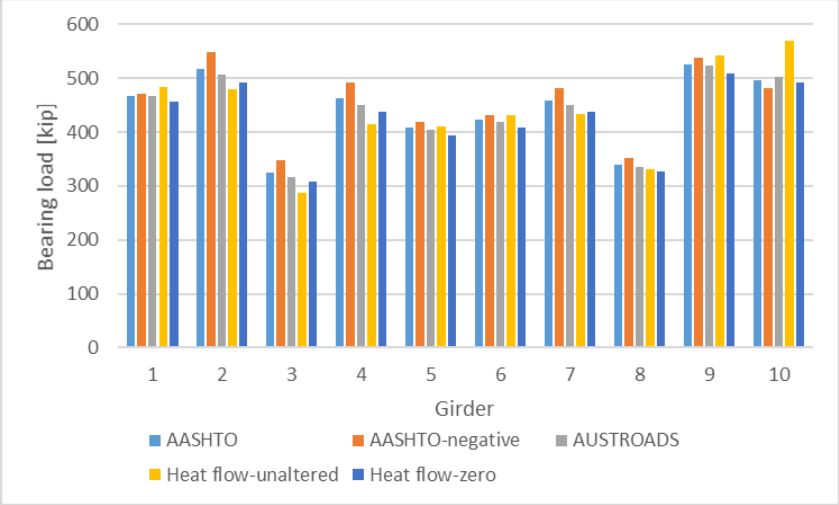

Figure 6-16-Distributed bearing loads with Service I combination at the pier

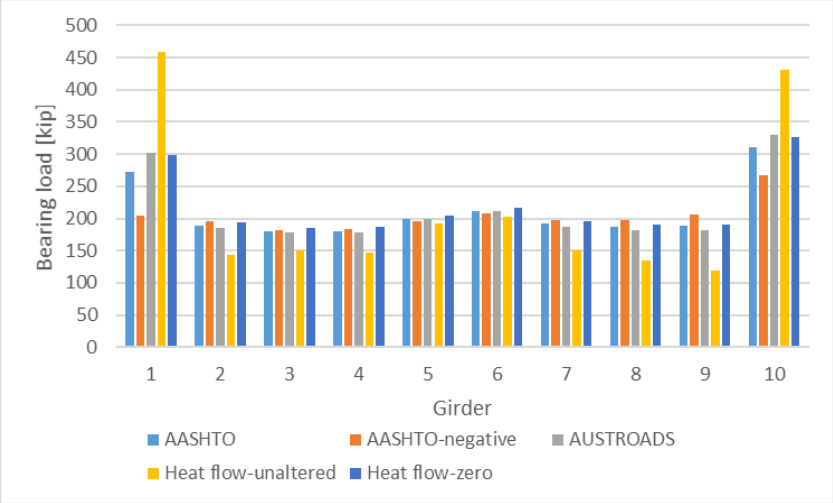

Figure 6-17-Distributed bearing loads with Service I combination at Abutment 2

6.5. Maintenance Records

As previously done with the Airport Connector, the maintenance records of the I-580 bridge were reviewed to evaluate whether abnormalities related to the bridge bearings could be attributed to thermal loading through connection with the analysis results of the previous section. The first inspection report in 1988 did not mention any issues with the bearings. Bearing devices were noted to drop in quality in 1996 with reduced contact between bearing and substructure, hereafter referred to as partial uplift. In 1998, the bearings on the northern end of the girder 1 and 2 were noted to "exhibit only 50% bearing". In 2000, more bearings were observed to exhibit partial uplift and the condition of the bearing devices was listed as critical. In 2002, partial uplift was noted in seven bearings at Abutment 2 as well as finding that abutment and pier anchor bolts were loose.

During a field visit to the I-580 bridge in February, all but three bearings at Abutment 2 (bearings 5, 9 and 10) displayed partial uplift. An example of the partial uplift observed during the field visit is shown in Figure 6-18. Two hypotheses were considered: (1) partial uplift in bearings at Abutment 2 was caused by the thermal gradient loading, or (2) the partial uplift was present since construction. If the partial uplift was due to positive thermal gradients, increased uplift during the summer would be expected; however, partial uplift was present during both winter (field visit) and summer (maintenance records). Furthermore, uplift was not predicted for any bearings at Abutment 2 under load combination Service I; thermal gradients would cause maximum force in the exterior bearings which was not reflected in the observed partial uplift of bearing 1. As the uplift was not reflected in the analysis, uplift was more likely caused by construction than by the thermal gradient.

Figure 6-18: Bearing 7 of Abutment 2 partial uplift from substructure

6.6. Conclusion

Five thermal gradients were considered when analyzing the composite steel girder bridge carrying Interstate 580 over South Virginia Street in Reno. The two AASHTO recommended composite gradients were compared to the AUSTROAD composite gradient and two thermal gradients reflecting the worst case thermal loading predicted from the heat flow analysis. The thermal gradients taken from the heat flow analysis exhibited the extreme assumptions of temperature through the girder: maximum temperature as predicted from heat flow analysis (heat flow-unaltered) and temperature set to zero (heat flow-zero).

The abutment support reaction caused by thermal gradient loading indicated that the most conservative thermal gradient is a linear temperature change through the concrete deck and no temperature change through the girder (i.e. the temperature in the steel girder is the temperature at time of construction). The support reactions due to the heat flow-zero gradient were 200% of the support reaction caused by the AASHTO composite thermal gradient. However, the trends for the transverse distribution of bearing load were opposite the trends of support reaction analysis. The heat flow-unaltered gradient caused the largest transverse distribution of bearing load while the heat flow-zero gradient caused the largest peak bending moments and support reactions. The transverse distribution of load caused by the heat flow-unaltered thermal gradient led to Abutment 1, girder 10 bearing loads that were 200% of the loads due to the heat flow thermal gradient with girder temperature set to zero and 400% of the loads due to the AASHTO composite thermal gradient.

The results of analyzing the I-580 bridge with the code recommended thermal gradient and thermal gradient more reflective of the results of heat flow analysis indicated that the method of solving for thermal gradient loading in a composite bridge has not been

adequately resolved. A more complete method of solving for the effects of thermal gradients should include an estimate of the temperature at time of construction for the composite bridge. A parametric study of three dimensional models is required to determine how variation of thermal gradient and bridge skew effect bearing loads in composite bridges. The contrast in loading between thermal gradient with girder temperature set to zero and an unaltered temperature profile indicate more consideration into the design thermal gradient for composite steel girder bridges with consideration for the conservative transverse distribution of bearing load is required.

7. CONCLUSION

Early investigation of thermal gradients in concrete bridges that led to the development of design thermal gradients for determining thermal curvature and resulting stresses were based on limited meteorological data. Furthermore, verification studies of the AASHTO LRFD thermal gradients conducted in various parts of the United States excluded the southwestern desert States.

In this study, heat flow equations were solved using meteorological data collected from two sites in Nevada to establish a more complete understanding of the variation of bridge temperature through the depth of the bridge over summer months. Two bridges with maintenance records documenting bearing pad issues that may have been the result of thermal loading were analyzed for thermal gradient effects.

7.1. Heat Flow

Heat flow analyses for both prestressed concrete and composite bridge superstructures located in Nevada were performed over a period of four months, May through August of 2015. The meteorological data used had more frequent intervals of data collection and was used for longer periods of analysis than previous studies, which allowed for greater precision in time of day and temperature difference of maximum thermal gradient. For a concrete superstructure, the analysis led to a maximum thermal gradient with a larger temperature difference through the depth than recommended by AASHTO LRFD Zone 1 gradient and a shape more reminiscent of the Priestley fifth order gradient. The AASHTO LRFD thermal gradient was unconservative when compared to the depth and temperature difference of the maximum gradient from the heat flow analysis.

Heat flow analysis of a composite bridge section led to a resulting maximum thermal gradient that was linear through the concrete slab and constant through the depth of the girder. Two variations of the composite maximum temperature profile were selected for later analysis; in the first, the uniform temperature through the girder was as calculated, while in the second the entire profile was adjusted such that the temperature through the girder was set to 0°F. The temperature difference through the slab was larger than recommended by the AASHTO LRFD Zone 1 composite gradient.

7.2. Airport Connector over Wright Brothers Lane

The Airport Connector bridge, a posttensioned box girder in Las Vegas, Nevada was analyzed for three positive thermal gradients: AASHTO, fifth order and adjusted fifth order. The AASHTO recommended thermal gradient consisted of two linear segments through 16 in. (0.41 m) of depth. The fifth order gradient and the adjusted fifth order gradient consisted of fifth order curves through 47.24 in. (1.2 m) of depth. The temperature differences of the AASHTO, fifth order and adjusted fifth order were 54°F, 54°F and 72°F (30°C, 30°C and 40°C) respectively.

Spine and area models created in CSiBridge were compared to an analytical solution for reference. The spine model had better agreement (5% error) to the analytical solutions than the area model (10% error); however, the spine model could not predict transverse

distribution of load. Thus, the area model was used for analysis of loading due to thermal gradients.

The total stress distributions through the depth of the superstructure, due to the three positive thermal gradient, had similar compressive stress in the top fiber but different tensile stresses in the bottom fiber. The shape of the gradient as well as the temperature difference impacted the tensile stresses in the bottom fiber of the bridge superstructure. Compared to a fifth order gradient and the adjusted fifth order gradient, the AASHTO LRFD Zone 1 thermal gradient—representative of current code—was unconservative.

The moments and support reactions due to the AASHTO LRFD Zone 1 thermal gradient were compared to the fifth order gradient and the adjusted fifth order gradient. The support reactions caused by the fifth order and adjusted fifth order gradients were 150% and 200% of the AASHTO positive gradient, respectively. The AASHTO LRFD Zone 1 bending moments and support reactions were unconservative compared to the adjusted thermal gradient, which is based on the heat flow analysis of Nevada.

At no point along the length of the bridge did the stress caused by Service I and Service III load combinations exceed the AASHTO LRFD compression and tension limits of a prestressed concrete bridge section. The effect of altering the thermal gradient load was minimal when analyzing stress due to total combined load. Currently CSiBridge does not accurately calculate stresses due to the thermal gradient loading; bridge designers should use analytical solutions when solving for thermal gradient stresses.

The total load on the bearings caused by load combination Service I was unequally distributed to the exterior and interior bearing pads in the area model which can capture transverse thermal curvature. The load combinations including positive thermal gradients exceeded the design compression limit of the exterior bearings. The fifth order gradient and adjusted fifth order gradient increased the total load on the exterior bearings by 7% and 12%, respectively when compared to the total load including the AASHTO thermal gradient. The bearing pads that are designed without consideration of the influence of transverse thermal loading on individual bearings may be subjected to larger load than expected throughout the summer months. Due to the demonstrated increase in exterior bearing load, thermal gradient loading should be included in three dimensional models to estimate the bridge design bearing loads.

Despite the analysis results indicating that the thermal gradients may have caused the load on exterior bearings to exceed the compressive limit, the maintenance records indicating overhang in three bearings were not sufficient to conclude that the issues present were caused by thermal gradients.

7.3. I-580 over South Virginia Interchange

The I-580 bridge, skewed composite steel girder bridge in Reno, Nevada was analyzed for four positive thermal gradients: AASHTO, AUSTROADS and two variations of the heat flow profile (heat flow-unaltered and heat flow-zero). The AASHTO recommended thermal gradient consisted of two linear segments through the 9.5 in. (0.24 m) of concrete deck and a uniform temperature of 7.58°F (4.21°C) through the girder. The AUSTROAD

gradient consisted of a fifth order curve through the concrete deck and a uniform temperature of 17.57°F (9.76°C) through the girder. The two heat flow profiles have linear change through the depth, heat flow-unaltered and heat flow-zero had uniform temperatures of 69°F and 0°F (38.33°C and 0°C) respectively. The temperature differences of the AASHTO, AUSTROADS, heat flow-unaltered and heat flow-zero were 46.42°F, 36.43°F, 63°F and 63°F (25.69°C, 20.24°C, 35°C and 35°C) respectively.

Spine and area models created in CSiBridge were compared to an analytical solution for reference. The area model had better agreement to the analytical solutions than the spine model. The large discrepancy between models and analytical solutions was attributed to the nonprismatic section properties and skew in the CSiBridge models that was not accounted for in the analytically calculated solutions. The area model was used for analysis of loading due to thermal gradients.

The four-positive thermal gradients caused bending moments, support reactions and bearing loads. The temperature profile taken directly from heat flow analysis (heat flow-unaltered), and the heat flow analysis temperature profile with girder temperature zeroed (heat flow-zero) caused larger bending moments and support reactions than the AASHTO LRFD Zone 1 thermal gradient for composite bridges. The support reactions due to heat flow-zero loading was 200% of the support reactions caused by AASHTO, while the heat flow-unaltered reaction was 133% of AASHTO. The load on the bearing at Abutment 1 girder 10 due to the heat flow-zero and heat flow-unaltered were 168% and 400% of the load due to the AASHTO composite thermal gradient respectively.

The total load on the bearings caused by load combination Service I was unequally distributed to the exterior and interior bearing pads in the area model which can capture transverse thermal curvature. Skew affected the bearing load distribution, the largest loading occurred at the obtuse corner bearing that did not restrict movement in the longitudinal direction. The load combinations did not exceed the design compression limit of the bearings at either abutment or pier. However, the total load including heat flow-unaltered increased the loading at Abutment 1 exterior bearings 27% relative to total load including the AASHTO thermal gradient.

The inclusion of constant temperature through the steel girder has big influence on response in both longitudinal and transverse loading. Zero temperature through the girder (heat flow-zero) maximized bending moment and support reactions; however, maximum temperature through the girder (heat flow-unaltered) maximized individual bearing loads. Thus, it is unclear whether it is more conservative to include or neglect the temperature through the steel girder.

The partial uplift issue listed in the maintenance records appeared not to vary with season. The loads predicted by thermal gradients did not correspond to partial uplift and was therefore deemed to be due to construction practices rather than thermal gradients.

Despite not finding evidence that the bearings of the I-580 bridge had been damaged by thermal gradients, a lack of information provided by AASHTO LRFD (2010) on analysis procedures for composite bridges indicates that more investigation to the solution of

thermal gradient effect is required. The thermal gradient suggested for the southwestern states may be unconservative and requires a field study for verification.

7.4. Recommendations for Future Studies

With respect to the heat flow analysis a future study measuring the temperature through the depth of the superstructure is recommended to verify that the temperature difference calculated with heat flow is an observable phenomenon in bridges located in the southwestern U.S. For the effect of thermal gradient on indeterminate bridges, parametric studies are recommended to establish a range for the expected distribution of loads between interior and exterior bearings of concrete and composite bridge superstructures.

Experimental investigation of a scaled composite bridge that isolates thermal effects is recommended. The study would involve equipping the bridge with thermocouples and load cells connected to a data logger to record temperature through the depth as well as bearing loads over the course of a year. Analyzing the scaled bridge would advance the understanding of how thermal gradients affect a composite bridge without live load considerations obscuring results. The study could be linked to verifying heat flow analysis in the southwestern United States if meteorological conditions at time of study are also recorded.

REFERENCES

AASHTO. (1994). AASHTO LRFD Bridge Design Specifications. In (1st Edition ed.). Washington, D.C. U.S.A.

AASHTO. (2010). AASHTO LRFD Bridge Design Specifications. In (5th Edition ed.). Washington, D.C. U.S.A.

Ala, N., Power, E. H., & Azzizinamini, A. (2016). Predicting the Service Life of Sliding Surfaces in Bridge Bearings. *Journal of Bridge Engineering*, 21(2), 04015035-04015031 -04015035-04015012. doi:10.1061/(ASCE)BE.1943-5592.0000767

AUSTROADS. (1992). Bridge Design Code: Section 2. In. Sydney.

Berwanger, C., & Symko, Y. (1974). Thermal Stresses in Steel-Concrete Composite Bridges. *Canadian Journal of Civil Engineering*, 2(1), 66-84.

Branco, F. A., & Mendes, P. A. (1993). Thermal Actions for Concrete Bridge Design. *Journal of Structural Engineering*, 119(8), 2313-2331. doi:10.1061/(ASCE)0733-9445(1993)119:8(2313)

BS5400-2. (1978). Steel, Concrete and Composite Bridges. In. London, U.K.: British Standard institution.

CSiBridge. (2016). Version 18.1.1 [Computer software]. Computers and Structures, Inc.

Daly, C., Halbleib, M., Smith, J. I., Gibson, W. P., Doggett, M. K., Taylor, G. H., . . . Pasteris, P. P. (2008). Physiographically Sensitive Mapping of Climatological Temperature and Precipitation across the Conterminous United States. *International Journal of Climatology*, 28(15), 2031-2064.

Emanuel, J. H., & Hulsey, J. L. (1978). Temperature Distributions in Composite Bridges. *Journal of the Structural Division*, 104(ST1), 65-78.

Emerson, M. (1973). The Calculation of the Distribution of Temperature in Bridges. *Transport and Road Research Laboratory*, TRRL Report LR 561.

Emerson, M. (1977). Temperature Differences in Bridges: Basis of Design Requirements. *Transport and Road Research Laboratory*, TRRL Laboratory Report 765.

Ghali, A., & Neville, A. M. (1989). Structural Analysis: *A Unified Classical and Matrix Approach* (T. Edition Ed.). London; New York: Chapman and Hall.

Hedegaard, B. D., French, C. E. W., & Shield, C. K. (2013). Investigation of Thermal Gradient Effects in the I-35W St. Anthony Falls Bridge. *Journal of Bridge Engineering*, 18(9), 890-900. doi:10.1061/(ASCE)BE.1943-5592.0000438

Hunt, B., & Cooke, N. (1975). Thermal Calculation for Bridge Design. *Journal of the Structural Division*, 101(ST9), 1763-1782.

Imbsen, R. A., Vandershaf, D. E., Schamber, R. A., & Nutt, R. V. (1985). Thermal Effects in Concrete Bridge Superstructures.*National Cooperative Highway Research Program Report, 276*, 1-99.

Kennedy, J. B., & Soliman, M. H. (1987). Temperature Distribution in Composite Bridges. *Journal of Structural Engineering*, 113(3), 475-482.

Lanigan, A. G. (1973). *The Temperature Response of Concrete Box Girder Bridges*. (Ph.D.), University of Auckland New Zealand,

Lee, J.-H. (2012). Investigation of Extreme Environmental Conditions and Design Thermal Gradients during Construction for Prestressed Concrete Bridge Girders. *Journal of Bridge Engineering*, 17(3), 547-556. doi:10.1061/(ASCE)BE.1943-5592.0000277

Moorty, S., & Roeder, C. W. (1992). Temperature- Dependent Bridge Movements. *Journal of Structural Engineering*, 118(4), 1090-1105. doi:10.1061/(ASCE)0733-9445(1992)118:4(1090)

Naruoka, M. H., & Yamaguti, T. (1957). *The Measurement of the Temperature of the Interior of the Reinforced Concrete Slab of the Shigita Bridge and Presumption of Thermal Stresses.* Paper presented at the Symposium on the Stress Measurements for Bridge and Structure Tokyo, Japan.

Nguyen, H. H., & Tassoulas, J. L. (2010). Directional Effects of Shear Combined with Compression on Bridge Elastomeric Bearings. *Journal of Bridge Engineering*, 15(1), 73-80. doi:10.1061/(ASCE)BE.1943-5592.0000034

NOAA Air Research Laboratories. (2017). Surface Radiation Budget Network (SURFRAD) Data. Retrieved from: ftp://aftp.cmdl.noaa.gov/data/radiation/surfrad/Desert_Rock_NV/

NREL. (2017). National Solar Radiation Database (NSRDB) Data Retrieved from: https://nsrdb.nrel.gov/nsrdb-viewer

Potgieter, I. C., & Gamble, W. L. (1983). *Response of Highway Bridges to Nonlinear Temperature Distributions*. Civil Engineering Studies SRS-505.

Potgieter, I. C., & Gamble, W. L. (1989). Nonlinear Temperature Distributions in Bridges at Different Location in the United States. *PCI Journal*, 34(4), 80-103.

Priestley, M. (1972a). *Thermal Gradients in Bridges-Some Design Considerations*. New Zealand Engineering, 27(7), 228-233.

Priestley, M. (1972b). *Structural Model of a Prestressed Concrete Box Girder Bridge-Phase 2: Thermal Loading*. Vol 1- Model Description and Temperature Results. MWD Central Labs (Report No. 440).

Priestley, M. (1976a). Linear Heat-Flow Analysis of Concrete Bridge Deck. Research Report. Department of Civil Engineering. University of Canterbury, Christchurch, New Zealand.

Priestley, M. (1976b). Design Thermal Gradients for Concrete Bridges. *New Zealand Engineering*, 31(9), 213-219.

Priestley, M., & Buckle, I. (1978). *Ambient Thermal Response of Concrete Bridges*. RRU Bulletin 42, 2, 1-83.

Roberts-Wollman, C. L., Breen, J. E., & Cawrse, J. (2002). Measurements of Thermal Gradients and their Effects on Segmental Concrete Bridge. *Journal of Bridge Engineering*, 7(3), 166-174. doi:10.1061/(ASCE)1084-0702(2002)7:3(166)

Rodriguez, L. E. (2012). *Temperature Effects on Integral Abutment Bridges for The Long-Term Bridge Performance Program*. Utah State University, Logan, Utah.

Rodriguez, L. E., Barr, P. J., & Halling, M. W. (2014). Temperature Effects on a Box-Girder Integral-Abutment Bridge. *Journal of Performance of Constructed Facilities*, 28(3), 583-591. doi:10.1061/(ASCE)CF.1943-5509.0000437

Roeder, C. W. (2003). Proposed Design Method for Thermal Bridge Movements. *Journal of Bridge Engineering*, 8(1), 12-19. doi:10.1061/(ASCE)1084-0702(2003)8:1(12)

Soliman, M., & Kennedy, J. B. (1986). Simplified Method for Estimating Thermal Stresses in Composite Bridges. Structural Design of Bridges, 23-31.

Tindal, T. T., & Yoo, C. H. (2003). Thermal Effects on Skewed Steel Highway Bridges and Bearing Orientation. *Journal of Bridge Engineering*, 8(2), 57-65. doi:10.1061/(ASCE)1084-0702(2003)8:2(57)

Wellock, D. (1994). *Thermal Movements of Two Steel Composite Bridges: A Case Study*. (Master of Science in Civil Engineering), University of Wyoming, Laranie, Wyoming.

Western Regional Climate Center (2017). WRCC data list summary. Retrieved from http://www.wrcc.dri.edu/cgi-bin/wea_list.pl?nvunrc

Zuk, W. (1961). Thermal and Shrinkage stresses in Composite Beams. *Journal of the American Concrete Institute*, 58(3), 327-340.

Zuk, W. (1965). Thermal Behavior of Composite Bridges-Insulated and Uninsulated. *Highway Research Record*, 76, 231-253.

APPENDIX A- PRIESTLEY AND BUCKLE (1978) EXAMPLE 1

The example problem from Priestley and Buckle (1978) was used as verification of CSiBridge's ability to calculate the forces caused by a thermal gradient. It involved the concrete tee beam bridge shown in Figure A-1. The dimension of a single girder plus effective deck width (a quarter of the total deck) and the thermal gradient applied as a five-line simplification of the fifth order gradient are shown in Figure A-2. The span dimensions of the bridge are shown in Figure A-3.

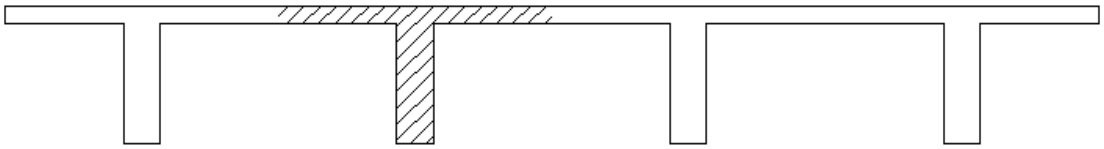

Figure A-1-Bridge cross section

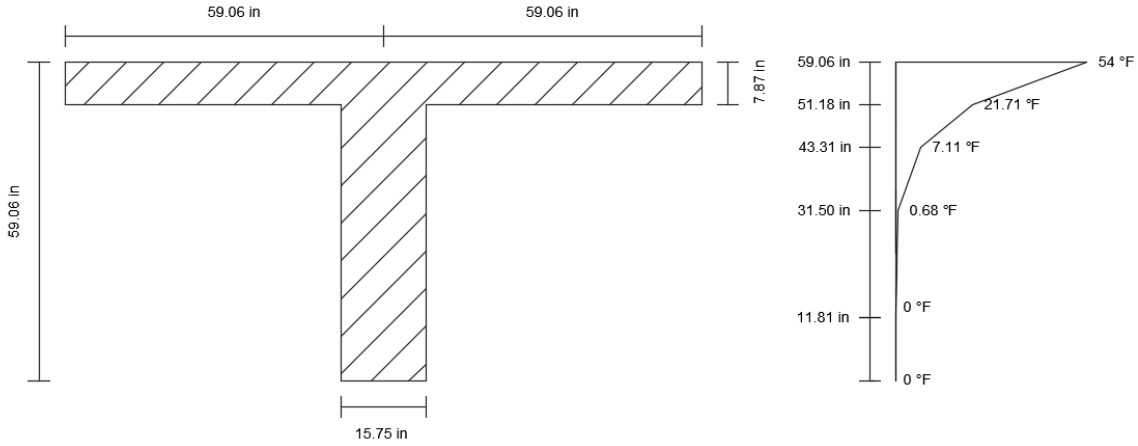

Figure A-2-Single-girder cross section and applied thermal gradient

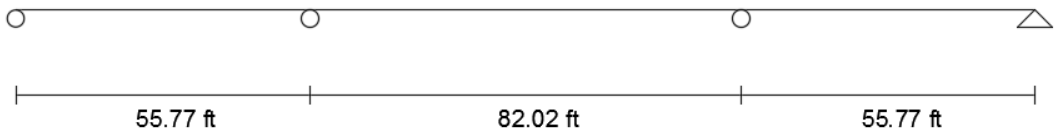

Figure A-3-Bridge span dimensions

The material properties of the concrete used in analysis of the single girder section:

$$\alpha = 5.56 * 10^{-6\circ} F^{-1}$$

$$E = 4{,}351.13\ ksi$$

The cross-section properties of the single girder:

$$I = 557{,}138\ in^4$$

$$A = 1{,}736\ in^2$$

$$n = 41.42\ in$$

Setting the bottom of the bridge as the datum (y equal to zero), the following equations express the thermal gradients of each of the five lines:

$$t_{(y)} = 0°F \text{ For } 0 \le y \le 11.81in$$

$$t_{(y)} = 0.0345y - 0.4079°F \text{ For } 11.81 \le y \le 31.50\ in$$

$$t_{(y)} = 0.5445y - 16.47°F \text{ For } 31.50 \le y \le 43.3\ in$$

$$t_{(y)} = 1.8551y - 73.236°F \text{ For } 43.3 \le y \le 51.18\ in$$

$$t_{(y)} = 4.0977y - 188.01°C \text{ For } 51.18 \le y \le 59.06\ in$$

Solving for the curvature of the bridge without the pier supports (simply supported):

$$\psi = \frac{\alpha}{I}\int t_{(y)} b_{(y)} (y - n)dy$$

$$\psi = \frac{\alpha}{I}\Big[\int_0^{11.81} (0)(15.75)\,(y - 41.42)dy + \int_{11.81}^{31.50} (0.0345y - 0.4079)(15.75)\,(y - 41.42)dy + \int_{31.50}^{43.31} (0.5445y - 16.47)(15.75)\,(y - 41.42)dy + \int_{43.31}^{51.18} (1.8551y - 73.236)(15.75)\,(y - 41.42)dy + \int_{51.18}^{59.06} (4.0977y - 188.01)(118.12)\,(y - 41.42)dy\Big]$$

$$\psi = \frac{5.56 * 10^{-6}}{557{,}138}[0 - 1{,}733.44 - 1{,}733.18 + 11{,}589.9 + 502{,}457]$$

$$\psi = 5.10 * 10^{-6} in^{-1}$$

The curvature of the bridge caused by thermal gradients is resisted in an indeterminate structure. To remove the incompatible rotation at each support, a restraint moment is applied as shown in Figure A-4.

Figure A-4-Moment restraints

The restraint moment (the moment of inertia of the entire cross section of bridge required):

$$M = EI\,\psi$$

$$M = 4{,}351.13\ ksi * (557{,}138\ in^4 * 4) *\ 5.10 * 10^{-6} in^{-1}$$

$$M = 49{,}453.27\ kip - in$$

The actual bending moment in the beam can be found using moment distribution method, for this case the adjusted moment is estimated to be $M' = 1.17M$:

$$M' = 1.17M = 57{,}860.33\ kip - in$$

Reaction forces:

$$V = \frac{dM}{dx} = \frac{M'}{55.77\ ft} = 86.46\ kip$$

The resulting bending moment and reaction forces are shown in Figure A-5 and A-6.

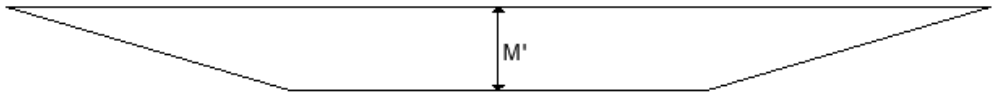

Figure A-5-Bending moment diagram

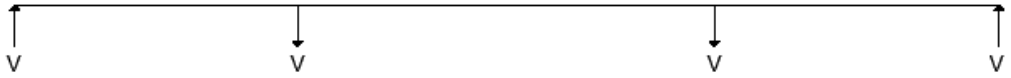

Figure A-6- Support reaction diagram

Solving for the strain in the bridge without the pier supports (simply supported):

$$\varepsilon_0 = \frac{\alpha}{A}\int t_{(y)} b_{(y)}\,dy - \psi n$$

$$\varepsilon_0 = \frac{\alpha}{A}\left[\int_0^{11.81} (0)(15.75)\,dy + \int_{11.81}^{31.50} (0.0345y - 0.4079)(15.75)\,dy + \int_{31.50}^{43.31} (0.5445y - 16.47)(15.75)\,dy + \int_{43.31}^{51.18} (1.8551y - 73.236)(15.75)\,dy + \int_{51.18}^{59.06} (4.0977y - 188.01)(118.12)\,dy\right] - 5.10 * 10^{-6} in^{-1} * 41.42\ in$$

$$\varepsilon_0 = \frac{5.56 * 10^{-6}}{1{,}736}[0 + 105.191 + 724.875 + 1785.93 + 35235.1] - 5.10 * 10^{-6} in^{-1} * 41.42\ in$$

$$\varepsilon_0 = -8.97 * 10^{-5}$$

Primary thermal stress through depth of the cross section (shown in Figure A-7):

$$f_{p_{(y)}} = E(\varepsilon_0 + \psi y - \alpha \cdot t_{(y)})$$

From $0 \leq y \leq 11.81 in$:

$$f_{p_{(y)}} = 4{,}351.13\ ksi(-8.97 * 10^{-5} + 5.10 * 10^{-6} \cdot y - 5.56 * 10^{-6} \cdot 0\ )$$

From $11.81 \leq y \leq 31.50\ in$:

$$f_{p_{(y)}} = 4{,}351.13\ ksi(-8.97 * 10^{-5} + 5.10 * 10^{-6} \cdot y - 5.56 * 10^{-6} \cdot (0.0345y - 0.4079)\ )$$

From $31.50 \leq y \leq 43.31\ in$:

$$f_{p_{(y)}} = 4{,}351.13\ ksi(-8.97 * 10^{-5} + 5.10 * 10^{-6} \cdot y - 5.56 * 10^{-6} \cdot (0.5445y - 16.47)\ )$$

From $43.31 \leq y \leq 51.18\ in$:

$$f_{p_{(y)}} = 4{,}351.13\ ksi(-8.97 * 10^{-5} + 5.10 * 10^{-6} \cdot y - 5.56 * 10^{-6} \cdot (1.8551y - 73.236)\ )$$

From $51.18 \leq y \leq 59.06\ in$:

$$f_{p_{(y)}} = 4{,}351.13\ ksi(-8.97 * 10^{-5} + 5.10 * 10^{-6} \cdot y - 5.56 * 10^{-6} \cdot (4.0977y - 188.01)\ )$$

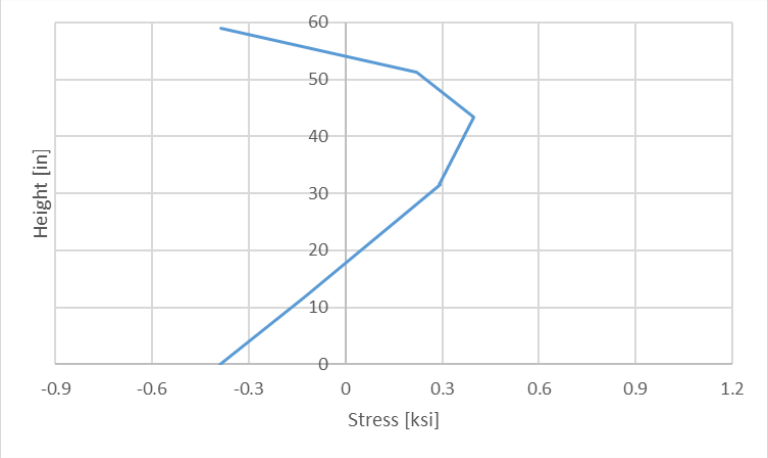

Figure A-7-The primary stresses caused by the piecewise linear approximation (compression is negative)

Secondary stress formed in an indeterminate structure in the center span (peak bending moment) through the depth of the cross section is shown in Figure A-8:

$$f_{s_{(y)}} = \frac{M'(n-y)}{I}$$

$$f_{s_{(y)}} = \frac{6{,}520.9\ kNm(1.052-y)}{0.2319m^4 * 4}$$

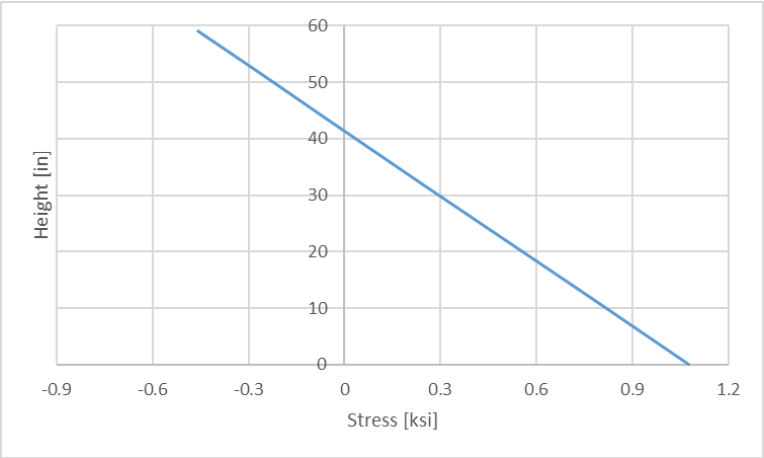

Figure A-8-Secondary stress caused by peak bending moment (compression is negative)

Total stress (in center span at location of peak bending moment) through the depth of the cross section is shown in Figure A-9:

$$f_{t_{(y)}} = f_{p_{(y)}} + f_{s_{(y)}}$$

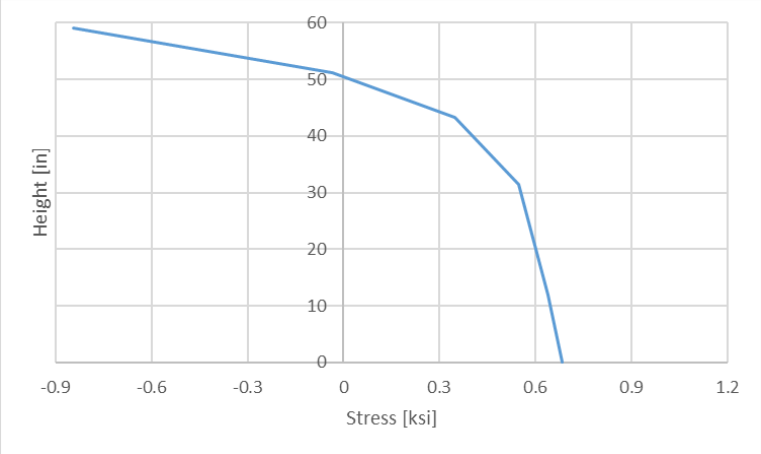

Figure A-9-Total stress caused by peak bending moment (compression is negative)

Stresses in the top and bottom fiber of the bridge along the length of the bridge:

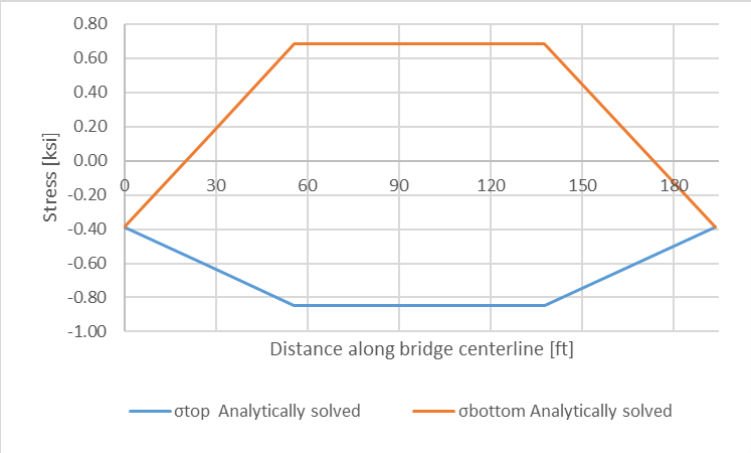

Figure A-10-Total stress in top and bottom fiber of cross section

APPENDIX B - COMPOSITE BRIDGE SECTION THERMAL LOADING STRAIN AND CURVATURE EQUATIONS

Formulating the equations to express the curvature and strain caused in a composite bridge was accomplished by following the same processing axial force and internal moment used by Priestley and Buckle (1978) for a concrete bridge section. However, to allow for the different material properties of the composite section the solutions used a modulus of elasticity and coefficient of thermal expansion that vary through depth, E(y) and α(y) respectively. Since the change in material properties takes place at the point of interface, di, between steel and concrete (Figure B-1) the equations were solved by discretely separating the integrations into concrete and steel sections. For these equations to be valid the follow assumptions must be made: I_t is the moment of inertia of the transformed section and is taken at the transformed section centroid, A_t is area of the transformed section, the curvature of steel and concrete sections must be equal and n is the distance from the transformed section centroid to an arbitrary datum.

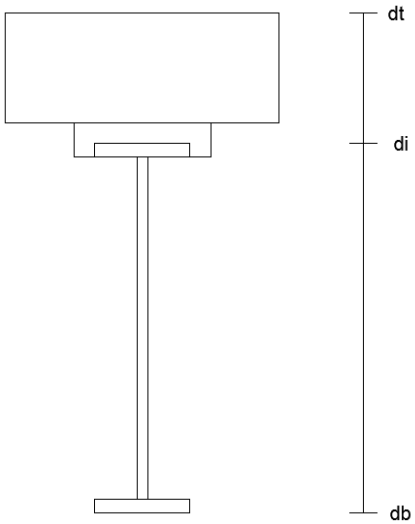

Figure B-1-Composite bridge cross section

Solving for the internal moment:

$$M = \int_{db}^{dt} \left(\varepsilon_{(y)} - \alpha_{(y)} t_{(y)}\right) E_{(y)} b_{(y)} (y - n) dy$$

Substituting $\varepsilon_{(y)} = \varepsilon_0 + \psi y$:

$$M = \int_{db}^{dt} \left((\varepsilon_0 + \psi y) - \alpha_{(y)} t_{(y)}\right) E_{(y)} b_{(y)} (y - n) dy$$

$$M = \int_{db}^{dt} \left((\varepsilon_0 + \psi y) E_{(y)} b_{(y)} (y - n) - \alpha_{(y)} t_{(y)} E_{(y)} b_{(y)} (y - n)\right) dy$$

$$M = \int_{db}^{dt} \left(\varepsilon_0 E_{(y)} b_{(y)}(y-n) + \psi y E_{(y)} b_{(y)}(y-n) - \alpha_{(y)} t_{(y)} E_{(y)} b_{(y)}(y-n)\right) dy$$

$$M = \varepsilon_0 \int_{db}^{dt} E_{(y)} b_{(y)}(y-n)\, dy + \psi \int_{db}^{dt} y E_{(y)} b_{(y)}(y-n) dy - \int_{db}^{dt} \alpha_{(y)} t_{(y)} E_{(y)} b_{(y)}(y-n) dy$$

Solving this equation for a simply supported beam, no moment restraint (M=0) and using transformed section method to replace the stiffness of steel with equivalent concrete such that $m = \frac{E_s}{E_c}$ and $b'_{(y)} = \begin{cases} m b_{(y)}, y < di \\ b_{(y)}, y \geq di \end{cases}$:

$0 = \varepsilon_0 \int_{db}^{dt} E_c b'_{(y)}(y-n)\, dy + \psi \int_{db}^{dt} y E_c b'_{(y)}(y-n) dy - \alpha_c \int_{di}^{dt} t_{(y)} E_c b'_{(y)}(y-n) dy - \alpha_s \int_{db}^{di} t_{(y)} E_c b'_{(y)}(y-n) dy$

Substituting $\int b_{(y)}\ dy = A$, $\int y b_{(y)}\ dy = nA$, and $\int y^2 b_{(y)}\ dy = I + n^2 A$:

$0 = \varepsilon_0 E_c (0) + \psi E_c I_t - \alpha_c E_c \int_{di}^{dt} t_{(y)} b'_{(y)}(y-n) dy - \alpha_s E_c \int_{db}^{di} t_{(y)} b'_{(y)}(y-n) dy$

$$0 = \psi E_c I_t - \alpha_c E_c \int_{di}^{dt} t_{(y)} b'_{(y)}(y-n) dy - \alpha_s E_c \int_{db}^{di} t_{(y)} b'_{(y)}(y-n) dy$$

Solving for the curvature (ψ):

$$\psi I_t = \alpha_c \int_{di}^{dt} t_{(y)} b'_{(y)}(y-n) dy + \alpha_s \int_{db}^{di} t_{(y)} b'_{(y)}(y-n) dy$$

$$\psi = \frac{\alpha_c \int_{di}^{dt} t_{(y)} b'_{(y)}(y-n) dy + \alpha_s \int_{db}^{di} t_{(y)} b'_{(y)}(y-n) dy}{I_t}$$

Solving for the axial force:

$$P = \int_{db}^{dt} \left(\varepsilon_{(y)} - \alpha_{(y)} t_{(y)}\right) E_{(y)} b_{(y)} dy$$

Substituting $\varepsilon_{(y)} = \varepsilon_0 + \psi y$:

$$P = \int_{db}^{dt} \left((\varepsilon_0 + \psi y) - \alpha_{(y)} t_{(y)}\right) E_{(y)} b_{(y)} dy$$

$$P = \int_{db}^{dt} \left((\varepsilon_0 + \psi y) E_{(y)} b_{(y)} - \alpha_{(y)} t_{(y)} E_{(y)} b_{(y)}\right) dy$$

$$P = \int_{db}^{dt} \left(\varepsilon_0 E_{(y)} b_{(y)} + \psi y E_{(y)} b_{(y)} - \alpha_{(y)} t_{(y)} E_{(y)} b_{(y)}\right) dy$$

$$P = \varepsilon_0 \int_{db}^{dt} E_{(y)} b_{(y)}\, dy + \psi \int_{db}^{dt} y E_{(y)} b_{(y)} dy - \int_{db}^{dt} \alpha_{(y)} t_{(y)} E_{(y)} b_{(y)} dy$$

Solving this equation for a simply supported beam, no axial restraint (P=0) and using transformed section method to replace the stiffness of steel with equivalent concrete such that $m = \frac{E_s}{E_c}$ and $b'_{(y)} = \begin{cases} m b_{(y)}, y < di \\ b_{(y)}, y \geq di \end{cases}$:

$$0 = \varepsilon_0 \int_{db}^{dt} E_c b'_{(y)}\, dy + \psi \int_{db}^{dt} y E_c b'_{(y)} dy - \alpha_c \int_{di}^{dt} t_{(y)} E_c b'_{(y)} dy - \alpha_s \int_{db}^{di} t_{(y)} E_c b'_{(y)} dy$$

Substituting $\int b_{(y)}\ dy = A$, $\int y b_{(y)}\ dy = nA$, and $\int y^2 b_{(y)}\ dy = I + n^2 A$:

$$0 = \varepsilon_0 E_c A_t + \psi E_c n A_t - \alpha_c \int_{di}^{dt} t_{(y)} E_c b'_{(y)} dy - \alpha_s \int_{db}^{di} t_{(y)} E_c b'_{(y)} dy$$

Solving for strain (ε_0):

$$\varepsilon_0 A_t = \alpha_c \int_{di}^{dt} t_{(y)} b'_{(y)} dy + \alpha_s \int_{db}^{di} t_{(y)} b'_{(y)} dy - \psi n A_t$$

$$\varepsilon_0 = \frac{\alpha_c \int_{di}^{dt} t_{(y)} b'_{(y)} dy + \alpha_s \int_{db}^{di} t_{(y)} b'_{(y)} dy}{A_t} - \psi n$$

APPENDIX C - COMPOSITE BRIDGE SECTION VERIFICATION EXAMPLE

This example used the equations of Appendix B to solve for the reactions of a composite bridge, for comparison to the CSiBridge composite model. The moment and reactions solved by using the previous equations were compared to those found using CSiBridge. A simple composite bridge cross section was selected (Figure C-1). The dimension of a single girder and effective deck width (a quarter of the total deck) and the AASHTO LRFD thermal gradient for composite bridges in Zone 1 are shown in Figure C-2. The dimensions of the I-beam are shown in Figure C-3. The span dimensions of the bridge are shown in Figure C-4.

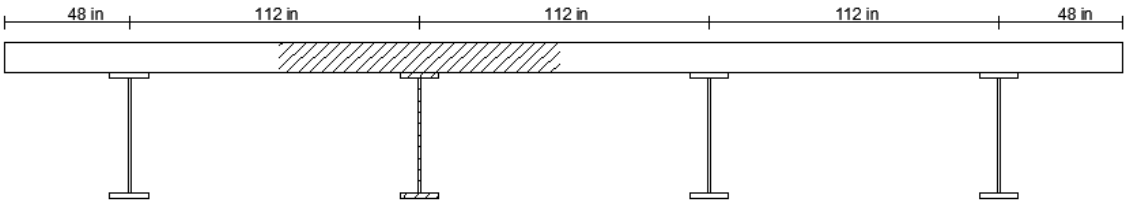

Figure C-1-Bridge cross section

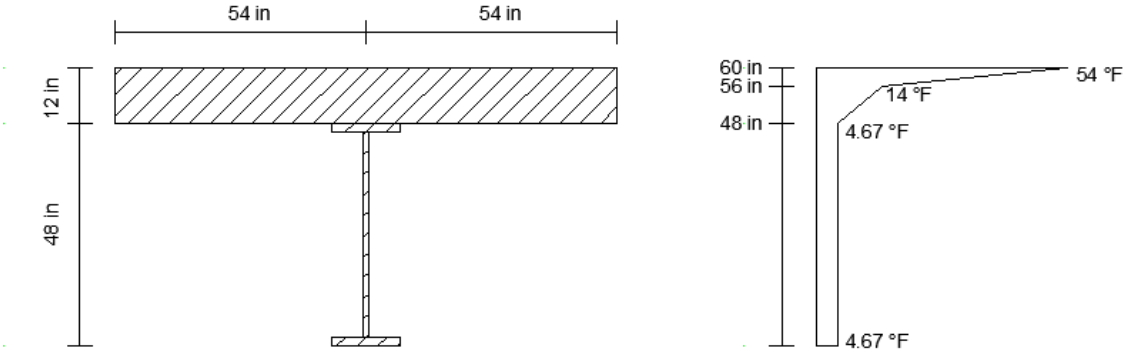

Figure C-2-Single-girder cross section and applied thermal gradient

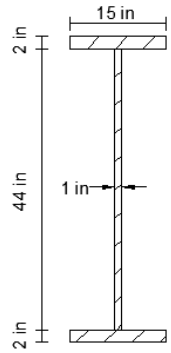

Figure C-3-I beam dimensions

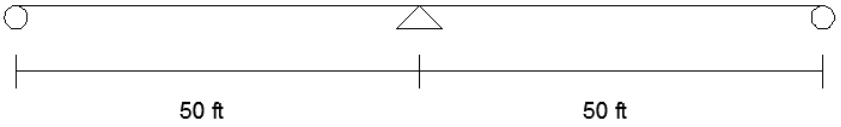

Figure C-4-Bridge span dimensions

The material properties of the concrete and steel used in analysis of the single girder section:

$$\alpha_c = 5.5 * 10^{-6\circ} F^{-1}$$

$$\alpha_s = 6.5 * 10^{-6\circ} F^{-1}$$

$$E_c = 3605\ ksi$$

$$E_s = 29000\ ksi$$

The cross-section properties of the single girder:

$$I_t = 7.85 * 10^5\ in^4$$

$$n = 42.24\ in$$

Setting the bottom of the bridge as the datum (y equal to zero), the following equations express the temperature through the depth of the bridge:

$$t_{(y)} = 4.67°F \text{ For } 0 \leq y \leq 48\ in$$

$$t_{(y)} = 1.1662y - 51.31°F \text{ For } 48 \leq y \leq 56\ in$$

$$t_{(y)} = 10y - 546°F \text{ For } 56\ \leq y \leq 60\ in$$

Solving for the curvature of the bridge without the pier supports (simply supported):

$$\psi = \frac{\alpha_c \int_{di}^{dt} t_{(y)} b_{(y)} (y-n)dy + m\,\alpha_s \int_{db}^{di} t_{(y)} b_{(y)} (y-n)dy}{(I_t)}$$

$$\psi = \frac{m\alpha_s}{(I_t)}\left[\int_0^2 (4.67)(15)\,(y-42.24)dy + \int_2^{46} (4.67)(1)\,(y-42.24)dy + \int_{46}^{48} (4.67)(15)\,(y-42.24)dy\right] + \frac{\alpha_c}{(I_t)}\left[\int_{48}^{56} (1.1662y-51.31)(108)\,(y-42.24)dy + \int_{56}^{60} (10y-546)(108)\,(y-42.24)dy\right]$$

$$\psi = \frac{8.04 * 6.5 * 10^{-6}}{7.85 * 10^5}[-5777.72 - 3747.94 + 666.88] + \frac{5.5 * 10^{-6}}{7.85 * 10^5}[84070.60 + 237243]$$

$$\psi = 1.66 * 10^{-6}\ in^{-1}$$

The curvature of the bridge caused by thermal gradients is resisted in an indeterminate structure. To remove the incompatible rotation at each support, a restraint moment is applied as shown in Figure C-5.

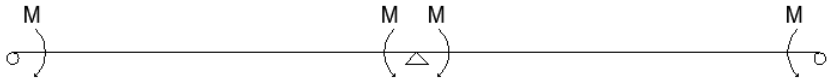

Figure C-5-Moment restraints

The restraint moment (the moment of inertia of the entire cross section of bridge required):

$$M = E_c(I_t)\,\psi$$

$$M = 3605\ ksi * (7.85 * 10^5\ in^4 * 4) * 1.479 * 10^{-6}\ in^{-1}$$

$$M = 18{,}804.2\ kip - in$$

The actual bending moment in the beam can be found using moment distribution method, for this case the adjusted moment is $M' = 1.5M$:

$$M' = 1.5M = 28{,}206.3\ kip - in$$

Reaction forces:

$$V = \frac{M'}{50ft} = 47.01$$

The resulting bending moment and reaction forces are shown in Figure C-6 and C-7:

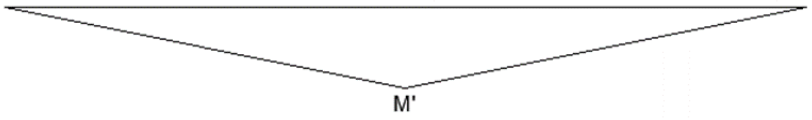

Figure C-6-Bending moment diagram

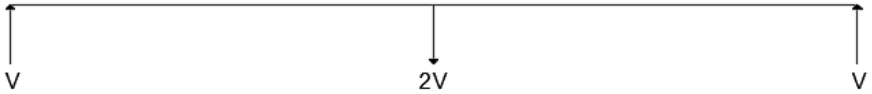

Figure C-7- Support reaction diagram

APPENDIX D- ANALYTICAL SOLUTION TO SIMPLIFIED MODEL OF AIRPORT CONNECTOR UNDER THERMAL LOADING

The AASHTO Zone 1 thermal gradient was applied to the Airport Connector Bridge to calculate the support reactions and stresses which were compared to the results from CSiBridge models in Chapter 5. The overall bridge cross section of the Airport Connector bridge can be found in Figure 5-2. The dimension of a single girder, effective deck width (a quarter of the total deck) effective soffit width (a quarter of the total soffit) and the thermal gradient applied are shown in Figure D-1. The span dimensions of the bridge are shown in Figure D-2.

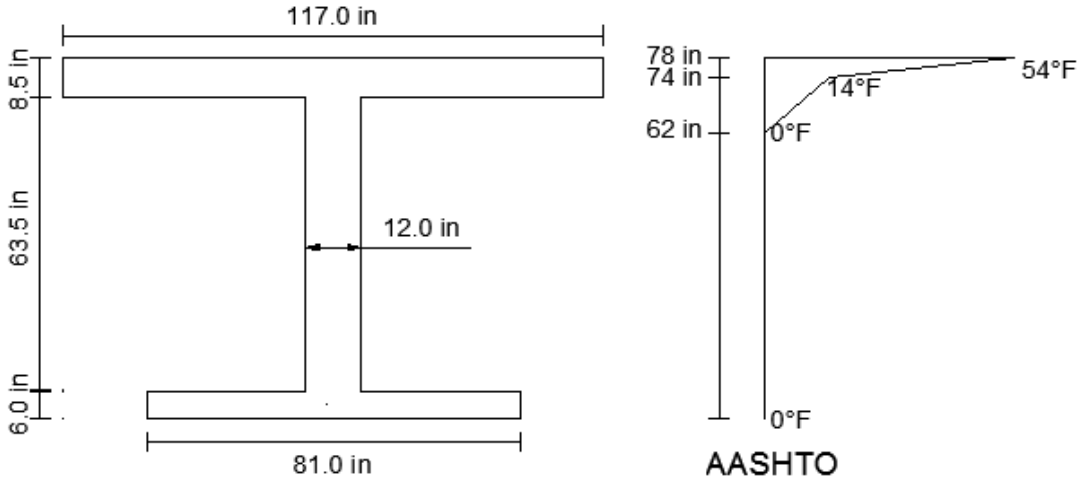

Figure D-1-Single-girder cross section and applied thermal gradient

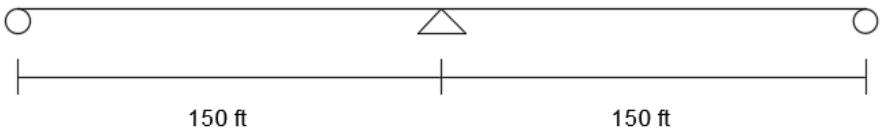

Figure D-2-Bridge span dimensions

The material properties of the concrete used in analysis of the single girder section:

$$\alpha = 5.5 * 10^{-6\circ} F^{-1}$$

$$E = 4030\ ksi$$

The cross-section properties of the single girder:

$$I = 1.9797 * 10^{6} in^{4}$$

$$A = 2242.5in^2$$

$$n = 46.18\ in$$

Setting the bottom of the bridge as the datum (y equal to zero), the following equations express the temperature through the depth of the bridge:

$$t_{(y)} = 0°F \text{ For } 0 \leq y \leq 62in$$

$$t_{(y)} = 1.1667y - 72.33\ °F \text{ For } 62 \leq y \leq 74in$$

$$t_{(y)} = 10y - 726°F \text{ For } 74 \leq y \leq 78\ in$$

Solving for the curvature of the bridge without the pier supports (simply supported):

$$\psi = \frac{\alpha}{I}\int t_{(y)} b_{(y)} (y - n)dy$$

$$\psi = \frac{\alpha}{I}[\int_0^6 (0)(81)\,(y - 46.18)dy + \int_6^{62} (0)(12)\,(y - 46.18)dy + \int_{62}^{69.5} (1.1667y - 72.33)(12)\,(y - 46.18)dy + \int_{69.5}^{74} (1.1667y - 72.33)(117)\,(y - 46.18)dy + \int_{74}^{78} (10y - 726)(117)\,(y - 46.18)dy]$$

$$\psi = \frac{5.5 * 10^{-6}}{1.9797 * 10^6}[0 + 0 + 8{,}207.62 + 154{,}251 + 480{,}736]$$

$$\psi = 1.787 * 10^{-6} in^{-1}$$

The curvature of the bridge caused by thermal gradients is resisted in an indeterminate structure. To remove the incompatible rotation at each support, a restraint moment is applied as shown in Figure D-3.

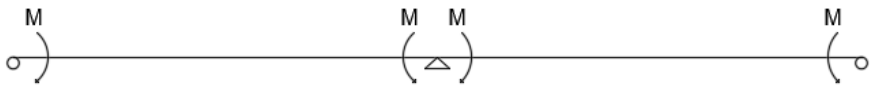

Figure D-3-Moment restraints

The restraint moment (the moment of inertia of the entire cross section of bridge required):

$$M = EI\ \psi$$

$$M = 4030\ ksi * (1.9797 * 10^6 in^4 * 4) * 1.787 * 10^{-6} in^{-1}$$

$$M = 57026\ kip - in$$

The actual bending moment in the beam can be found using moment distribution method, for this case the adjusted moment is $M' = 1.5M$:

$$M' = 1.5M = 85538\ kip - in$$

$$M' = 7128\ kip - ft$$

Reaction forces:

$$V = \frac{dM}{dx} = \frac{M'}{150\ ft} = 47.52\ kip$$

The resulting bending moment and reaction forces are shown in Figure D-4 and D-5.

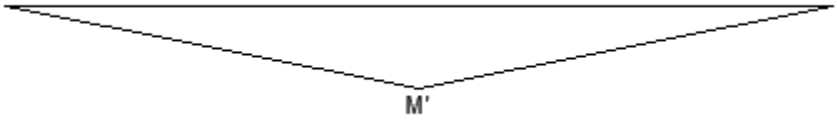

Figure D-4-Bending moment diagram

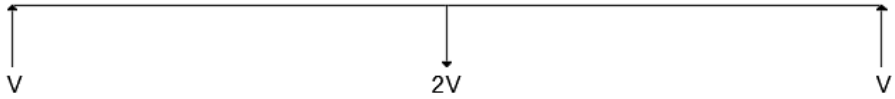

Figure D-5- Support reaction diagram

Solving for the strain in the bridge without the pier supports (simply supported):

$$\varepsilon_0 = \frac{\alpha}{A}\int t_{(y)} b_{(y)} dy - \psi n$$

$$\varepsilon_0 = \frac{\alpha}{A}\left[\int_0^6 (0)(81)\,dy + \int_6^{62} (0)(12)\,dy + \int_{62}^{69.5} (1.1667y - 72.33)(12)\,dy + \int_{69.5}^{74} (1.1667y - 72.33)(117)\,dy + \int_{74}^{78} (10y - 726)(117)\,dy\right] - 1.787 * 10^{-6} in^{-1} * 46.18\ in$$

$$\varepsilon_0 = \frac{5.5 * 10^{-6}}{2242.5 in^2}[0 + 0 + 394.247 + 5991.95 + 15912] - 1.787 * 10^{-6} in^{-1} * 46.18\ in$$

$$\varepsilon_0 = -2.78 * 10^{-5}$$

Primary thermal stress through depth of the cross section (shown in Figure D-6):

$$f_{p_{(y)}} = E(\varepsilon_0 + \psi y - \alpha \cdot t_{(y)})$$

From $0 \leq y \leq 62in$:

$$f_{p_{(y)}} = 4030\ ksi(-2.78 * 10^{-5} + 1.787 * 10^{-6} \cdot y - 5.5 * 10^{-6} \cdot 0\ )$$

From $62 \leq y \leq 74in$:

$$f_{p_{(y)}} = 4030\ ksi\big(-2.78 * 10^{-5} + 1.787 * 10^{-6} \cdot y - 5.5 * 10^{-6} \cdot (1.1667y - 72.33\ )\big)$$

From $74 \leq y \leq 78\ in$:

$$f_{p_{(y)}} = 4030\ ksi(-2.78 * 10^{-5} + 1.787 * 10^{-6} \cdot y - 5.5 * 10^{-6} \cdot (10y - 726))$$

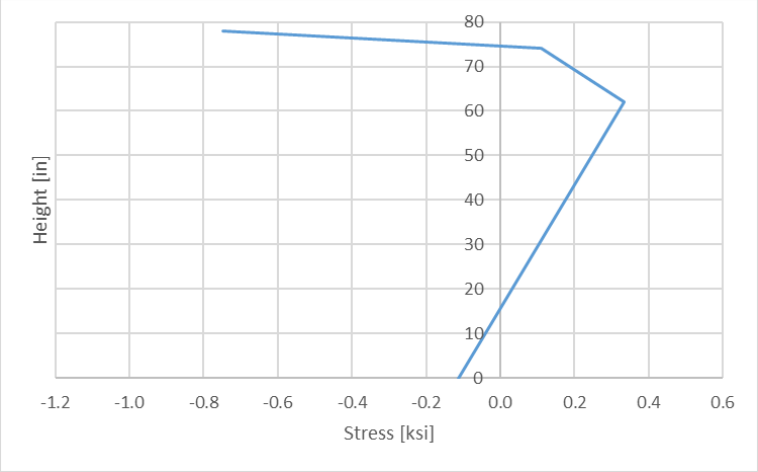

Figure D-6-The primary stresses caused by the AASHTO Zone 1 thermal gradient (compression is negative)

Secondary stresses formed in an indeterminate structure at pier support (point of peak bending moment) through the depth of the cross section is shown in Figure D-7:

$$f_{s_{(y)}} = \frac{M'(n - y)}{I}$$

$$f_{s_{(y)}} = \frac{87443kip - in(46.18 - y)}{1.9797 * 10^6 in^4 * 4}$$

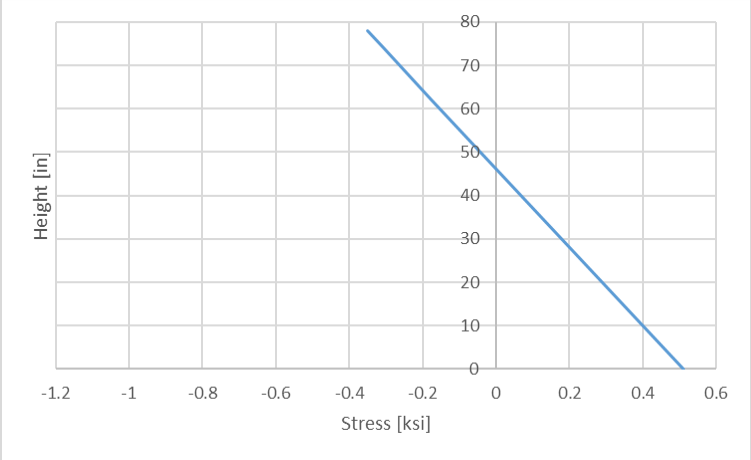

Figure D-7-Secondary stress caused by maximum bending moment (compression is negative)

Total stress at pier support (at pier support, location of maximum bending moment) through the depth of the cross section is shown in Figure D-8:

$$f_{t_{(y)}} = f_{p_{(y)}} + f_{s_{(y)}}$$

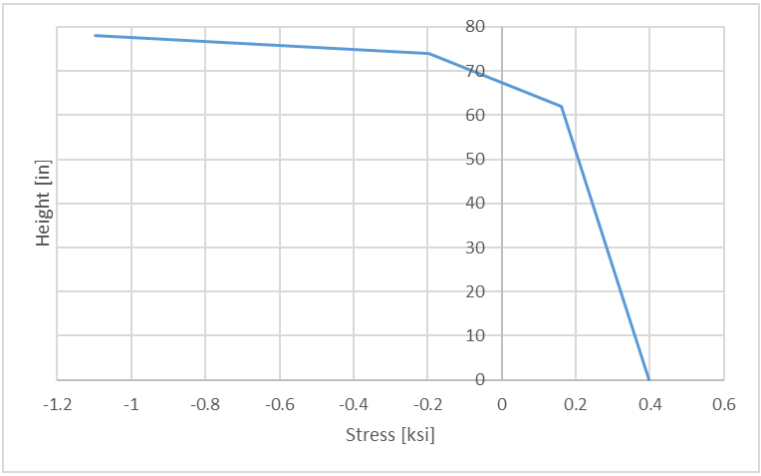

Figure D-8-Total stress caused by maximum bending moment (compression is negative)

APPENDIX E - ANALYTICAL SOLUTION TO SIMPLIFIED MODEL OF I-580 UNDER THERMAL LOADING

The AASHTO Zone 1 thermal gradient was applied to the Airport Connector Bridge to calculate the support reactions which were compared to the results from CSiBridge models in Chapter 6. The cross section of the I-580 bridge can be found in Chapter 6 (Figure 6-2). The dimension of a single girder, effective deck width (a tenth of the total deck) and the thermal gradient applied are shown in Figure E-1. The dimensions of the I-beam are shown in Figure E-2. The span dimensions of the bridge are shown in Figure E-3.

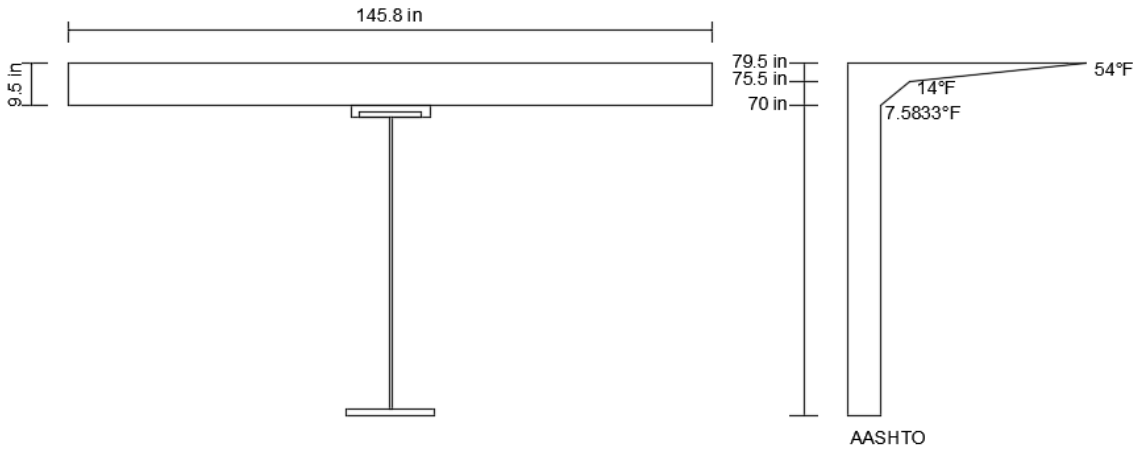

Figure E-1-Single-girder cross section and applied thermal gradient

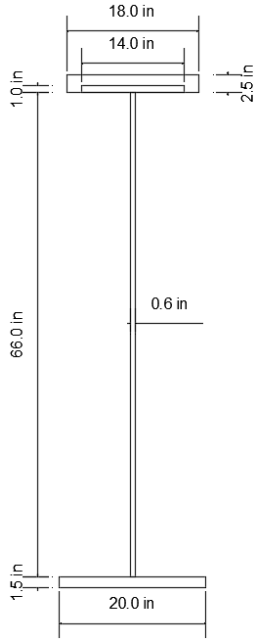

Figure E-2-I beam dimensions

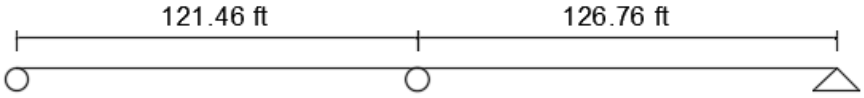

Figure E-3-Bridge span dimensions

The material properties of the concrete and steel used in analysis of the single girder section:

$$\alpha_c = 5.5 * 10^{-6\circ} F^{-1}$$

$$\alpha_s = 6.5 * 10^{-6\circ} F^{-1}$$

$$E_c = 3823.67\ ksi$$

$$E_s = 29000\ ksi$$

The cross-section properties of the single girder:

$$I_t = 1.0742 * 10^6 in^4$$

$$n = 62.13\ in$$

Setting the bottom of the bridge as the datum (y equal to zero), the following equations express the temperature through the depth of the bridge:

$$t_{(y)} = 7.5833°F \text{ For } 0 \leq y \leq 70in$$

$$t_{(y)} = 1.1667y - 74.084\ °F \text{ For } 70 \leq y \leq 75.5in$$

$$t_{(y)} = 10y - 741°F \text{ For } 75.5 \leq y \leq 79.5\ in$$

Solving for the curvature of the bridge without the pier supports (simply supported):

$$\psi = \frac{\alpha}{I}\int t_{(y)} b_{(y)}(y-n)dy$$

$$\psi = \frac{m\alpha_s}{(I_t)}\left[\int_0^{1.5}(7.5833)(20)\,(y-62.13)dy + \int_{1.5}^{67.5}(7.5833)(0.625)\,(y-62.13)dy + \int_{67.5}^{68.5}(7.5833)(14)\,(y-62.13)dy\right] + \frac{\alpha_c}{(I_t)}\left[\int_{68.5}^{70}(7.5833)(18)\,(y-62.13)dy + \int_{70}^{75.5}(1.1662y-74.084)(145.8)\,(y-62.13)dy + \int_{75.5}^{79.5}(10y-741)(145.8)\,(y-62.13)dy\right]$$

$$\psi = \frac{7.58 * 6.5 * 10^{-6}}{1.0742 * 10^{6}}[-13963.9 - 8642.97 + 623.196] + \frac{5.5 * 10^{-6}}{1.0742 * 10^{6}}[1457.81 + 93966.4 + 312545]$$

$$\psi = 1.08 * 10^{-6} in^{-1}$$

The curvature of the bridge caused by thermal gradients is resisted in an indeterminate structure. To remove the incompatible rotation at each support, a restraint moment is applied as shown in Figure E-4.

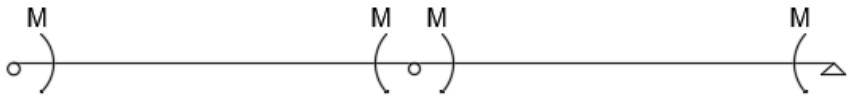

Figure E-4-Moment restraints

The restraint moment (the moment of inertia of the entire cross section of bridge required):

$$M = EI_t\,\psi$$

$$M = 3824\ ksi * (1.0742 * 10^{6} in^4 * 10) * 1.08 * 10^{-6} in^{-1}$$

$$M = 44357.45\ kip - in$$

The actual bending moment in the beam can be found using moment distribution method, for this case the adjusted moment is estimated to be $M' = 1.5M$:

$$M' = 1.5M = 66536\ kip - in$$

$$M' = 5545\ kip - ft$$

Reaction forces:

$$V_1 = \frac{dM}{dx} = \frac{M'}{121.465\ ft} = 45.64\ kip$$

$$V_2 = \frac{dM}{dx} = \frac{M'}{126.744\ ft} = 43.74\ kip$$

The resulting bending moment and reaction forces are shown in Figure E-5 and E-6.

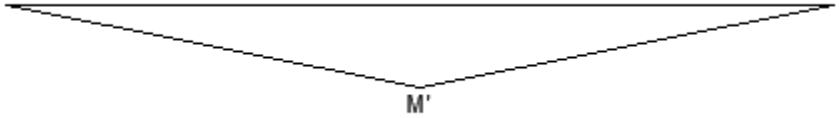

Figure E-5-Bending moment diagram

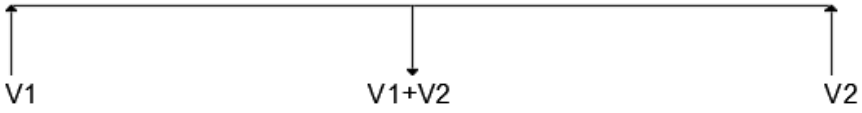

Figure E-6- Support reaction diagram

Nevada Department of Transportation
Rudy Malfabon, P.E. Director
Ken Chambers, Research Division Chief
(775) 888-7220
kchambers@dot.nv.gov
1263 South Stewart Street
Carson City, Nevada 89712